

Library Declaration and Deposit Agreement

1. STUDENT DETAILS

Toby Rodel
1913707

2. THESIS DEPOSIT

- 2.1 I understand that under my registration at the University, I am required to deposit my thesis with the University in BOTH hard copy and in digital format. The digital version should normally be saved as a single pdf file.
- 2.2 The hard copy will be housed in the University Library. The digital version will be deposited in the University's Institutional Repository (WRAP). Unless otherwise indicated (see 2.3 below) this will be made openly accessible on the Internet and will be supplied to the British Library to be made available online via its Electronic Theses Online Service (EThOS) service. [At present, theses submitted for a Master's degree by Research (MA, MSc, LLM, MS or MMedSci) are not being deposited in WRAP and not being made available via EThOS. This may change in future.]
- 2.3 In exceptional circumstances, the Chair of the Board of Graduate Studies may grant permission for an embargo to be placed on public access to the hard copy thesis for a limited period. It is also possible to apply separately for an embargo on the digital version. (Further information is available in the Guide to Examinations for Higher Degrees by Research.)
- 2.4 (a) Hard Copy I hereby deposit a hard copy of my thesis in the University Library to be made publicly available to readers immediately.
I agree that my thesis may be photocopied.
- (b) Digital Copy I hereby deposit a digital copy of my thesis to be held in WRAP and made available via EThOS.
My thesis can be made publicly available online.

3. GRANTING OF NON-EXCLUSIVE RIGHTS

Whether I deposit my Work personally or through an assistant or other agent, I agree to the following: Rights granted to the University of Warwick and the British Library and the user of the thesis through this agreement are non-exclusive. I retain all rights in the thesis in its present version or future versions. I agree that the institutional repository administrators and the British Library or their agents may, without changing content, digitise and migrate the thesis to any medium or format for the purpose of future preservation and accessibility.

4. DECLARATIONS

(a) I DECLARE THAT:

- I am the author and owner of the copyright in the thesis and/or I have the authority of the authors and owners of the copyright in the thesis to make this agreement. Reproduction of any part of this thesis for teaching or in academic or other forms of publication is subject to the normal limitations on the use of copyrighted materials and to the proper and full acknowledgement of its source.
- The digital version of the thesis I am supplying is the same version as the final, hardbound copy submitted in completion of my degree, once any minor corrections have been completed.
- I have exercised reasonable care to ensure that the thesis is original, and does not to the best of my knowledge break any UK law or other Intellectual Property Right, or contain any confidential material.
- I understand that, through the medium of the Internet, files will be available to automated agents, and may be searched and copied by, for example, text mining and plagiarism detection software.

(b) IF I HAVE AGREED (in Section 2 above) TO MAKE MY THESIS PUBLICLY AVAILABLE DIGITALLY, I ALSO DECLARE THAT:

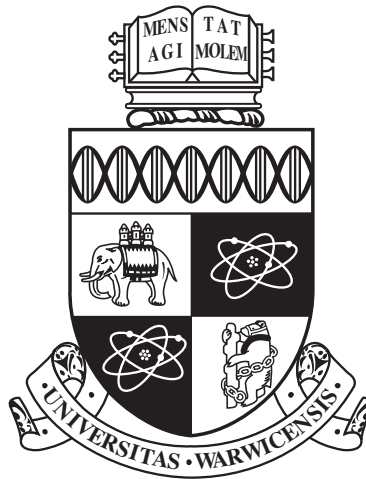
- I grant the University of Warwick and the British Library a licence to make available on the Internet the thesis in digitised format through the Institutional Repository and through the British Library via the EThOS service.
- If my thesis does include any substantial subsidiary material owned by third-party copyright holders, I have sought and obtained permission to include it in any version of my thesis available in digital format and that this permission encompasses the rights that I have granted to the University of Warwick and to the British Library.

5. LEGAL INFRINGEMENTS

I understand that neither the University of Warwick nor the British Library have any obligation to take legal action on behalf of myself, or other rights holders, in the event of infringement of intellectual property rights, breach of contract or of any other right, in the thesis.

Please sign this agreement and return it to the Graduate School Office when you submit your thesis.

Student's signature:  Date: 20/11/2023



**Estimating the yield of long-period exoplanets from
the Transiting Exoplanet Survey Satellite**

by

Toby Rodel

Thesis

Submitted to the University of Warwick

for the degree of

Master of Science (by Research) in Physics

Department of Physics

September 2023

THE UNIVERSITY OF
WARWICK

Contents

List of Tables	iv
List of Figures	v
Acknowledgments	vii
Declarations	ix
Data Acknowledgements	x
Abstract	xi
Abbreviations	xii
Chapter 1 Introduction	1
1.1 Exoplanets: An overview	1
1.2 Discovery methods	2
1.2.1 Direct Imaging	3
1.2.2 Microlensing	4
1.2.3 Astrometry	7
1.2.4 Radial Velocity method	8
1.2.5 Transit method	12
1.3 Exoplanet demographics	13
1.3.1 Super-Earths and Mini-Neptunes	13
1.3.2 Hot Jupiters	16
1.3.3 Warm Jupiters	17
1.4 Transits 101	18
1.4.1 Transit Geometry	18
1.4.2 Transit observations	23
1.4.3 Additional science from transits	23

1.5	Transit surveys	26
1.5.1	Ground-based surveys	26
1.5.2	The <i>Kepler</i> space telescope	29
1.6	The Transiting Exoplanet Survey Satellite (<i>TESS</i>)	30
1.6.1	Overview	30
1.6.2	Pointings	32
1.6.3	Discoveries	34
1.7	Monotransits	34
1.8	Project Objectives	35

Chapter 2 Estimating yields of long-period planets from the southern ecliptic of *TESS* 38

2.1	Introduction	39
2.2	The TIaRA pipeline	43
2.2.1	Input of Lightcurves	43
2.2.2	Simulating Transiting Planets	45
2.2.3	Signal-to-Noise Calculation	47
2.2.4	Detection Probability	48
2.2.5	Minimum detectable radius cutoff	50
2.3	<i>TESS</i> simulations	50
2.3.1	<i>TESS</i> SPOC FFI lightcurves	50
2.3.2	Stellar parameters	51
2.3.3	Window functions	51
2.3.4	Signal to Noise	52
2.3.5	Probability of detection	52
2.3.6	Creating sensitivity maps	54
2.3.7	Occurrence Rates	54
2.3.8	Yield Estimates	55
2.4	Results	57
2.4.1	<i>TESS</i> Sensitivity	57
2.4.2	Predicted Yield	60
2.4.3	Monotransits	60
2.4.4	Duotransits	63
2.4.5	Breakdown by Spectral Type	63
2.4.6	Comparison of Detection Probability Functions	65
2.5	Discussion	68
2.5.1	Comparison to actual <i>TESS</i> detections	68

2.5.2	Comparison to Biennial Duotransit search	70
2.5.3	Comparison to previously predicted yield	70
2.5.4	Occurrence Rates	71
2.5.5	Probability of detection	72
2.5.6	Use of Year 1 and Year 3 SPOC FFI Lightcurves	73
2.6	Summary and Conclusion	73
2.7	Appendix	74
2.7.1	Sensitivity by spectral types	74
2.7.2	Yield by spectral type	74
Chapter 3	Future work and Conclusion	85
3.1	Summary of Key Results	85
3.2	Future Work on <i>TESS</i>	86
3.2.1	Northern ecliptic Hemisphere: Year 2 and Year 4	86
3.2.2	Update to southern ecliptic with Year 5	87
3.2.3	Quick Look Pipeline (QLP) lightcurves	87
3.2.4	Future <i>TESS</i> sectors	88
3.2.5	Occurrence rates	88
3.3	Applications to other Transit Surveys	88
3.3.1	<i>PLATO</i>	89
3.4	TTaRA Upgrades	90
3.5	Conclusions	91

List of Tables

2.1	Gamma function coefficients	49
-----	---------------------------------------	----

List of Figures

1.1	Cumulative exoplanet discoveries by discovery method per year . . .	3
1.2	Directly imaged exoplanet	5
1.3	Planetary microlensing event	6
1.4	Example astrometry observation	9
1.5	RV phase curve of 51 Peg	10
1.6	RV phase curve of HD 80606	11
1.7	Exoplanet mass-period diagram	14
1.8	Exoplanet radius-period diagram	15
1.9	Overview of a transiting exoplanetary system	19
1.10	Geometry of transit	20
1.11	Transiting exoplanet shadow	22
1.12	Unfolded <i>TESS</i> lightcurve of <i>WASP</i> -18	24
1.13	<i>TESS</i> phase curve of <i>WASP</i> -18	25
1.14	<i>WASP</i>	27
1.15	<i>NGTS</i>	28
1.16	<i>TESS</i> payload and spacecraft	30
1.17	Layout of <i>TESS</i> sectors	31
1.18	<i>TESS</i> sectors for years 1, 2 and 3	33
1.19	Monotransit lightcurve	36
2.1	The <i>TESS</i> planet sample	41
2.2	TTaRA pipeline flowchart	44
2.3	Gamma function plot	49
2.4	<i>TESS</i> CVZ lightcurve	52
2.5	Comparison of <i>TESS</i> window functions	53
2.6	Rebinned M dwarf planetary occurrence rates	56
2.7	Overall <i>TESS</i> sensitivity map	57
2.8	<i>TESS</i> yield	58

2.9	Total yield histograms	59
2.10	Monotransit yield histograms	61
2.11	Monotransit period evolution	62
2.12	Biennial duotransit yield histogram	64
2.13	Long period yields by spectral type	66
2.14	Yields for different detection criteria	67
2.15	Long-period deficit	69
2.16	A type sensitivity map	75
2.17	F type sensitivity map	76
2.18	G type sensitivity map	77
2.19	K type sensitivity map	78
2.20	M type sensitivity map	79
2.21	A dwarf yields	80
2.22	F dwarf yields	81
2.23	G dwarf yields	82
2.24	K dwarf yields	83
2.25	M dwarf yields	84

Acknowledgments

My first thanks go to my Supervisor Dr Daniel Bayliss. I could not be more grateful to you for taking me on as a Master's student. Your patience, wisdom and warmth have meant so much while completing this thesis and I hope to remain collaborators and friends for years to come.

Thanks also to Dr Samuel Gill for co-supervising me this year. Sam, your technical expertise made this project possible and your sense of humour made Wednesdays a highlight when you came into the office. I am convinced the *NGTS* consortium would fall like a house of cards without you and the fact you still found time to help me out amongst that speaks volumes.

To Faith, thank you for your friendship and presence. Over this year you have quickly earned a spot amongst my greatest friends. You never fail to make me laugh and snap me out of it when my brain starts catastrophising. Playing stupid Music with you, Sam and Emre has also been not only the most fun I have had this year but through all of University. Make sure Gustavo eats good for me while I'm gone and try to keep at least some of the plants alive.

To Dr Matteo Brogi, before you started supervising my BSc project my confidence in myself as a scientist was at its lowest. If you hadn't told me I had the skills for research and encouraged me to seek out this MSc I would not be an astronomer today. I guess that makes you fully responsible for my research output for the rest of my career - for better or worse. I still seriously consider getting a *WASP-18b* tattoo to commemorate the project that got me started.

I would also like to extend my appreciation to the entire Astronomy and Astrophysics group at Warwick and to its late founder Professor Thomas Marsh.

My deepest gratefulness extends to Ioannis Apergis for giving me a room to stay in for the last three weeks of writing and to Marcelo, Morgan, James and Alastair for putting up with me freeloading in your house. Special mentions also go to Cait, Sean, Ares and Amena for their advice with navigating through my Masters year and to Dr Lauren Doyle for her supportiveness and providing opportunities for me to infodump about space to children. I will miss the cakes, the lunchtime conversations, Bec's laugh echoing down the hall to my office and wild Jorge sightings.

Thanking everyone individually who helped in some way with this thesis may take me past the heat death of the universe, let alone the submission deadline, so my final thanks are to all my friends, family and colleagues of whom I am surrounded with humbling numbers. I will miss everyone terribly in Belfast and would love as many of you as possible to visit.

My last thanks go to My Father, Mark Rodel who's passion for physics sometimes seems to outstrip my own. Even when his questions to me on quantum phenomena or General Relativity consistently prompt the response "I have *absolutely no idea*". Thank you for indulging my impassioned childhood rants on dinosaurs, showing an interest in my silly little science to this day.

Declarations

I declare that the work in this thesis is my own and was carried out at the University of Warwick, during the period October 2022 to October 2023, under the supervision of Dr. Daniel Bayliss and Dr Samuel Gill. The research reported here has not been submitted, either wholly or in part, in this or any other academic institution for admission to a higher degree.

The work in Chapter 2 of this is reproduced from a scientific paper written by myself, Dr Daniel Bayliss, Dr Samuel Gill and Faith Hawthorn which we plan to submit for publication in the Monthly Notices of the Royal Astronomical society (MNRAS). Co-author Gill provided general supervision and assistance with the programming elements of the project and wrote the code used to calculate the depth of grazing transits in Section 2.2.3. Co-Author Hawthorn supplied the data which we compare to our predictions in Figure 2.12b and Section 2.5.2.

Data Acknowledgements

We acknowledge the use of public TESS Alert data from pipelines at the TESS Science Office and at the TESS Science Processing Operations Centre. This paper includes data collected with the TESS mission, obtained from the MAST data archive at the Space Telescope Science Institute (STScI). Funding for the TESS mission is provided by the NASA Explorer Program. STScI is operated by the Association of Universities for Research in Astronomy, Inc., under NASA contract NAS 5–26555.

This research has made use of the NASA Exoplanet Archive, which is operated by the California Institute of Technology, under contract with the National Aeronautics and Space Administration under the Exoplanet Exploration Program.

Abstract

Since the first confirmed exoplanets were found in 1992 and 1995, exoplanetary science has grown rapidly into one of the largest and most exciting fields in Astronomy. The most successful technique to date for detecting exoplanets is the transit method, with thousands of exoplanets detected via transits. Despite this success, transit discoveries are dominated by planets with short orbital periods. The Transiting Exoplanet Survey Satellite (*TESS*), represents an opportunity to discover longer-period planets around nearby bright stars which can be studied in detail.

We present a study of the detection efficiency for the *TESS* mission, focusing on the yield of longer-period transiting exoplanets. We create the Transit Injection and Recovery Application (**TIaRA**) pipeline to use real *TESS* data with simulated transits to create sensitivity maps which we combine with known occurrence rates. This allows us to predict exoplanet yields from *TESS*. Our predicted yields are in good agreement with the actual discoveries from the *TESS* mission, however we find a significant lack of discovered long-period *TESS* planets compared to our predictions. This suggests the *TESS* discoveries to date are incomplete for longer-periods and more of these systems remain to be discovered in the *TESS* data.

The **TIaRA** pipeline we developed for this project is highly modular in nature and has the potential to be applied to further sets of *TESS* data and future transit surveys including the upcoming ESA *PLATO* mission.

Abbreviations

- **NASA** National Aeronautics and Space Administration
- ***TESS*** Transiting Exoplanet Survey Satellite
- **SPOC** Science Processing Operations Centre
- **QLP** Quick Look Pipeline
- **FFI** Full Frame Image
- **CVZ** Continuous Viewing Zone
- **TIC** *TESS* Input Catalogue
- **CTL** Candidate Target List
- **TOI** *TESS* Object Of Interest
- **TiARA** Transit Injection and Recovery Application
- **SNR** Signal-to-Noise Ratio
- ***NGTS*** Next Generation Transit Survey
- **CCD** Charged Coupled Device
- **CDPP** Combined Differential Photometric Precision.

Chapter 1

Introduction

"The search for knowledge is
hopeless and eternal; HOORAY!!!"

Professor Hubert J. Farnsworth
Futurama (1999-2003, 2008-2009,
2010-2013, 2023-)

1.1 Exoplanets: An overview

It seems that as long as human beings have existed we have been fascinated with the night sky. Aside from the awe inspired by the sight of a sky full of stars, it invites deeply philosophical questions about our place in the Universe. Are there other planets like Earth out there? Do any of them host life? Such questions have been pondered since at least 450 BC with Epicurus arguing that if the universe was infinite, as he thought, there must be infinite worlds both like and unlike our own. In the centuries that followed, our model of the universe moved from a geocentric one with the Earth at its centre to the heliocentric model proposed by Nicholas Copernicus in 1543 which placed the sun at the centre with the Earth and other planets revolving around it [Copernicus, 1543]. Italian philosopher and poet Giordano Bruno took Copernicus' idea even further and posited that most of the stars in the night sky were their own suns, hosting their own planetary systems like the solar system [Bruno, 1584a,b]. In 1600 Giordano Bruno was burned at the stake for heresy.

Other philosophers and scientists later supported the idea, including French scientist Bernard le Bovier de Fontenelle in *Entretiens sur la pluralité des mondes* (*Conversations on the Plurality of Worlds*) [Fontenelle, 1686], and the Dutch mathematician and astronomer Christiaan Huygens, who discussed the potential of

extrasolar planets hosting life and began to propose methods to detect them in *The celestial worlds discover'd* [Huygens, 1698].

In the centuries after Bruno and others first suggested their existence, numerous attempts were made to detect and confirm the existence of such extrasolar planets or "exoplanets", although it would take more than three centuries filled with erroneous attempts for the first confirmation and vindication of Bruno's ideas. In 1855, British astronomer William Stephen Jacob made the first serious claim of exoplanet detection when he suggested that orbital anomalies in the star 70 Ophiuci were due to the presence of an exoplanet [Jacob, 1855], although this was later proved to be invalid [Heintz, 1988]. Dutch astronomer Peter van de Kamp would make repeated claims of a planet around Barnard's star, first in 1963 then 1969 and again in 1982 now claiming two planets [van de Kamp, 1963, 1969, 1982]. Van de Kamp's results were contested by his contemporaries [Black & Suffolk, 1973] and later attributed to instrumental effects [Gatewood, 1995]. Modern observations have not found any confirmed planets around Barnard's star [Choi et al., 2013; Lubin et al., 2021]. In 1988 a tentative detection of a planet around the star Γ Cephei A was claimed [Campbell et al., 1988]. This claim was contested due to poor data quality and alternate explanations [Walker et al., 1992]. However, a planet would later be confirmed around the star in 2002 [Hatzes et al., 2003].

The exoplanet era as we know it would begin in earnest in 1992, when the first confirmed exoplanet was discovered around a pulsar - a rapidly rotating neutron star leftover from the death of a giant star [Wolszczan & Frail, 1992]. Shortly afterwards the first exoplanet was confirmed around a main sequence star similar to our own sun named 51 Pegasi b [Mayor & Queloz, 1995], a discovery that won the 2019 Nobel Prize in physics. Since these pioneering early discoveries the number of known exoplanets has grown exponentially as shown in Figure 1.1, with 5514 confirmed exoplanets being known at the time of writing according to the NASA Exoplanet archive on 18-09-2023 [Akeson et al., 2013] (available at <https://exoplanetarchive.ipac.caltech.edu/index.html>).

1.2 Discovery methods

There are several different methods which can be used to detect exoplanets, all with different strengths, weaknesses and sensitivities to different kinds of exoplanets. The majority of these techniques are indirect as most exoplanets are simply too faint to be detected directly. Figure 1.1 shows how different discovery methods have contributed to the total number of known exoplanets over time. As Figure 1.1 shows

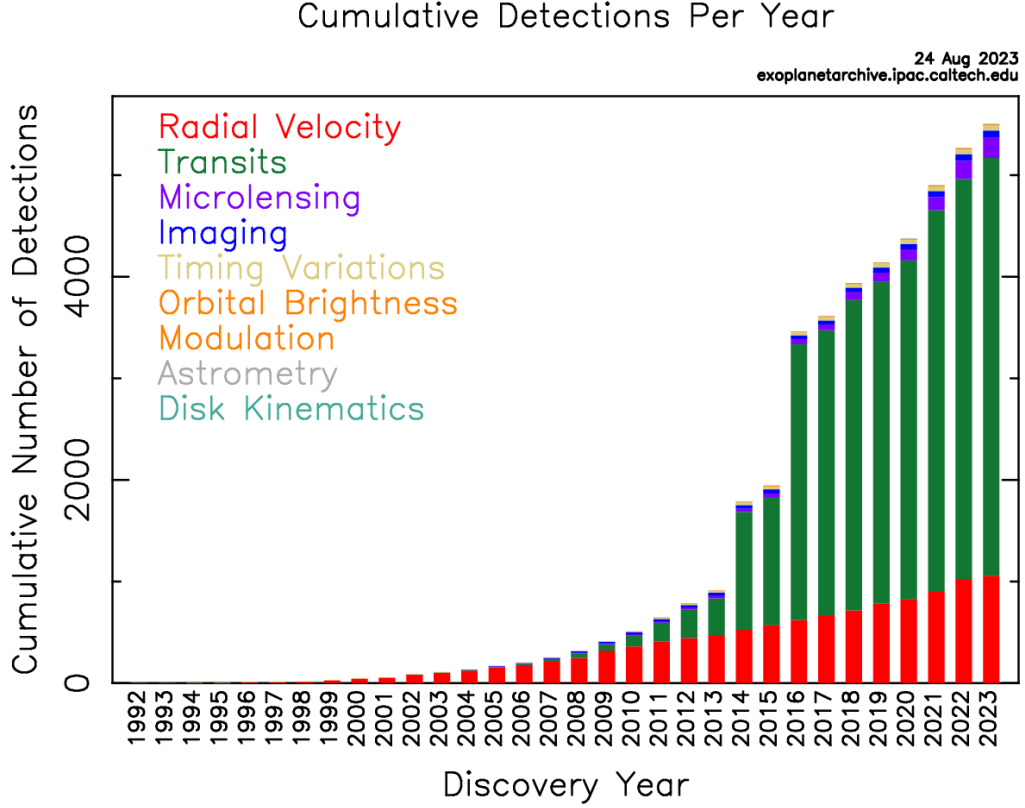


Figure 1.1: Cumulative exoplanet discoveries by discovery method per year. The radial velocity method dominates during the mid-late 2000s before transit surveys begin to take over. The large spikes in 2014 and 2016 are largely due to bulk releases of discoveries from the *Kepler* [Borucki et al., 2010] and K2 [Howell et al., 2014] surveys. Taken from the NASA exoplanet archive [Akeson et al., 2013] on 24-08-2023 (<https://exoplanetarchive.ipac.caltech.edu>)

the majority of exoplanet discoveries come from transits and the next largest set from radial velocities, with relatively few from other methods. In this section we briefly set out the mechanisms of the most prominent methods of exoplanet detection and list some notable discoveries from each. We discuss the transit method only briefly here; a more in depth explanation can be found in Section 1.4.

1.2.1 Direct Imaging

Most exoplanets cannot currently be imaged directly as they reside at extremely small angular separations from their host stars (on the order of 10^{-6} arc-seconds, or around a 10 billionth of a degree) and have extremely low planet/star flux ratios (between 10^{-9} and 10^{-12}). However for a very small population of young, massive, nearby exoplanets it is possible to directly image them rather than using indirect

techniques. Observations are carried out at longer wavelengths where planets are brighter and using a coronagraph to filter out stellar light and leave behind the planetary signal. An example is shown in Figure 1.2. This requires planets which are both relatively bright and at very large orbital separations from their host stars [Currie et al., 2023b]. As such this method is generally biased towards younger and high mass planets which radiate strongly due to the heat released in their formation processes [Nielsen et al., 2019; Vigan et al., 2021]. It is also possible to directly image the protoplanetary disks around young stars from which exoplanets form using instruments like the Atacama Large Millimetre/submillimetre Array [ALMA; ALMA Partnership et al., 2015] and even detect very young planets and protoplanets in those disks [e.g; Keppler et al., 2019]. Despite not being ideal for finding large numbers of exoplanets, direct imaging surveys do produce targets which are very amenable to atmospheric characterisation due to the ability to collect photons directly from the planet [e.g; Konopacky et al., 2013].

The first directly imaged exoplanet is difficult to define as mass estimates change and many exist around the boundary between high mass planets and low-mass brown dwarfs [$\sim 13M_J$ Bowler, 2016]. Some of the earliest detections of planetary mass objects by direct imaging include: 2MASSWJ 1207334-393254 b - which orbits a brown dwarf [Chauvin et al., 2004] and DH Tau b [Itoh et al., 2005; Zhou et al., 2014]. Other significant early detections include the first imaging of a multiplanet system [HR 8799 b, c and d; Marois et al., 2008, see Figure 1.2], the imaging of a planet around the young naked eye star β Pictoris [Lagrange et al., 2010] and one of the first true Jupiter analogues discovered [51 Eridani b; Macintosh et al., 2014].

The first generation of exoplanet direct imaging surveys were completed with instruments such as the Gemini Planet Imager [GPI; Macintosh et al., 2014] and the Spectro-Polarimetric High contrast imager for Exoplanets REsearch [SPHERE; Beuzit et al., 2019]. Space based surveys such as *JWST* [Gardner et al., 2006] are providing higher quality data, allowing for imaging of lower mass planets at smaller orbital separations [e.g; Carter et al., 2023; Feng et al., 2023]. Future Space based direct imaging surveys such as the Habitable Exoplanet Observatory [HabEx; Gaudi et al., 2020] will further improve observations, potentially allowing for imaging of Earth-like or Venus-like planets.

1.2.2 Microlensing

This technique exploits the gravitational lensing effect predicted by Einstein’s general theory of relativity [Einstein, 1936]. Objects on the scale of planets do not produce spatially resolved lensing effects but can increase the brightness of back-

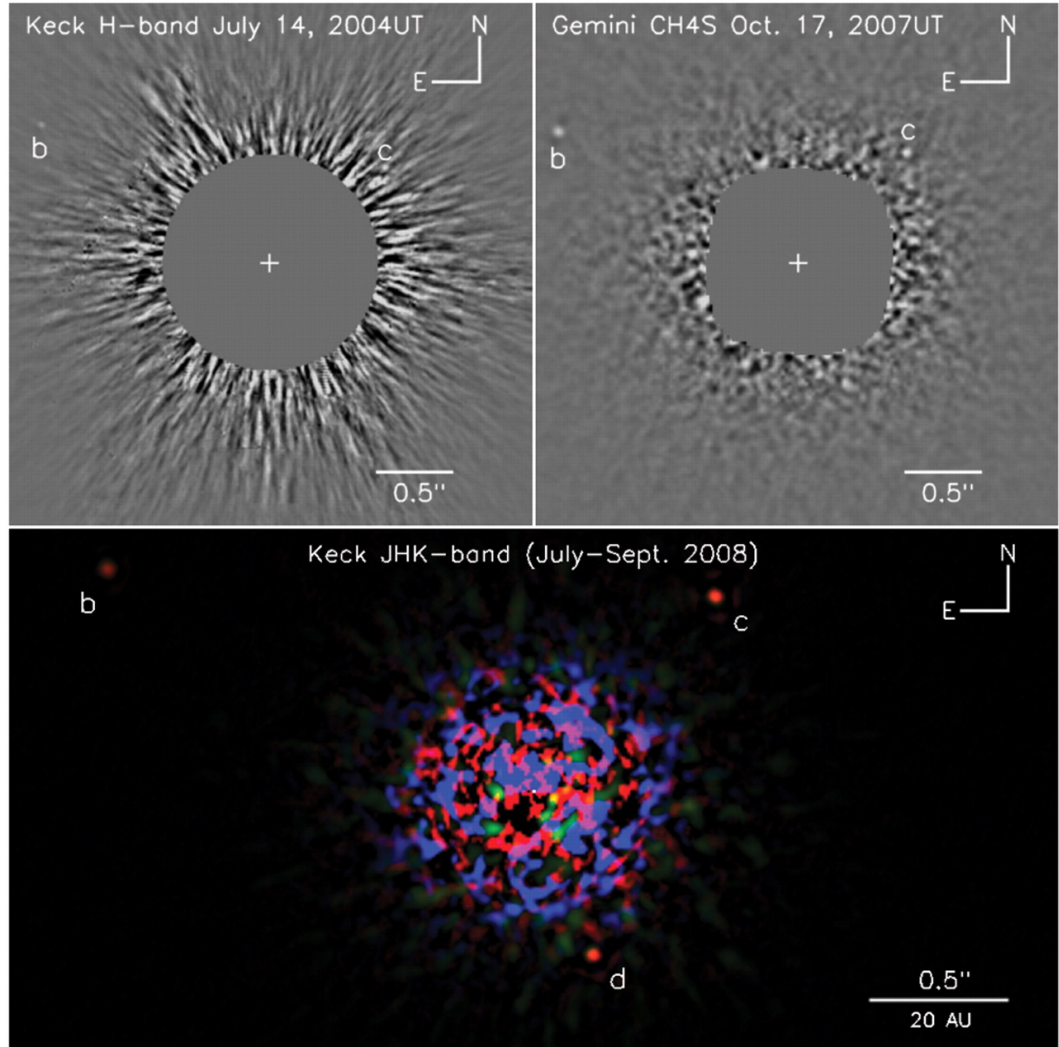


Figure 1.2: HR 8799 b,c and d - the first multiplanet system to be directly imaged shown with light from star removed by ADI processing. Upper left image was taken with a 10m KECK telescope on Mauna Kea, Hawaii, observing in the H wavelength Band in July 2004. Upper right image was taken with the Gemini planet imager in October 2007. The Lower image shows observations from July to September taken across 3 wavelength bands (J, H and K) combined to form a colour image (with the images rotated to account for the orbital motion of planet d during that time). Planet d was hidden in the speckle noise seen in the centre of the images until they were combined. Taken from Marois et al. [2008].

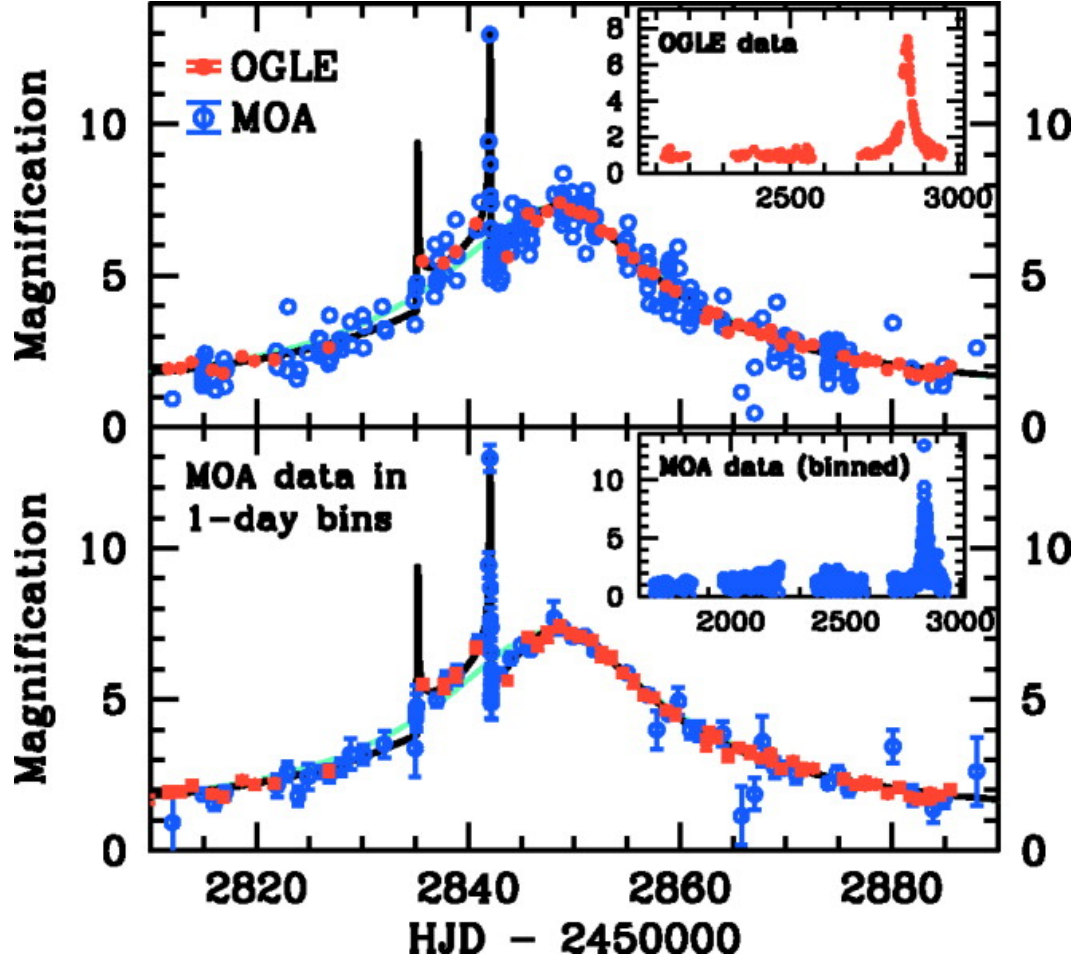


Figure 1.3: Lightcurve of the first widely accepted detection of a planetary microlensing event OGLE 2003-BLG-235/MOA 2003-BLG-53 from Bond et al. [2004]. The underlying curve shape is due to the planet hosting star passing in front of the background star, causing a longer microlensing event, while the two sharp spikes are due to the planet orbiting the lensing star causing additional lensing. OGLE data is shown in red and MOA data in blue, the top panel shows each data set unbinned while the bottom panel shows the MOA data in one day bins. Each panel also has a subpanel showing a much longer time baseline for the OGLE data (top) and MOA data (bottom).

ground objects, such spatially unresolved lensing effects are referred to as microlensing [Paczynski, 1986]. The effect of a planet microlensing a background star as such produces a characteristic peak in the lightcurve of the background star (see Figure 1.3 for an example) which can be used to infer the existence of a planet and its mass [Gould & Loeb, 1992; Gould, 2000]. Photometric surveys have already successfully used microlensing to study planets around the galactic centre such as the Optical Gravitational Lensing Experiment [OGLE; Udalski et al., 2015], the Microlensing Observations in Astrophysics project [MOA; Abe et al., 1997] and the Korean Microlensing Telescope Network [KMTNet; Kim et al., 2016]. OGLE and MOA yielded what is now the earliest widely accepted planetary microlensing event in 2003 [OGLE 2003-BLG-235/MOA 2003-BLG-53; Bond et al., 2004; Bond, 2012, see Figure 1.3]. Since this early discovery, many more likely planetary microlensing events have been observed, although such events are difficult to follow up and confirm with other methods [Bond, 2012]. While the difficulty of follow-up and confirmation can limit the value of individual microlensing discoveries, microlensing surveys can still probe demographics of exoplanets available to no-other technique - including free-floating or "rogue" planets, although the exact population of such exoplanets remains controversial [Mróz et al., 2017; Barclay et al., 2017]. It was also microlensing observations that led to the widely cited prediction that, on average, every star in the Milky Way hosts one or more planets [Cassan et al., 2012].

In the near future, ESA's Euclid mission [Laureijs et al., 2011; Bachelet & Penny, 2019] and NASA's Nancy-Grace-Roman space telescope [previously WFIRST; Akeson et al., 2019] will both perform microlensing surveys from space, allowing for further microlensing discoveries and demographic studies [Bachelet & Penny, 2019; Johnson et al., 2020].

1.2.3 Astrometry

Detection of planets by astrometry uses measurements of the reflex motion of a star due to an orbiting planet. While techniques such as the radial velocity technique (see Section 1.2.4) attempt to indirectly measure this motion via Doppler shift, astrometric measurements seek to use the movement of an object on sky to measure reflex motion. This is a complex process, as other sources of apparent motion of the target star, such as parallax and proper motion due to the orbit of the Sun and the target around the galactic centre, must be removed. At the time of writing, no planets have been discovered primarily by astrometry, but several RV detected planets (see Section 1.2.4) have had their masses measured astrometrically with the Hubble Space Telescope (*HST*) [e.g; Benedict et al., 2002; McArthur et al., 2004;

Benedict et al., 2006; Bean et al., 2007; McArthur et al., 2010, 2014; Benedict et al., 2017, see Figure 1.4]. ESA's *Gaia* mission [Gaia Collaboration et al., 2016, 2018, 2023] has performed astrometry observations of stars across the sky and is expected to yield tens of thousands of exoplanet candidates from astrometry alone [Perryman et al., 2014; Holl et al., 2023; Espinoza-Retamal et al., 2023]. Combined astrometric measurement from *Hipparcos* and *Gaia* [Brandt, 2021] has now been used to measure masses of several exoplanets and to discover new exoplanets [e.g; Kiefer et al., 2021; Brandt et al., 2021; Venner et al., 2021; Currie et al., 2023a; Benedict et al., 2023; de Beurs et al., 2023]

The first attempt to use astrometry to detect an exoplanet was W.S. Jacob's, impressive but ultimately erroneous, claim of an exoplanet around 70 Ophiuchi [Jacob, 1855]. However the technique was first pioneered ~ 10 years earlier by the German astronomer Friedrich Wilhelm Bessel to confirm the existence of unseen binary companions around Procyon and Sirius [Bessel, 1844]. Peter van de Kamp's claims of a planet around Barnard's star were also based on astrometric measurement [van de Kamp, 1963, 1969, 1982].

1.2.4 Radial Velocity method

Similarly to astrometry, the radial velocity (RV) technique uses the reflex motion of a star caused by an orbiting planet. We typically think of a star as a fixed point relative to an orbiting planet, but this is not the case. In reality both planet and star orbit a common centre of mass; however, due to the star's vastly greater mass, this centre is usually inside the star. As such the orbital motion of the star is very small, often colloquially referred to as a "wobble". This wobble is detectable through spectroscopy, as the star's motion towards and away from the observer (i.e. its radial velocity, v_r) causes a measurable wavelength shift in its spectrum due to the Doppler effect [Doppler & Studnica, 1842]. A planet-hosting star will show a periodic sinusoidal variation in its radial velocity measurements over time. If the orbital period of the planet is known, the radial velocity curve can be "folded" along the orbital period of the planet, producing an RV phase curve (see Figures 1.5 and 1.6 for examples). The peak of the RV phase curve, the semi-amplitude ($K = (v_{r,\max} - v_{r,\min})/2$) is given by the following equation from Lovis & Fischer [2010]:

$$K = \sqrt{\frac{G}{1-e^2}} \frac{M_p \sin i}{\sqrt{M_\star + M_p}} \frac{1}{\sqrt{a}}, \quad (1.1)$$

where G is the gravitational constant, e is the orbital eccentricity, i is the orbital inclination relative to an observer, M_\star, M_p are the masses of the star and

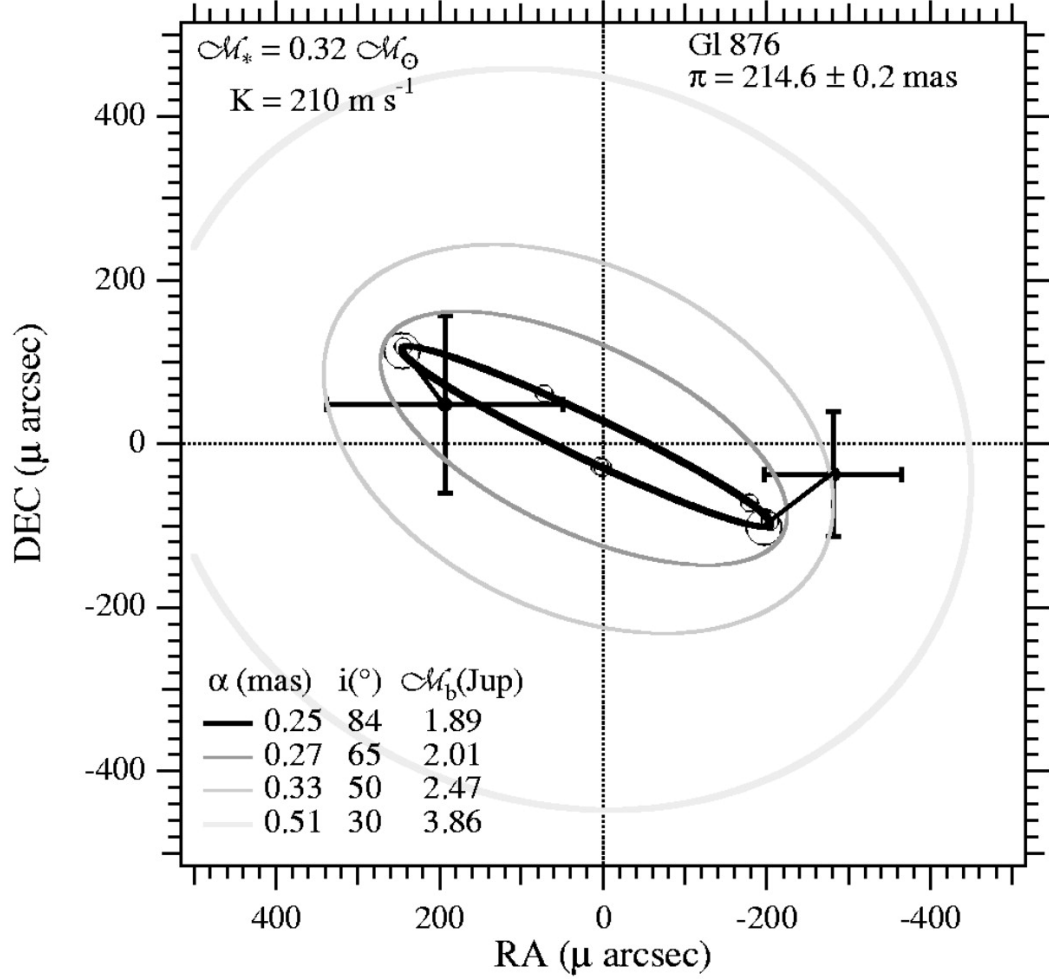


Figure 1.4: Four orbital models for the sky motion of GI 876 due to the perturbation of an orbiting planet with different masses and inclinations are shown as increasingly dark concentric ellipses. The innermost model is the result of the combined astrometric and RV solution. Also shown are points of astrometric measurements with errors taken at orbital phase 0.26 (periastron; lower right) and 0.74 (upper left). Lines are drawn connecting the measured points to the expected values based on the innermost model.

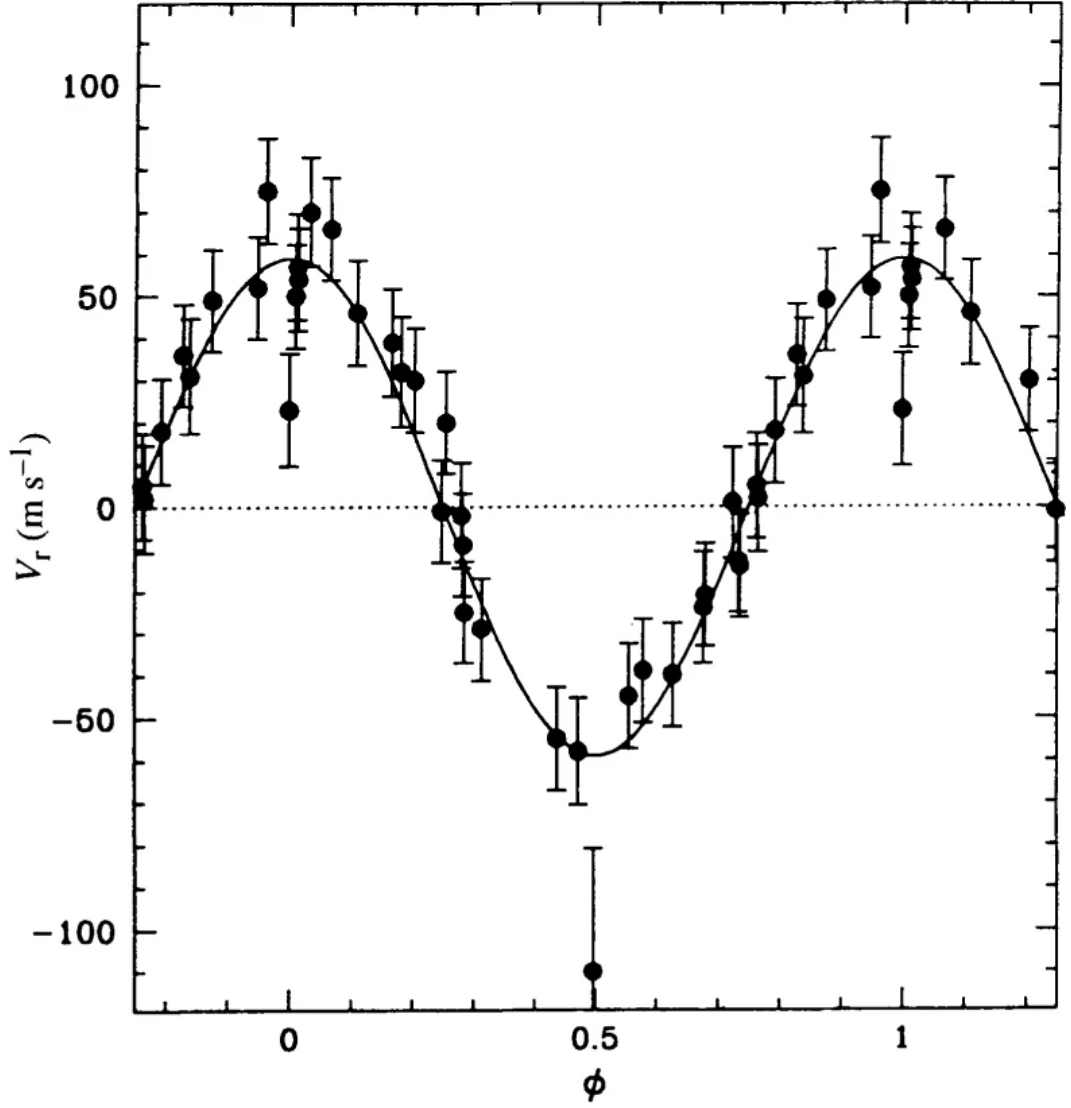


Figure 1.5: Radial velocity curve of the hot-Jupiter host star 51 Pegasi, folded to orbital period of 51 Pegasi b (4.23 days). Radial velocity data points from the ELODIE spectrograph are shown in black with error bars. A best fit sinusoidal model is drawn through the data points. Note the shape of the curve is sinusoidal, due to the low eccentricity of the system ($e \approx 0$). Taken from Mayor & Queloz [1995].

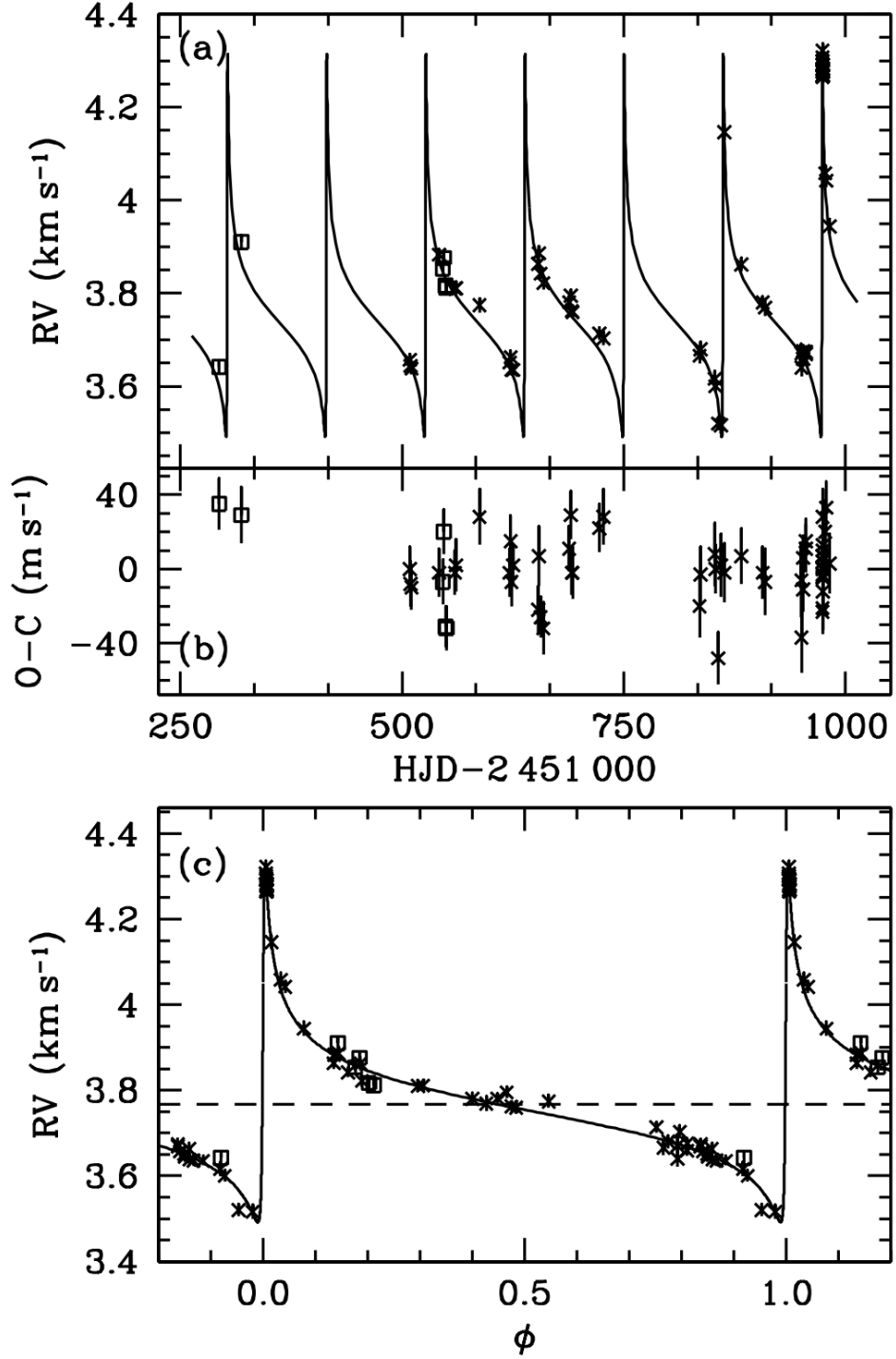


Figure 1.6: Radial velocity phase curve of HD 80606. Folded to a period of 111 days. ELODIE data shown with crosses and *HIRES* data with open squares. Note the extremely irregular shape of the sinusoidal curve due to the high eccentricity ($e \approx 0.93$). Taken from Naef et al. [2001].

planet respectively and a is the semi-major axis of the orbit (effectively the average orbital separation). If the mass of the star is known, the orbital period measured from the RV phase curve can be used to calculate a using Kepler's third law [Kepler, 1609], and the eccentricity can be estimated from the shape of the phase curve [Wright & Gaudi, 2013]. The effect of eccentricity on phase curve shape can be seen via a comparison between the real examples of the high eccentricity phase curve shown in Figure 1.6 and the low eccentricity phase curve shown in Figure 1.5. This allows for a lower limit of the planet's mass, $M_p \sin i$, to be calculated. If the orbital inclination is known, usually through transit measurements (see Sections 1.2.5 and 1.4), then the mass of the planet can be constrained.

The earliest RV detection is also the first exoplanet detected around a solar-type main sequence star, 51 Pegasi b [Mayor & Queloz, 1995] - see Figure 1.5 - which was found using the "ELODIE" spectrograph [Baranne et al., 1996]. RV detections are also responsible for the discovery of the first true Jupiter Analogue [HIP 11915 b; Bedell et al., 2015] and the 55 Cancri system [Fischer et al., 2008] which includes the first "super-Earth" exoplanet (see Section 1.3) found around a main sequence star [55 Cancri c; McArthur et al., 2004]. Other notable RV discoveries include HD 80606 b - a giant planet on a highly eccentric ~ 100 day orbit [Naef et al., 2001, see Figure 1.6] and Proxima Centauri b, an earth-sized, potentially-temperate planet which orbits the nearest star to the sun, making it the nearest exoplanet to the Earth [Anglada-Escudé et al., 2016].

Radial velocity spectrographs used for planet detection include; the High Accuracy Radial-velocity Planet Searcher [*HARPS*; Mayor et al., 2003], the Echelle SPectrograph for Rocky Exoplanets and Stable Spectroscopic Observations [*ESPRESSO*; Pepe et al., 2010], the High-Resolution Echelle Spectrometer [*HIRES*; Vogt et al., 1994] and the Fiberfed Extended Range Optical Spectrograph [*FEROS*; Kaufer et al., 1999].

1.2.5 Transit method

The exoplanet detection method responsible for the most discoveries to date, the transit method relies on a planet passing between the line of sight of an observer and its host star causing a measurable decrease in the star's brightness. The idea that such "shadowing" could occur due to an exoplanet was predicted as early as 1698 by Christiaan Huygens [Huygens, 1698]. The amount of dimming can be used to calculate planetary radius and the time between transit events can indicate the orbital period [Winn, 2014]. Since the first detection of an exoplanet transit [HD 209458 b; Charbonneau et al., 2000] and the first exoplanet discovery via transit

[OGLE-TR-56 b; Konacki et al., 2003], thousands of transiting exoplanets have been discovered [NASA Exoplanet Archive; Akeson et al., 2013].

The transit method lies at the heart of this thesis research, and therefore a detailed explanation of exoplanet transits is presented in Section 1.4 and examples of transit surveys are described in Sections 1.5 and 1.6.

1.3 Exoplanet demographics

Our known sample of exoplanets has grown to the point where we are now able to make inferences about the entire underlying population of exoplanets including the occurrence rates of planets of different sizes and orbital separations around different host stars [e.g.; Dressing & Charbonneau, 2013, 2015; Fressin et al., 2013; Hsu et al., 2019; Kunitomo & Matthews, 2020; Bryant et al., 2023]. This is largely due to the advent of space based surveys such as *Kepler* [Borucki et al., 2010] and the Transiting Exoplanet Survey Satellite [*TESS*; Ricker et al., 2015]. This large sample contains a wide and exotic variety of exoplanets, some similar to those in our own Solar System and others utterly unlike them.

1.3.1 Super-Earths and Mini-Neptunes

One of the most surprising discoveries has been the huge population of planets between the size of Earth and Neptune ($1R_{\oplus} < R_p < 4R_{\oplus}$), made up of large terrestrial planets known as "super-Earths" [e.g.; Gandolfi et al., 2018; Huang et al., 2018b; Maciejewski et al., 2023; Hawthorn et al., 2023b] and small gaseous/icy planets commonly called "mini-Neptunes" [e.g.; Barros et al., 2023; Hawthorn et al., 2023b,c]. These populations are perhaps better distinguished in terms of radius since composition is difficult to determine and radius can be measured directly. Mass and radius measurements have determined that the boundary between these two populations lies between $1.5\text{--}2R_{\oplus}$ [Lopez & Fortney, 2014; Rogers, 2015; Chen & Kipping, 2017]. The relatively low occurrence rate of planets on short periods in this range of radii between the two populations is also referred to as the "radius valley" [Owen & Wu, 2017]. Both populations can be seen in the lower left regions of Figures 1.7 and 1.8. No planets fitting either of these categories exist in the Solar System and yet they appear to be some of the most numerous planets in our galaxy [Fressin et al., 2013; Hsu et al., 2019; Kunitomo & Matthews, 2020].

Mass — Period Distribution

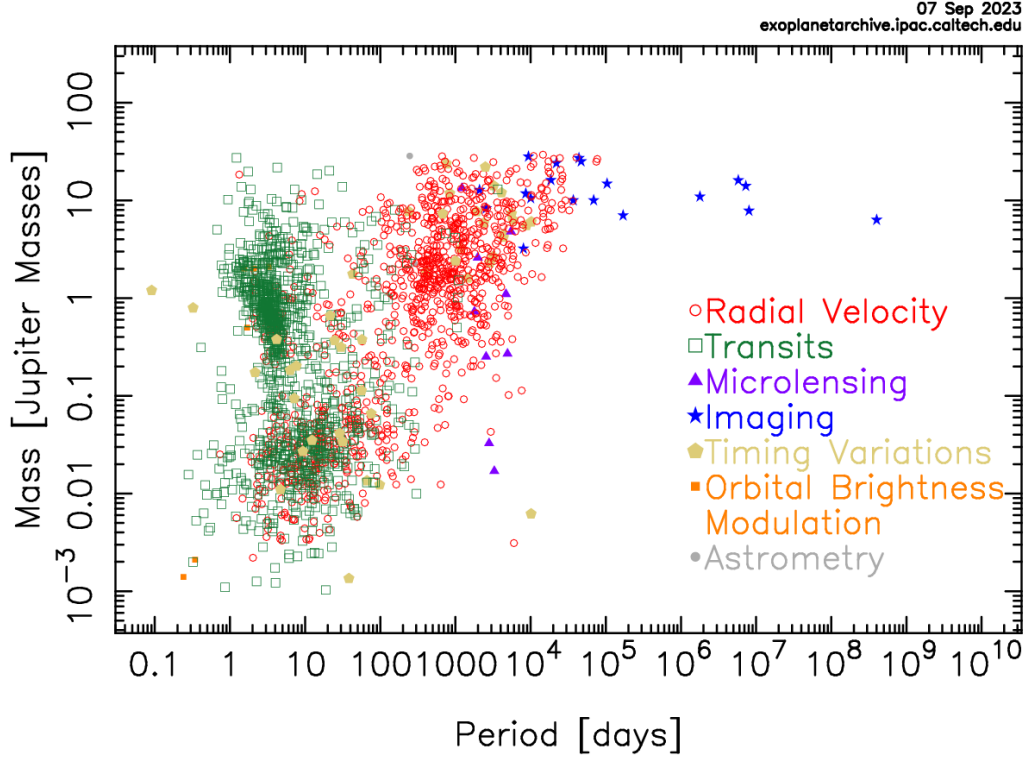


Figure 1.7: Distribution of known exoplanets in mass-period space. The "hot-Jupiter" population can be seen clustered at periods below 10 days and around 1 Jupiter mass and above. Compared to these, fewer intermediate period (10-200 day) giant planets (i.e. "warm-Jupiters") can be seen from transits due to observational biases. The clump of objects between 0.01 and 0.1 Jupiter masses are the "mini-Neptunes" and "super-Earths". Note the lack of planets with intermediate masses and periods below 10 days, this sparse region of parameter space is often called the "Neptunian desert" Mazeh et al. [2016]. Taken from the NASA exoplanet archive [Akeson et al., 2013].

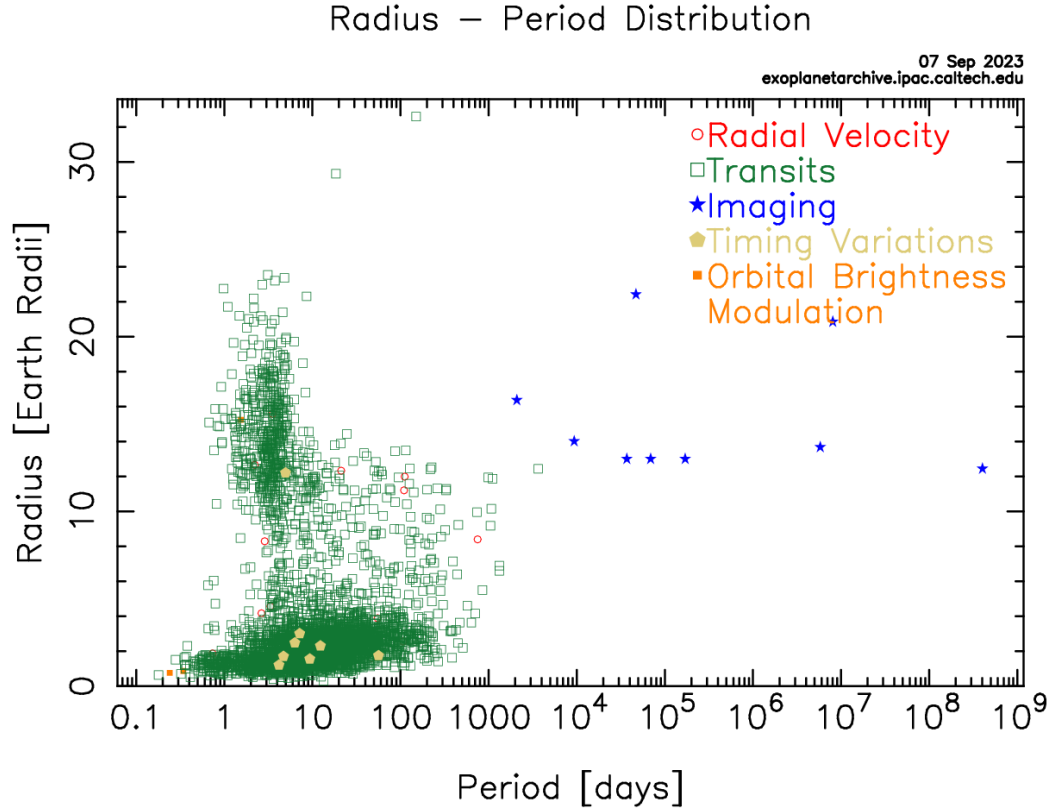


Figure 1.8: Distribution of known exoplanets in radius-period space. The "hot-Jupiter" population is seen clustered at periods ≤ 10 days and above 10 Earth radii. Comparatively fewer "warm-Jupiter" type giant planets with periods between 10 and 200 days are seen. This is due to the observational biases of transit photometry - the method via which the vast majority of exoplanets with known radii are discovered. The so called "super-Earths" and "mini-Neptunes" are seen between 1 and 4 Earth radii. Note the lack of planets with radii between roughly 2 and 10 Earth radii and periods less than 10 days; this sparse region of parameter space is often called the "Neptunian desert" [Mazeh et al., 2016]. Taken from the NASA exoplanet archive [Akeson et al., 2013].

The Neptune Desert

We have also found a relative lack of intermediate sized planets comparable to Neptune on short-orbits; this so called Neptune desert [Mazeh et al., 2016] can be seen in Figures 1.7 and 1.8.

1.3.2 Hot Jupiters

We have also discovered numerous examples of giant planets, similar in size to Jupiter but incredibly close to their host stars with orbital periods of a few days or less [e.g.; Mayor & Queloz, 1995; Charbonneau et al., 2000; Hellier et al., 2009; Buchhave et al., 2010; Maxted et al., 2011; Hellier et al., 2011; Gaudi et al., 2017; Yee et al., 2023] (for reference shortest orbital period in the solar system; that of Mercury, is ~ 88 days). These so-called "hot-Jupiters" (on account of their very high equilibrium temperatures on the order of 1000K) are shown clustered in the upper left regions of Figures 1.7 and 1.8.

At such short periods the dynamics of these systems are dominated by tidal interactions between the planet and host star [Mardling, 2007; Valsecchi et al., 2015], resulting in damping of orbital eccentricities leading to highly circularised orbits, which is reflected in the absence high eccentricity short-period exoplanets [Winn & Fabrycky, 2015]. Although this is also partially due to the fact that eccentric short-period orbits are often physically impossible and would bring the planet too close to the star to maintain an orbit without falling onto the star due to its immense gravity. These tidal interactions heat up the planet alongside irradiation from the host star creating very high temperatures and inflating the planetary radius, leading to high numbers of super large radii planets with periods ≤ 10 days as seen in Figure 1.8 [Mardling, 2007; Batygin & Stevenson, 2010; Demory & Seager, 2011; Perna et al., 2012]. These tidal interactions also mean that hot-Jupiters should be tidally locked (i.e. their spin period is the same as their orbital period) causing them to have a permanent dayside which is always irradiated by their host star.

Hot-Jupiters are very unlikely to have formed in-situ and are thus predicted to experience inward migration. Two main pathways are predicted for this; gas-disk migration and high eccentricity tidal migration [Dawson & Johnson, 2018]. Gas-disk migration is caused by torque exerted on a young planet or protoplanet by gas in the protoplanetary disk causing the semi-major axis of its orbit to dramatically shrink [Bitsch et al., 2013; Duffell et al., 2014; Dürmann & Kley, 2015]. Meanwhile, high eccentricity migration is predicted to occur when a giant planet is perturbed into a highly eccentric orbit, leading to a loss of angular momentum over time from

tidal interactions as the planet approaches its host star [Ford & Rasio, 2006; Fabrycky & Tremaine, 2007; Petrovich, 2015; Xiang-Gruess, 2016]. However, the strong tidal interactions experienced by hot-Jupiters tend to remove traces of past dynamical interactions from the planet's orbit, leaving only obliquity measurements (see Section 1.4.3) as a way of distinguishing between possible formation and migration mechanisms.

1.3.3 Warm Jupiters

While radial velocity and direct imaging surveys (see Sections 1.2.1 and 1.2.4) have found numerous giant planets on longer orbits ($P > 10$ days), transit surveys have recovered relatively few such systems as can be seen in Figures 1.7 and 1.8. Recent works are, however, beginning to recover such planets from transit surveys [Particularly from *TESS* (see Section 1.6) e.g; Gill et al., 2020; Ulmer-Moll et al., 2022; Grieves et al., 2022; Mann et al., 2023; Gupta et al., 2023; Brahm et al., 2023; Dong et al., 2023]. These so called "warm-Jupiters" are, as their name implies, cooler than their hot-Jupiter cousins due to greater separation from their host stars. They also experience significantly less tidal interaction than hot-Jupiters and therefore show a wider range of eccentricities [Winn & Fabrycky, 2015] and are unlikely to be tidally locked. This means that, unlike hot-Jupiters, it is possible to infer dynamical histories of warm-Jupiters from their current orbital elements. It has been theorised that while some warm-Jupiters are "proto" hot-Jupiters and migrating inwards, others may be part of a distinct population, experiencing their own formation and migration pathways [Wu & Lithwick, 2011; Petrovich, 2014; Mustill et al., 2017a]. Huang et al. [2016] found that warm-Jupiters have more close companions than hot-Jupiters and Dong et al. [2021] found two distinct populations of low eccentricity and high eccentricity warm-Jupiters. Both of these trends provide evidence that at least some warm-Jupiters are experiencing distinct formation and migration mechanisms to hot-Jupiters. Additionally, obliquity measurements (see Section 1.4.3) by Rice et al. [2022] have shown that a small subset of warm-Jupiters are more aligned than hot-Jupiters which provides additional evidence, however it remains to be seen whether this trend extends to the warm-Jupiter population as a whole.

Warm-Jupiters are also likely to have distinct atmospheric properties from hot-Jupiters. Due to their rotation period not being tidally locked, rotational periods of warm-Jupiters are expected to dominate their atmospheric dynamics - potentially leading to more efficient atmospheric heat redistribution as has been seen in brown dwarfs [Tan & Showman, 2021]. Lower stellar irradiation and resulting cooler equilibrium temperatures should also have significant effects on atmospheric

dynamics and chemistry [Gao et al., 2017; Fortney et al., 2020; Hu, 2021]. Additionally, such planets are likely to experience less photoevaporation of their atmospheres than shorter-period planets [e.g; Hawthorn et al., 2023b,c; Osborn et al., 2023a], thus retaining more of their primordial atmospheres and allowing for a more accurate characterisation of their formation through atmospheric measurement (see Section 1.4.3) of their Carbon to Oxygen [C/O] ratios or comparing bulk Nitrogen concentrations to Ammonia [Öberg et al., 2011; Öberg et al., 2013; Ohno & Fortney, 2023; Öberg et al., 2023].

Warm-Jupiters are also promising candidates in the search for exomoons and exorings, which have not yet been detected but are theoretically detectable around giant transiting planets [Barnes & Fortney, 2004; Kipping et al., 2009; Simon et al., 2012; Aizawa et al., 2017]. Exomoons and exorings are predicted to be more stable and thus likelier to exist around longer-period planets with greater orbital separations [Barnes & O’Brien, 2002; Barnes & Fortney, 2004; Cassidy et al., 2009; Dobos et al., 2021; Makarov & Efroimsky, 2023].

1.4 Transits 101

The transit method is the most successful method for detecting exoplanets at the time of writing (see Section 1.2.5 and Figure 1.1). Transits allow for the radius, orbital period and inclination of an exoplanet to be constrained. When coupled with radial velocity measurements this allows for determination of the bulk density. Additionally it is possible to measure the atmospheric compositions of transiting exoplanets via transmission spectroscopy (see Section 1.4.3).

1.4.1 Transit Geometry

In astronomy, an *eclipse* refers to the obscuring of one object by another object passing between it and the line of sight of an observer. In the case where one object is much larger than the other (such as a planet and its host star) the obscuring of the larger body by the smaller one is referred to as a *transit* and the reverse case where the larger object obscures the smaller one as an *occultation* as shown in Figure 1.9. Although planets and stars are spherical objects in reality, it is perfectly appropriate to consider them as 2-dimensional circular disks for the purposes of modelling transits.

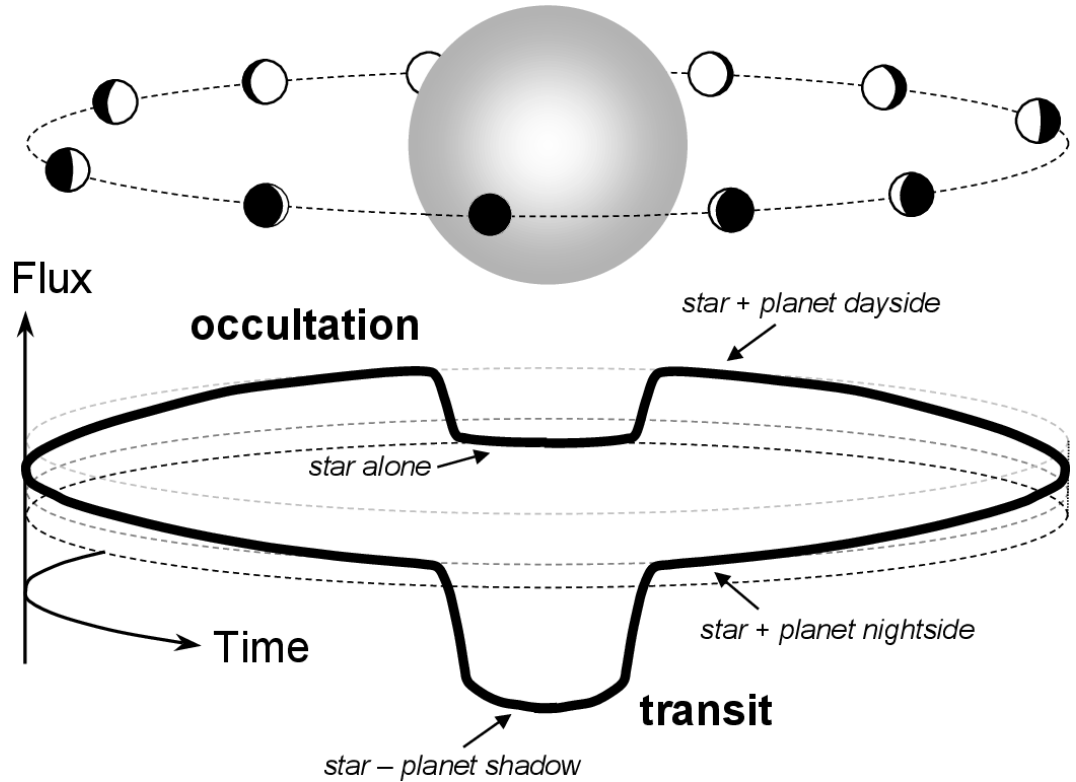


Figure 1.9: Overview of changes in flux as a function of orbital phase for a typical transiting exoplanetary system. The transit is shown when the planet passes in front of the star with a round bottomed shape due to limb darkening. The occultation occurs when the planet passes behind the star, and is much shallower and more flat bottomed than the transit. Note that this diagram is based on a short-period system which is tidally locked and longer period systems will not necessarily have a fixed day and nightside with orbital phase. Taken from Winn [2014].

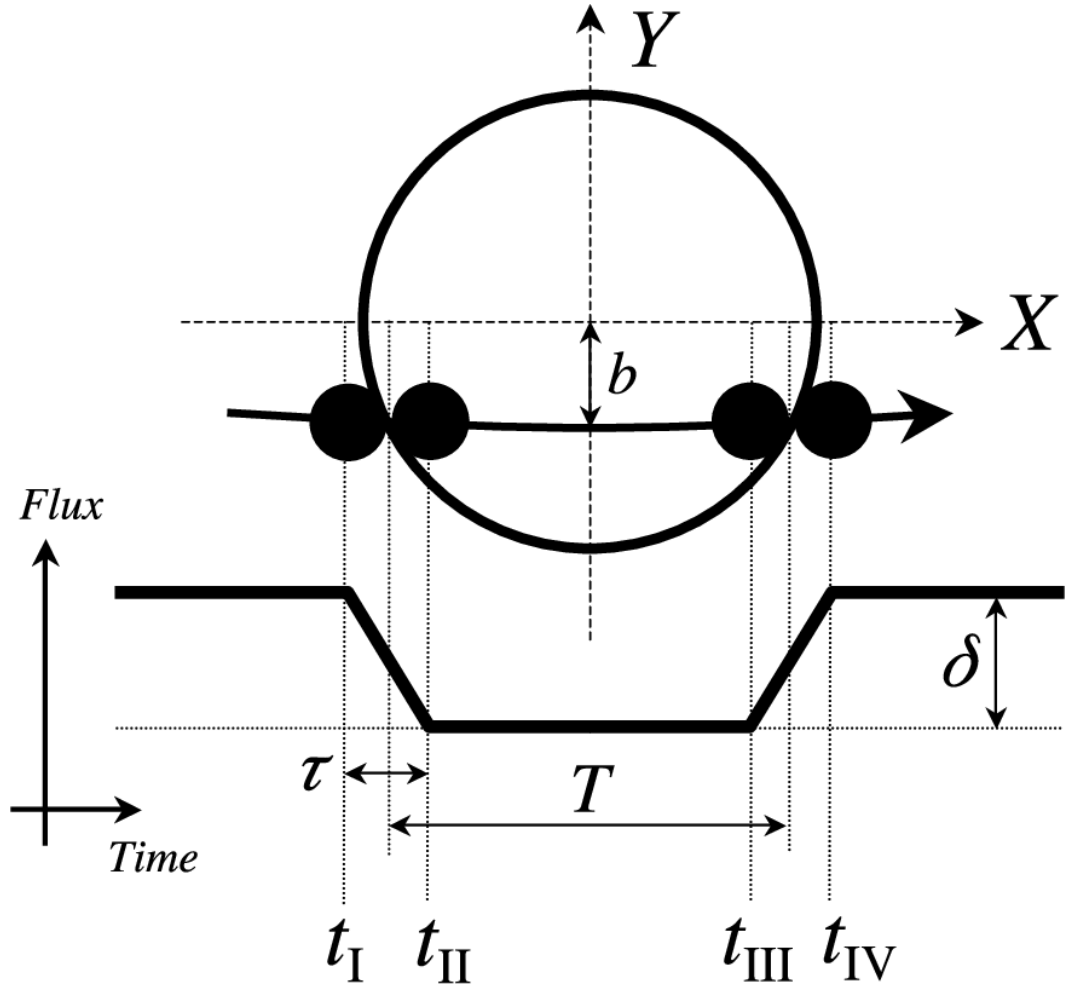


Figure 1.10: Two-dimensional representation of transit geometry showing the impact parameter (b), the depth of transit (δ) and the times of contact between the stellar and planetary disks (t_I, t_{II}, t_{III} , and t_{IV}). Taken from Winn [2014].

Impact Parameter

When discussing transits, it is vital to understand whether the planet crosses closer to the equator of the stellar disk or the very edge (usually referred to as the "limb" of the star) from the perspective of an observer. This is quantified by the *impact parameter* (b ; see Figure 1.10) which is defined as the sky projected distance from the equator of the planetary disk to the equator of the stellar disk at conjunction and is given by the following equation from Winn [2014]:

$$b = \frac{a \cos i}{R_\star} \left(\frac{1 - e^2}{1 - e \sin \omega} \right). \quad (1.2)$$

The impact parameter is commonly used in conjunction with the radius ratio between the planet and star ($k = \frac{R_p}{R_\star}$) to define whether a planet transits and whether the transit is full (the full disk of the planet crosses the star) or partial. A full transit is defined as $0 \leq |b| < (1 - k)$ while a partial or "grazing" transit is defined by $(1 - k) \leq |b| \leq (1 + k)$.

Transit Depth

The depth of transit (δ ; see Figure 1.10) is equal to the proportion of stellar light blocked by the transiting planet. In the case of a full transit ($0 \leq |b| < (1 - k)$), assuming that the flux from the planet itself during transit is negligible, as is overwhelmingly often the case, then this is proportional to the square of the ratio of the radii of the planet and star (R_p and R_\star , respectively):

$$\delta = k^2 = \left(\frac{R_p}{R_\star} \right)^2. \quad (1.3)$$

For a grazing transit ($(1 - k) \leq |b| \leq (1 + k)$) calculating the depth of transit is more complex and relies on modelling the conjunction of two spheres. Firstly we must calculate the true anomaly (i.e. the angular position of the planet in its orbit) and then calculate the corresponding projected separation of the planet and star on the sky. We can then calculate the depth of transit by determining the area of the stellar disk covered by the planetary disk as a fraction of the total area of the stellar disk [Hilditch, 2001]. Software tools are available for these types of calculations [e.g; Maxted, 2016].

Duration of transit

There are two ways to define the duration of transit. Either the total duration of transit (T_{tot}), or the duration of transit at full depth only (T_{full}). The former case

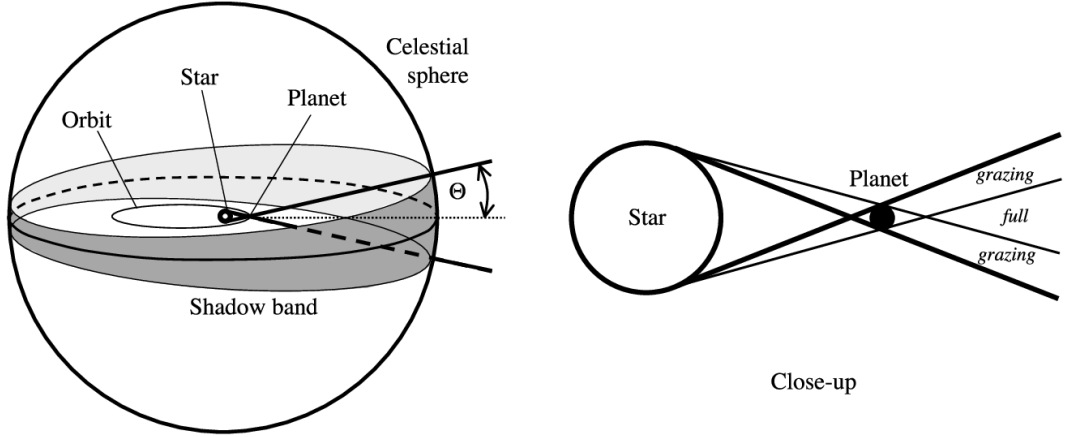


Figure 1.11: Demonstration of the solid angle swept through space by a planet's shadow in 3 dimensions (left) and 2 dimensions (right). To see a transit, an observer must be in the shadow region, as such the probability of transit is the probability that the system is inclined such that we are in its shadow band. Taken from Winn [2014]

(T_{tot}) can be defined as the time between the first and fourth points of conjunction between the planetary and stellar disks (t_I, t_{IV} ; see Figure 1.10) and is calculated using the following equation from Winn [2014]:

$$T_{\text{tot}} = T_{14} = t_{IV} - t_I = \frac{P_{\text{orb}}}{\pi} \arcsin \left[\frac{R_{\star}}{a} \frac{\sqrt{\left(1 + \frac{R_p}{R_{\star}}\right)^2 - b^2}}{\sin i} \right] \frac{\sqrt{1 - e^2}}{1 + e \sin \omega}. \quad (1.4)$$

Conversely, the latter case (T_{full}), is defined as the time between the second and third points of conjunction (t_{II}, t_{III} ; see Figure 1.10) and is calculated as follows [Winn, 2014]:

$$T_{\text{full}} = T_{23} = t_{III} - t_{II} = \frac{P_{\text{orb}}}{\pi} \arcsin \left[\frac{R_{\star}}{a} \frac{\sqrt{\left(1 - \frac{R_p}{R_{\star}}\right)^2 - b^2}}{\sin i} \right] \frac{\sqrt{1 - e^2}}{1 + e \sin \omega}. \quad (1.5)$$

Probability of transit

For a transit to occur the orbit of the planet must be aligned such that it passes directly between its host star and the line of sight of an observer, thus casting a shadow on the observer. The cone this shadow sweeps through space is illustrated in Figure 1.11. To observe a transit, the observer must be within the region of space swept out by the shadow cone. This can also be expressed as the transit meeting the condition $|b| < (1 \pm k)$, where using $+$ allows for grazing transits and $-$ allows only full transits. With this condition, the probability of transit can be expressed using the following equation from Winn [2014]:

$$p_{\text{tra}} = \left(\frac{R_{\star} \pm R_{\text{p}}}{a} \right) \left(\frac{1 + e \sin \omega}{1 - e^2} \right). \quad (1.6)$$

Where once again using $+$ allows for partial transits and $-$ does not. The probability of transit is inversely proportional to the orbital separation, and as such, planets with very close orbits are much more likely to transit. It is for this reason that transit surveys are highly biased towards shorter period planets as they are closer to their host stars and thus more likely to transit.

1.4.2 Transit observations

High precision time-series relative photometry is used to monitor transit events. To demonstrate a typical transiting exoplanet lightcurve and to briefly describe the reduction and processing of such data we use the example of the *TESS* (see Section 1.6) full phase curve of the *WASP*-18 system by Shporer et al. [2019]. A transit lightcurve is the result of taking a series of images of a target star at regular time intervals and using these to extract the flux from the star at each timestamp. This results in an unfolded "raw" lightcurve such as that shown in Figure 1.12.

In the case of a planet with multiple observed transits like *WASP*-18b, the data is phase-folded (similarly to an RV curve, see Section 1.2.4) along the orbital period of the planet, which is obtained by measuring the time between sequential transits. The resulting phase-folded lightcurve for *WASP*-18 is shown in Figure 1.13.

1.4.3 Additional science from transits

Transit detections allow for unique opportunities to characterise exoplanets and probe their formation and migration histories, especially for transiting exoplanets which orbit bright, nearby host stars. Two important methods for exoplanet characterisation of transiting systems are atmospheric transmission spectroscopy and

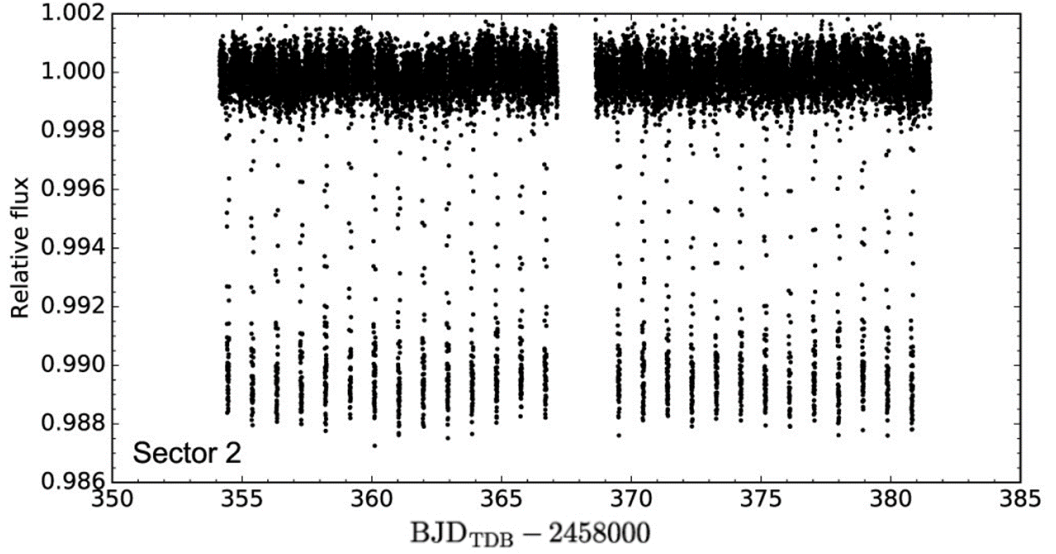


Figure 1.12: Unfolded normalised *TESS* sector 2 lightcurve of *WASP-18* from Shporer et al. [2019]. Transits occur every ~ 0.94 days with a depth of $\sim 1.2\%$. Note that the flux value has been normalised from a value in $\text{e}^- \text{s}^{-1}$ to a value where the out of transit flux = 1. The gap in the middle of observations is caused by the *TESS* data upload every 13.7 days.

spin-obliquity measurement.

Atmospheric Transmission Spectroscopy

Transmission spectroscopy is performed by measuring the transit depth at different wavelengths of light and recording the depth as a function of wavelength producing a transmission spectrum. Molecules in the atmosphere of the exoplanet absorb different wavelengths of light, leaving characteristic absorption features in the transmission spectrum. This method allows for direct measurement of the atmospheric properties of exoplanets orbiting host stars of sufficient brightness to produce high signal-to-noise spectra [Winn, 2014; Madhusudhan, 2019]. Transmission spectroscopy is regularly used to characterise exoplanet atmospheres [e.g; Charbonneau et al., 2002; JWST Transiting Exoplanet Community Early Release Science Team et al., 2023; Mikal-Evans et al., 2023].

Spin-Obliquity measurements

It is additionally possible to measure the alignment between the orbit of a transiting exoplanet and the spin axis of its host star via RV measurements (see Section 1.2.4)

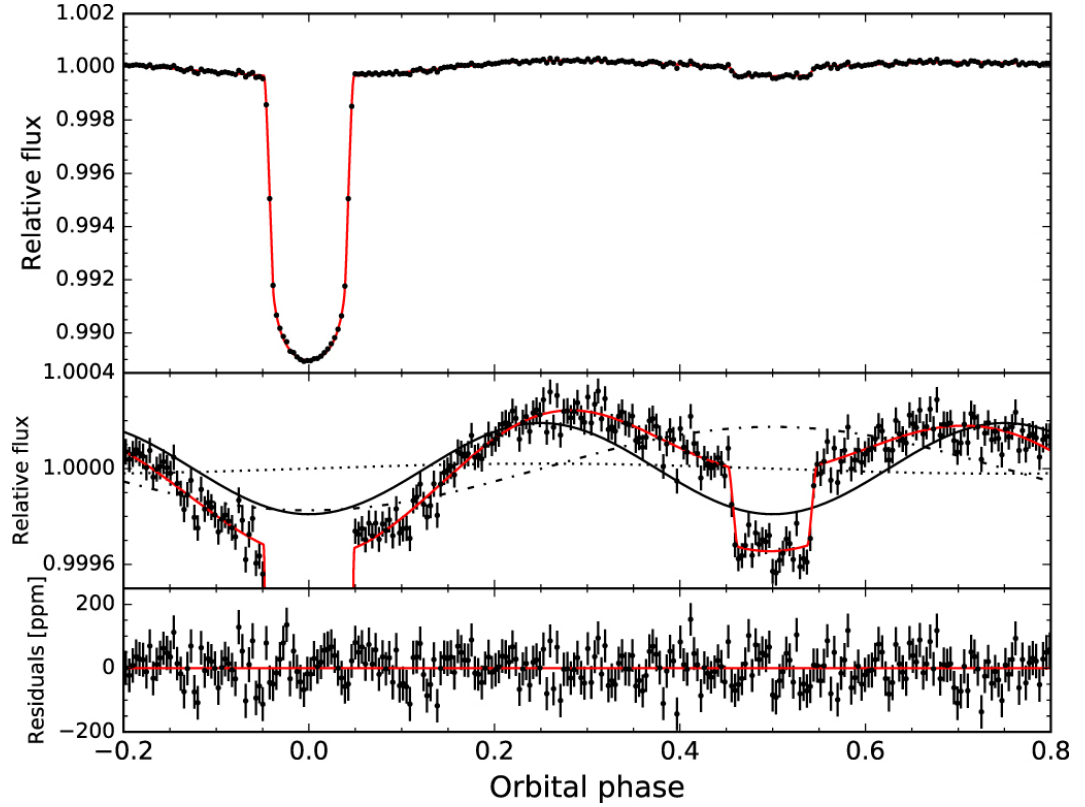


Figure 1.13: *TESS* phase curve of *WASP*-18 system folded to the period of *WASP*-18b (0.94 days) from Shporer et al. [2019]. *TESS* data points are shown in black with a best fit model shown in red. The top panel shows the deep U shaped transit at phase 0 and the shallower occultation at phase 0.5. The U shape of the transit is due to limb darkening. The middle panel shows a zoomed in view of the occultation and models for the effects of ellipsoidal (solid line), atmospheric brightness (dot-dashed line) and doppler beaming (dotted line) modulations on the out-of-transit flux.

of the Rossiter-McLaughlin effect [RM; Rossiter, 1924; McLaughlin, 1924]. This allows for inferences on possible migration and formation pathways the planet may have experienced in its past [Triaud, 2018].

1.5 Transit surveys

Since the first detection of an exoplanet transit [HD 209458 b; Charbonneau et al., 2000] and the first discovery of an exoplanet via transit [OGLE-TR-56 b; Konacki et al., 2003], numerous ground and space based surveys have found thousands of additional transiting exoplanets [Source: NASA Exoplanet Archive; Akeson et al., 2013]. It is also worth noting that other photometric surveys, such as those searching for gravitational microlensing events (see Section 1.2.2), have also incidentally discovered transiting exoplanets [e.g; Konacki et al., 2003].

1.5.1 Ground-based surveys

The first dedicated surveys for transiting exoplanets were carried out from the ground. Among the most notable of these was the Wide Angle Search for Planets [*WASP*; Pollacco et al., 2006]. Each *WASP* instrument consisted of eight ~ 11 cm aperture Canon telephoto lenses each with mounted Charged Coupled Devices (CCDs) mounted to a robotic armature as shown in Figure 1.14. The *WASP* survey yielded numerous "hot-Jupiter" type exoplanets around nearby bright host stars, among which are some of the most well studied exoplanets known [e.g; Collier Cameron et al., 2007; Pollacco et al., 2008; Hebb et al., 2009; Hellier et al., 2009; Hebb et al., 2010; Faedi et al., 2011; Hellier et al., 2014]. Another notable early ground based survey is the Kilodegree Extremely Little Telescope [*KELT*; Pepper et al., 2007]. *KELT* is responsible for the discovery of *KELT*-9b, one of the most extremely irradiated known hot-Jupiters with an estimated equilibrium temperature above that of some M and K type stars [Gaudi et al., 2017]. Also of note are the Hungarian Automated Telescope Network [*HATNet*; Bakos et al., 2004] facilities and the Antarctic Search for Transiting ExoPlaneTs [*ASTEP*; Crouzet et al., 2010]. One of the most exciting exoplanetary discoveries has come from the TRAnsiting Planets and Planetesimals Small Telescope [*TRAPPIST*; Jehin et al., 2011] survey, which discovered a system of seven terrestrial planets, with three in the temperate zone, in close resonant orbits around the small nearby star *TRAPPIST*-1 [Gillon et al., 2017].

The next generation of transit surveys is being led by the aptly named Next Generation Transit Survey [*NGTS*; Wheatley et al., 2018]. *NGTS* consists of twelve

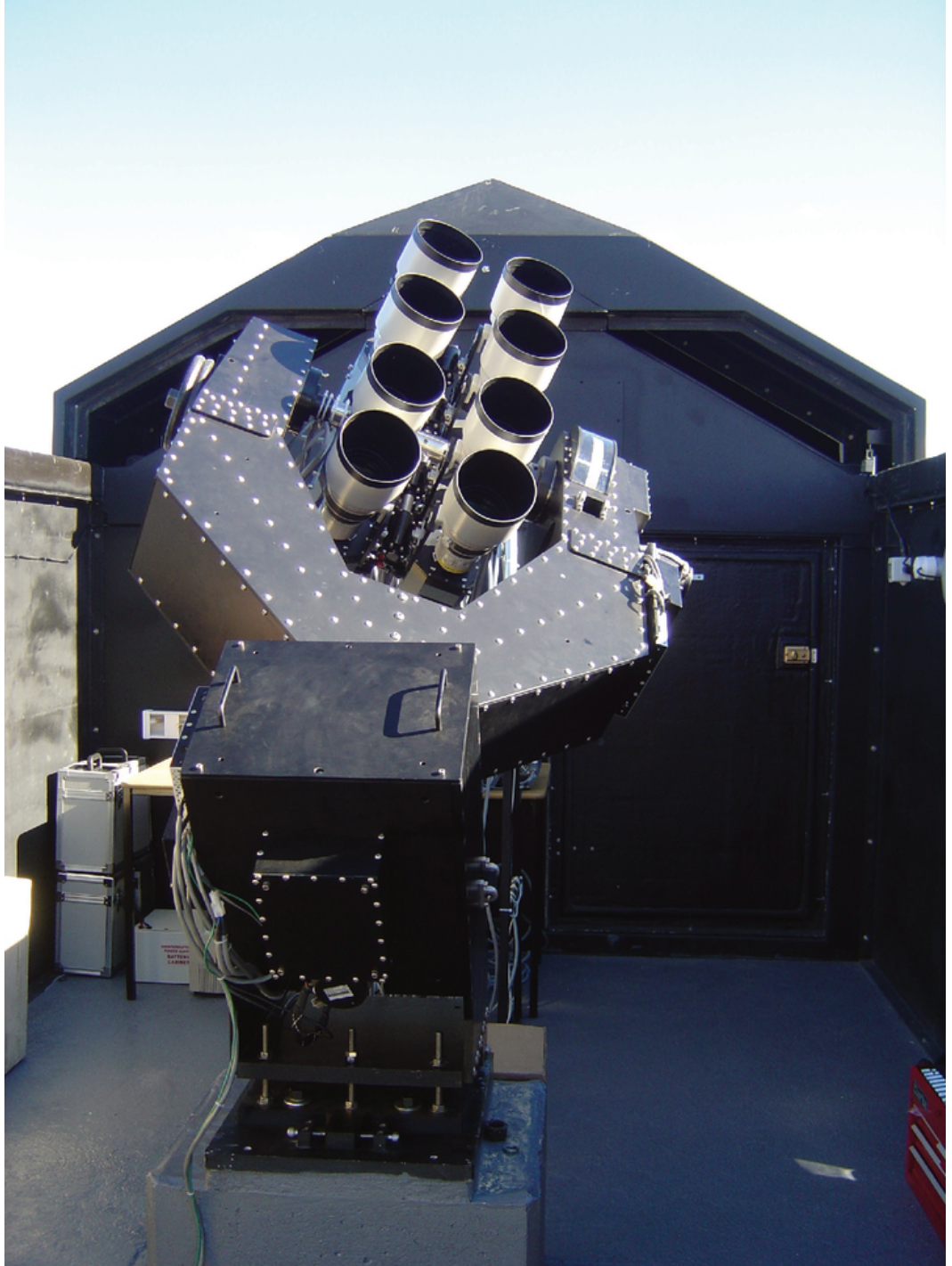


Figure 1.14: *WASP* instrumental setup showing the eight 11cm aperture Canon telescopes attached to their armature. From Pollacco et al. [2006]

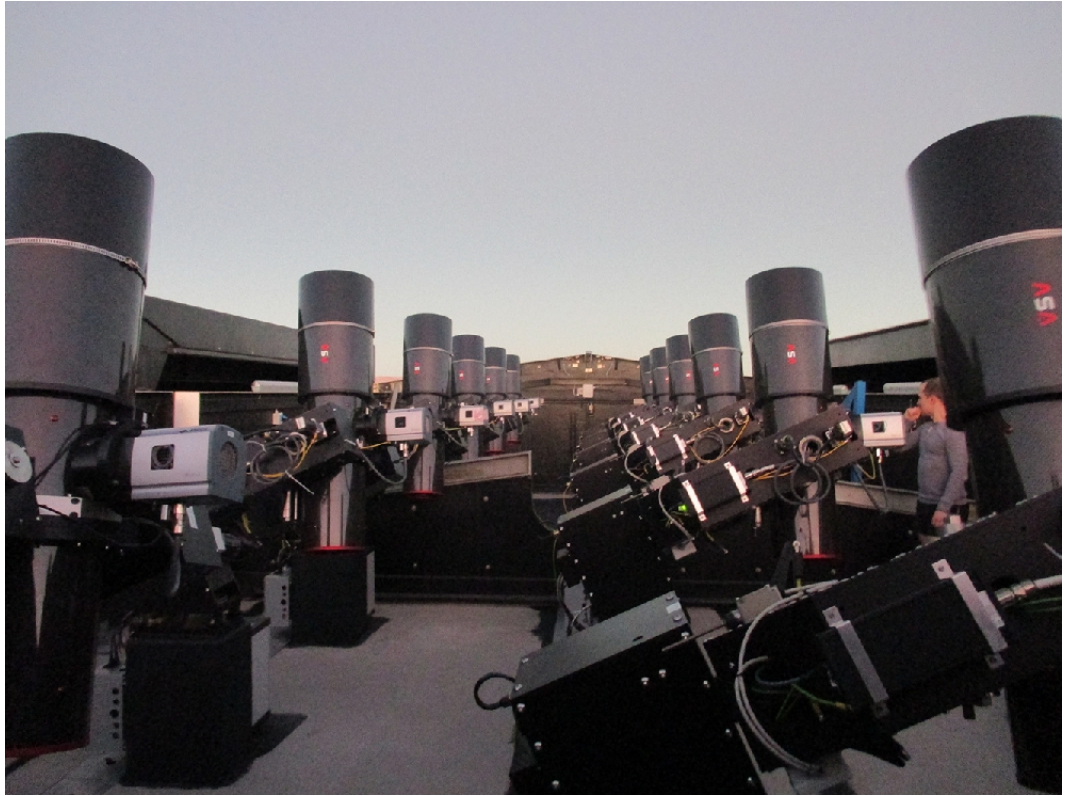


Figure 1.15: The twelve 20 cm *NGTS* telescopes shown on their independent mounts in Paranal, Chile. Taken from Wheatley et al. [2018]. (Astronomer Dr James McCormac for scale).

independently mounted 20cm robotic telescopes in Paranal, Chile. These telescopes can either be pointed at the same target to increase precision or at different targets to maximise sky coverage. For bright stars the precision of *NGTS* is approaching the limit of what can be achieved from the ground due to atmospheric scintillation effects (i.e. twinkling) [O’Brien et al., 2022]. To date, *NGTS* has recovered more than two dozen transiting exoplanets from its own survey and follow-up observations of space based surveys including *TESS* (see Section 1.6) [e.g; Bayliss et al., 2018; Raynard et al., 2018; Günther et al., 2018; West et al., 2019; Vines et al., 2019; Gill et al., 2020]. Another current generation ground based survey of note is the Search for habitable Planets ECliPSing ULtra-cOOl Stars [SPECULOOS; Sebastian et al., 2021] survey, which is specifically searching for Earth or Venus sized planets around late M type dwarf stars.

1.5.2 The *Kepler* space telescope

The *Kepler* space telescope [Borucki et al., 2010], carried out a 3.5 year long stare observation of a relatively small field and was hugely successful in discovering a sample of thousands of transiting exoplanets. Thanks to this large homogeneous sample, it is possible to perform large demographic analyses of exoplanets (see Section 1.3) and estimate the underlying planetary occurrence rate [e.g.; Fressin et al., 2013; Dressing & Charbonneau, 2013, 2015; Hsu et al., 2019; Kunitomo & Matthews, 2020].

By May 2013, two of the reaction wheels aboard the *Kepler* spacecraft had failed, meaning that the telescope could no longer remain pointed at its original field. However, the telescope itself was still perfectly functional and engineers realised that the solar wind could be used to aid the two remaining reaction wheels for pointing. The *Kepler* mission was reworked into the K2 mission [Howell et al., 2014], now pointing at several fields along the ecliptic for ~ 75 days each. Exoplanet discoveries continued to be made from K2 [e.g. Foreman-Mackey et al., 2015; Cloutier et al., 2017] until 2018 when the spacecraft finally ran out of fuel and ceased operation.

Despite the enormous success of *Kepler*, due to the relatively small field of view of *Kepler* most of its target stars are too faint to allow for spectroscopic observations to determine the masses (see Section 1.2.4) and atmospheric compositions (see Section 1.4.3) of their orbiting planets.

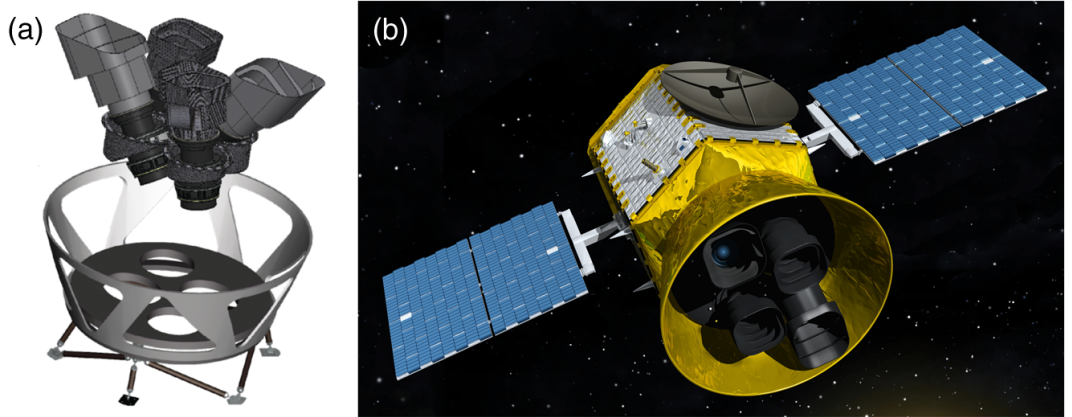


Figure 1.16: (a) Diagram showing the arrangement of the four *TESS* cameras on their mounting platform. (b) Artist's impression of the *TESS* spacecraft. Taken from Ricker et al. [2015].

1.6 The Transiting Exoplanet Survey Satellite (*TESS*)

1.6.1 Overview

The Transiting Exoplanet Survey Satellite [*TESS*; Ricker et al., 2015] was launched in 2018 with the aim to take the next logical step from *Kepler* (see Section 1.5.2) by performing a near all sky survey to discover transiting planets (with a particular focus on planets with radii smaller than Neptune) orbiting nearby stars which are sufficiently bright to allow spectroscopic follow-up observations.

The *TESS* spacecraft orbits the Earth approximately once every 13.7 days, following a highly elliptical path in a 2:1 resonance with The Moon. *TESS* uploads its data at orbital perigee, causing a visible gap in the data every 13.7 days, which can be seen in Figure 1.12. In the Second extended mission and beyond *TESS* will upload data at apogee and perigee, resulting in two smaller data gaps and allowing data to be available faster. Its main payload consists of four onboard cameras each made up of four Charge-Coupled-Devices (CCDs) which are sensitive to optical light with wavelengths between 600 and 1000nm, particularly to longer-wavelength redder light within this band-pass which tends to be produced by smaller cooler stars. Each camera has a square field of view of $24^\circ \times 24^\circ$. These four cameras are stacked vertically to create a combined rectangular field of view of $96^\circ \times 24^\circ$ as shown in Figures 1.16 and 1.17.

Figure 1.17 shows an overview of the observing strategy of *TESS*. The night sky is divided into 26 equally sized sectors, 13 in each ecliptic hemisphere (sectors 1-13 in the south and 14-26 in the north in the primary mission) with *TESS* camera 4

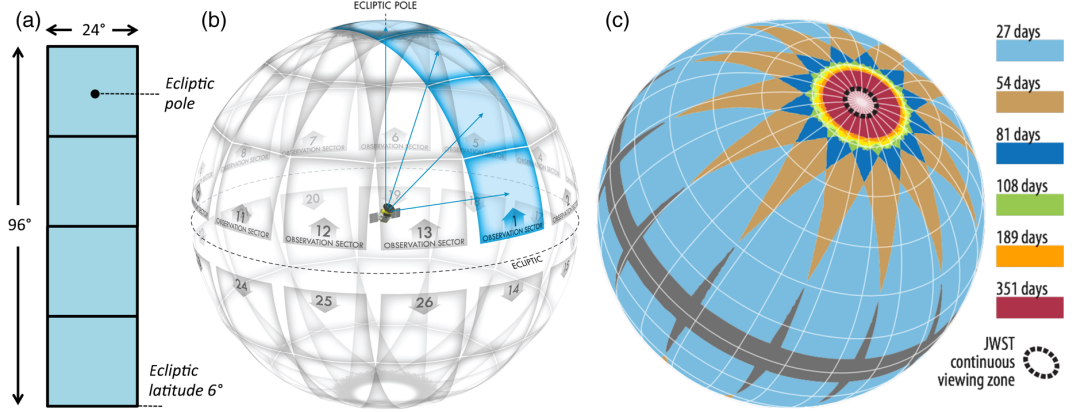


Figure 1.17: Diagrams taken from Ricker et al. [2015]. (a) Shows the field of view of a single *TESS* sector made up of four cameras. (b) Shows the layout of 26 observation sectors. (c) Shows the observation duration of *TESS* as a function of sky coordinates based on the overlap of *TESS* observing sectors.

centered on the ecliptic pole. *TESS* observes each sector for two orbits (i.e. 27.4 days) before rotating and beginning to observe the next sector. *TESS* data is downloaded at the perigee (closest point to Earth) of each of its orbits, causing a ~ 0.5 day gap in observations in the middle of each sector (this can be seen in Figure 1.12). The overlap between sectors, especially near the ecliptic poles, meant that some *TESS* targets are observed in multiple sectors, giving them a longer duration of observations. Some targets near the ecliptic poles are in the Continuous Viewing Zone (CVZ) and are observed in every sector for a full year before *TESS* moves to observe the opposite ecliptic hemisphere.

TESS produces two main data products; high time cadence "postage-stamp" lightcurves of ~ 200000 selected targets produced by the Science Processing Operations Centre [SPOC; Jenkins et al., 2016] and the full frame images [Ricker et al., 2015, FFI;]. Both data sets are freely available from the Mikulski Archive for Space Telescopes (MAST). The SPOC and Quick Look Pipelines [QLP; Huang et al., 2020] also produce freely accessible lightcurves from the FFIs for specific targets from the *TESS* Input Catalogue [TIC; Stassun et al., 2019]. TIC is a compiled catalog of stellar parameters for every optically persistent, stationary object in the sky containing accurate stellar parameters from *Gaia* [Gaia Collaboration et al., 2016, 2018, 2023]. In the Primary mission, postage stamps were taken at a 2 minute time cadence and FFIs at 30 mins. In the second extended mission the cadence of FFIs was increased to 10 minutes. In the second extended mission and beyond *TESS* will take postage stamp observations at 20second cadence and FFIs at 200 seconds.

1.6.2 Pointings

Primary Mission

The pointings of *TESS* sectors for the mission's first year of observations in the Southern ecliptic hemisphere are shown in Figure 1.18a. When *TESS* moved to observe the northern hemisphere in the second year of its primary mission, sectors 14,15,16 and 24,25,26 had to have their pointings shifted north to account for scattered light. The resulting pointings are shown in Figure 1.18b.

First extended mission

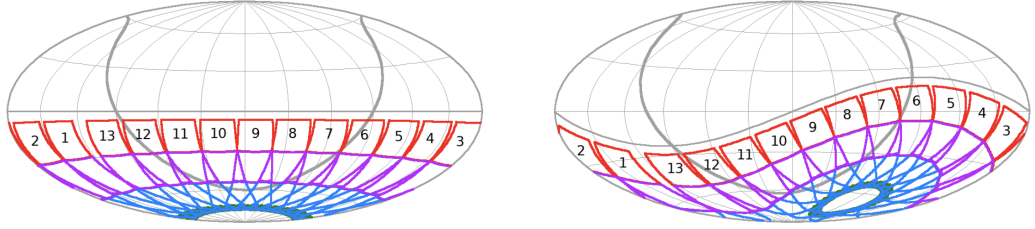
In 2020, *TESS* completed its primary mission and began its first extended mission, reobserving the northern and southern hemisphere (see Figure 1.18c) with sectors 27-39 shifted to cover some gaps in sky coverage from the primary mission. The reobservation of the northern ecliptic hemisphere in Year 4 included 16 sectors (40-55) instead of the usual 13 and lasted around 15 months as the spacecraft rolled on its axis to observe the ecliptic. The first extended mission was completed in 2022.

Second extended mission

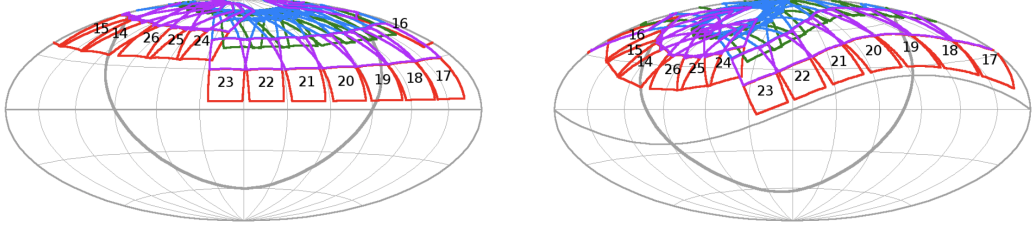
At the time of writing, *TESS* has completed its first extended mission and is currently undergoing its second extended mission. Once again *TESS* will reobserve the northern and southern ecliptic hemispheres and the ecliptic itself. Year 5 has just been completed with a survey of the northern ecliptic hemisphere in sectors 56-60 before reobserving the southern ecliptic hemisphere in sectors 61-69. Year 6 has just begun, following a similar strategy to Year 4 observing the ecliptic plane in sectors 70-72 before reobserving the northern ecliptic hemisphere in sectors 73-83.

Future extended missions

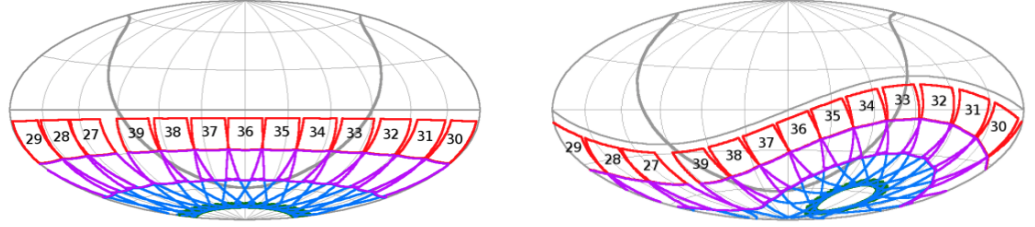
TESS continues to produce high quality data and was launched with at least a decade worth of fuel [Ricker et al., 2015]. As long as the storage space and computational resources are available, additional *TESS* extended missions could continue for years to come. Kunimoto et al. [2022] have performed yield estimations for *TESS* across its primary and extended missions and have found that the mission will continue to yield large numbers of exoplanets into the future.



(a) *TESS* Year 1 sectors shown in ecliptic coordinates (left) and sky coordinates (right)



(b) *TESS* Year 2 sectors shown in ecliptic coordinates (left) and sky coordinates (right)



(c) *TESS* Year 3 sectors shown in ecliptic coordinates (left) and sky coordinates (right)

Figure 1.18: *TESS* sectors for years 1, 2 and 3. Year (top), Year 2 (middle) and Year 3 (bottom). Each set of sectors is shown in ecliptic coordinates (left) and sky coordinates (right), the thinner line across equator is the ecliptic and the thicker line curving down and upwards is the galactic plane. Note the northward shift of sectors 14,15,16 and 24,25,26 of Year 1 to avoid scattered light from the Earth and Moon, resulting in a considerable gap in sky coverage for the northern ecliptic hemisphere. Image credit: NASA.

1.6.3 Discoveries

The first exoplanet detected by *TESS* was π Mensae c [Huang et al., 2018b; Gandolfi et al., 2018], a super-Earth planet (see Section 1.3) on a 6.27 day orbit around π Mensae - a star visible with the naked eye in the constellation of Mensa which was already known from RV observations (see Section 1.2.4) to host a Jupiter sized planet on a highly eccentric > 2000 day orbit [π Mensae b; Jones et al., 2002].

Since this first discovery, *TESS* has gone on to find 5663 candidate exoplanets with 232 currently confirmed from RVs or other follow-up measurements at the time of writing [Source - NASA Exoplanet Archive; Akesson et al., 2013, Accessed; 15-06-2023]. This includes AU Mic b [Plavchan et al., 2020], a short-period Neptune sized planet orbiting the nearby red dwarf star AU microscopis which is also known to host a large debris disk [Kalas et al., 2004]. *TESS* has also yielded exciting discoveries of short period planets of intermediate radii in the so-called Neptunian desert (see Section 1.3.1) [e.g; Hawthorn et al., 2023c; Osborn et al., 2023a; Frame et al., 2023] as well as relatively small super-Earths and mini-Neptunes (see Section 1.3.1) [e.g; Huang et al., 2018b; Gandolfi et al., 2018; Barros et al., 2023; Maciejewski et al., 2023; Hawthorn et al., 2023b,c].

Non-exoplanet science

The all-sky nature of the *TESS* mission makes it useful for other areas of astronomy beyond only exoplanets. *TESS* has proved useful in studies using astroseismology [Bowman, 2020; Aerts, 2021] to probe the interior structures of giant stars [e.g; Handler et al., 2019; Aerts et al., 2019; Bowman et al., 2019; Southworth et al., 2020; Burssens et al., 2020; Daszyńska-Daszkiewicz et al., 2023] as well as observations of young stars [e.g; Armeni et al., 2023; Bouma et al., 2023]. Short duration transient events such as supernovae and Tidal Disruption Events (TDE) have been detected and studied using *TESS* [e.g; Valley et al., 2019; Holoien et al., 2019; Fausnaugh et al., 2021]. Solar System bodies have also been studied with *TESS* [e.g; Rice & Laughlin, 2020; Kiss et al., 2021; Szakáts et al., 2023].

1.7 Monotransits

Transiting exoplanets are generally biased towards shorter periods, shorter period planets have a greater geometric probability of transit (see Section 1.4.1) are more likely to transit more often during a given monitoring period, allowing more confidence in a detection. Planets with longer-periods are more likely to only transit once

in shorter monitoring campaigns such as those employed by K2 (see Section 1.5.2 and *TESS* (see Section 1.6) [Osborn, 2017]. Such events are often referred to as "monotransits". Early examples include HIP 116454 b [Vanderburg et al., 2015] and EPIC 248847494 b [Giles et al., 2018, see Figure 1.19] both of which were recovered from single transit events in K2 (See Section 1.5.2).

Normally, for a planet with multiple observed transits, the observations are confirmed by folding the repeated transits along the period of the orbit to obtain a greater signal-to-noise ratio (SNR) as demonstrated in Section 1.4.2. This is, of course, not possible with only one transit observed. In such cases, follow-up observations are needed to confirm the transit and constrain the parameters of the system. The orbital period can be somewhat constrained by measurement of the width of transit, which is a function of the orbital period (see Equation 1.4) and by measurement of the host star's density which allows dynamical predictions to be made of the orbital period. However, followup observations are ultimately required to truly determine the orbital period. One of the only facilities capable of such follow-up observations is the Next Generation Transit Survey [*NGTS*; Wheatley et al., 2018, see Section 1.5.1].

A good example of this is *NGTS*-11b [Gill et al., 2020] which was the first exoplanet to be found as a monotransit in *TESS* and have its period confirmed with *NGTS*. The first transit of *NGTS*-11b was found in the FFI light curve from sector 3 of the primary *TESS* mission. A second transit was then observed by *NGTS* 390 days later. This allowed the orbital period to be constrained to a series of aliases, each an integer fraction of 390 days. This constraint was then combined with radial velocity measurements from *HARPS* and *FEROS* (see Section 1.2.4) to determine the most likely period of *NGTS* 11b. The most likely period of the planet was found to be 34.46 days.

Studies such as Villanueva et al. [2019]; Cooke et al. [2018, 2019]; Yao et al. [2019] have characterised the ability of *TESS* to discover long-period transiting planets via monotransits and predicted yields. Now, after the completion of the second extended *TESS* mission, a considerable number of these events have been found and later confirmed as planets [e.g; Gill et al., 2020; Ulmer-Moll et al., 2022; Grieves et al., 2022; Brahm et al., 2023].

1.8 Project Objectives

Due to the generally short duration of *TESS* observations (~ 27 days, see Section 1.6), numerous monotransits are expected to be present in the data as pre-

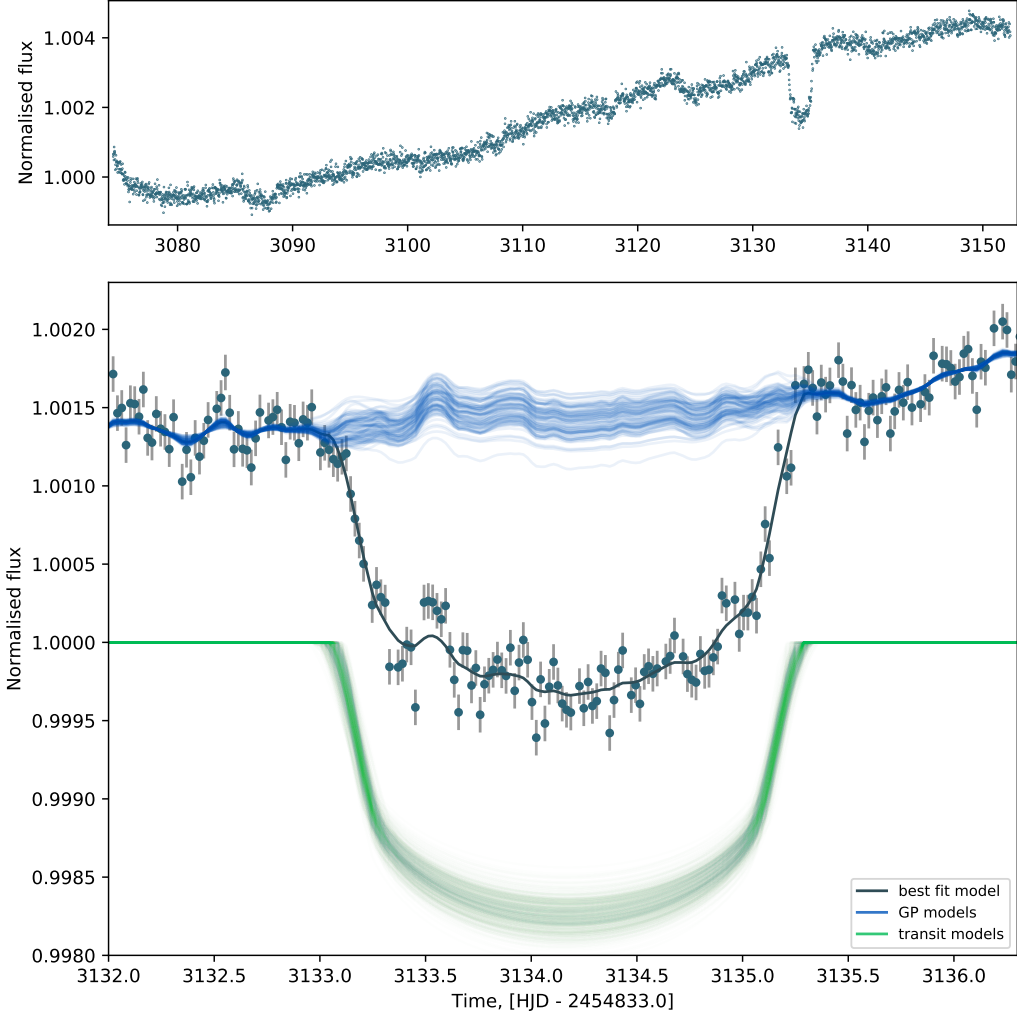


Figure 1.19: Normalised lightcurve of monotransit discovery EPIC 248847494 b from Giles et al. [2018]. The top panel shows the full lightcurve with the 54hr duration single transit shown. The bottom panel shows a zoom in on the transit itself with the best fit model shown in dark blue, Gaussian Process noise models in light blue and transit models in green. The actual data has been offset from the transit model.

dicted by Cooke et al. [2018, 2019]; Villanueva et al. [2019]. These events will allow for discoveries of longer-period transiting exoplanets (see Section 1.3.3) from *TESS* in conjunction with ground based facilities such as *NGTS* (see Section 1.5.1). To guide efforts to recover long-period planets, in Chapter 2 we present a study predicting the yield of exoplanets with a particular focus on long-period planets and monotransits from years 1 and 3 of the *TESS* mission. Our study uses more up-to-date occurrence rates from Kunimoto & Matthews [2020] instead of those from Fressin et al. [2013] as used by Cooke et al. [2018, 2019]; Villanueva et al. [2019]. We also make further use of real *TESS* data in our simulation than these studies.

In Section 2.1 we provide a background and justification for our work. In Section 2.2 we present the Transit Injection and Recovery Application (T*IaRA*) pipeline; made for estimating yields from photometric survey lightcurves. In Section 2.3 we describe how we applied the T*IaRA* pipeline to SPOC data from years 1 and 3 to estimate yields. In Section 2.4, we present the results of our study; both sensitivity maps showing the detection efficiency of *TESS* at detecting long-period planets and our yield predictions from combining those maps with occurrence rates. We discuss possible interpretations and the implications of our results in Section 2.5 as well as caveats to be aware of when interpreting our results. We finally close chapter 2 with a brief summary of our results and discussion of future applications.

The closing Chapter of this thesis, Chapter 3, contains a summary of the key results from Chapter 2 in Section 3.1. We also present a more in-depth discussion of potential future applications of the T*IaRA* pipeline in Section 3.2 and close by discussing improvements to the T*IaRA* pipeline and other methods in Section 3.4.

Chapter 2

Estimating yields of long-period planets from the southern ecliptic of *TESS*

"You know, I'm something of a scientist myself."

Norman Osborn
Spider-man (2002)

The following chapter is reproduced from the manuscript of a scientific paper written by Toby Rodel, Dr Daniel Bayliss, Dr Samuel Gill and Faith Hawthorn and intended to be submitted for publication in the Monthly Notices of the Royal Astronomical Society (MNRAS) in October 2023.

Abstract

We present a study of the detection efficiency for the *TESS* mission, focusing on the yield of longer-period transiting exoplanets ($P > 25$ days). We created the Transit Injection and Recovery Application (T_IaR_A) pipeline to use real *TESS* data with injected transits to create sensitivity maps which we combine with known *Kepler* occurrence rates. This allows us to predict longer-period exoplanet yields, which will help design follow-up photometric and spectroscopic programs, such as the *NGTS* Monotransit Program. For the *TESS* Year 1 and Year 3 SPOC FFI lightcurves, we find 2271^{+241}_{-138} exoplanets predicted to be detected around AFGKM dwarf host stars. Of these 403^{+64}_{-38} will have orbital periods greater than 25 days and 113^{+23}_{-17} will have

orbital periods greater than 100 days. We find 215^{+37}_{-23} exoplanets should be detected from single-transit events or "monotransits". An additional 113^{+22}_{-13} detections should result from "biennial duotransit" events with one transit in Year 1 and a second in Year 3. We also find that K dwarf stars yield the most detections by *TESS* per star observed. We compare our results to the actual TOI discoveries around the stars in our sample and find reasonable agreement for planets with $P < 25$ days and increasing over-prediction compared to TOI discoveries for longer-periods. This may indicate a significant number of long-period planets yet to be discovered from *TESS* data as monotransits or biennial duotransits.

2.1 Introduction

Transiting exoplanets are of exceptional scientific importance as they allow for many parameters of a planetary system to be characterised. Transit detections themselves allow for the orbital period and radius of a planet to be constrained [Winn, 2014]. These measurements of radius can then be combined with spectroscopic radial velocity measurements of the planet's mass (if the planet orbits a sufficiently bright host star) to constrain the planetary density and make inferences about composition and internal structure. For planets transiting bright enough stars to produce high signal to noise spectra it is possible even to undertake atmospheric characterisation via transmission spectroscopy [e.g. Charbonneau et al., 2002; Madhusudhan et al., 2014a; Kreidberg, 2018; Kempton et al., 2018; Madhusudhan, 2019].

Discoveries from transit surveys are biased towards shorter-period planets. Shorter-period planets have a greater geometric probability of transit [Winn, 2014] and transit more frequently within any given monitoring campaign, resulting in an increase in the signal-to-noise ratio (SNR) of the transit signal.

Longer-period planets also allow for unique insights into planet formation and migration mechanisms. At the extremely small orbital separation of planets with $P < 10$ days tidal interactions are expected to dominate dynamical evolution [Valsecchi et al., 2015]. This leads to very reduced eccentricities [Albrecht et al., 2012; Winn, 2014], effectively removing any trace of past dynamical interactions from the planet's present day orbit. Planets with longer-orbital periods have larger orbital separations and as such experience weaker tidal forces, retaining more information on past dynamical interactions. Differences have been identified in distributions of numbers of close orbital companions [Huang et al., 2016] and orbital eccentricity [Dong et al., 2021], between longer-period giant "warm-Jupiter" type planets and shorter-period "hot-Jupiter" giant planets. This indicates that giant planets with

orbital periods longer than 10 days may be experiencing different migration pathways compared with short-period giant planets [Wu & Lithwick, 2011; Petrovich, 2014; Mustill et al., 2017b]. Furthermore, Rossiter-McLaughlin [RM; Rossiter, 1924; McLaughlin, 1924] measurements of orbital obliquity allow further constraining of possible migration mechanisms in the planet’s history [Triaud, 2018]. Already, Rice et al. [2022] have found a trend towards more aligned obliquities in some warm-Jupiters compared to hot-Jupiters although a statistical study on a greater number of targets are needed to confirm this trend.

Additionally, due to the less extreme irradiation from their host stars, longer-period planets are likely to retain more of their original atmospheres compared to shorter-period planets e.g. Hawthorn et al. [2023b,c]; Osborn et al. [2023a]. This makes long-period planets promising targets for atmospheric studies to probe cooler atmospheres that have undergone less photo-evaporation and to gain an accurate understanding of their formation through measurement of their C/O ratios [Öberg et al., 2011; Madhusudhan et al., 2014b].

Long-period planets also offer important targets in the search for exomoons and exorings, which have not yet been detected but are theoretically detectable around giant transiting planets [Barnes & Fortney, 2004; Kipping et al., 2009; Simon et al., 2012; Aizawa et al., 2017]. Exomoons and exorings are predicted to be more stable and thus likelier to exist around longer-period planets with greater orbital separations [Barnes & O’Brien, 2002; Barnes & Fortney, 2004; Cassidy et al., 2009; Dobos et al., 2021; Makarov & Efroimsky, 2023].

Thus to obtain an understanding of a broader population of exoplanets, it is essential to discover longer-period transiting exoplanets.

Since 2018, the Transiting Exoplanet Survey Satellite [*TESS*; Ricker et al., 2015] has been performing an all-sky survey searching for transiting exoplanets around bright host stars. The primary science goal is to find nearby planets amenable to atmospheric characterisation [Ricker et al., 2015; Kempton et al., 2018]. *TESS* observes each $24^\circ \times 96^\circ$ sector of sky for 27 days at a time, although overlap of some regions between sectors mean that the observation baselines for some targets will be >300 days near the Ecliptic poles in the Continuous Viewing Zone [CVZ; Ricker et al., 2015]. However, in the first year of *TESS* 75% of SPOC FFI target stars were only observed in a single sector which means that longer period planets are likely to only be observed as a single transit. Figure 2.1 shows the population of *TESS* planet detections both confirmed and unconfirmed, showing the relative lack of longer-period planets. Although such single-transiting candidates are harder to detect, it is not impossible and the ability of *TESS* to do so has been studied previ-

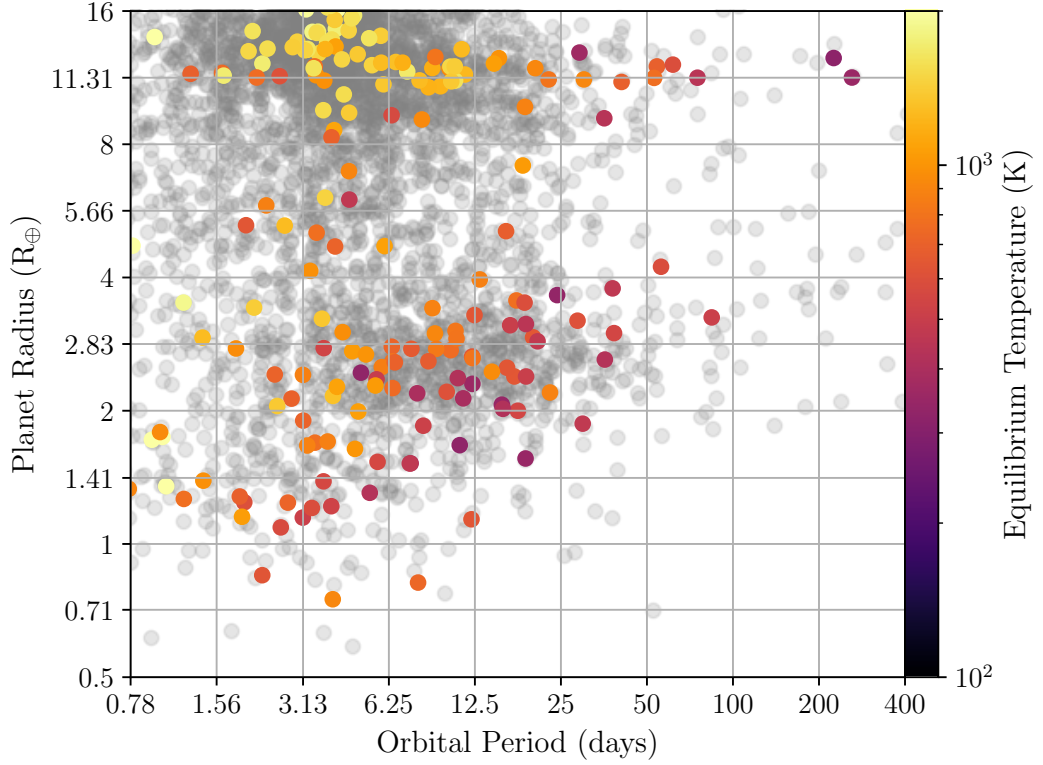


Figure 2.1: The *TESS* planet sample. Full sample of *TESS* objects of interest (TOI) are shown in grey and confirmed TOIs are coloured according to their equilibrium temperature. The full 5663 TOIs consist of the *TESS* project candidate list excluding those flagged as False Positives. The 232 confirmed *TESS* planets include all published and confirmed exoplanets from *TESS* with fully constrained, masses, radii and orbital periods. Both data sets were downloaded from the NASA exoplanet archive [Akeson et al., 2013] on 2023-06-15.

ously in Cooke et al. [2018, 2019]; Villanueva et al. [2019].

Planets discovered from a single transit or "monotransit" do not have constrained periods and require follow-up observations to rule out false positive scenarios and constrain their periods. Such observations can be performed using photometry or spectroscopic radial velocity (RV) measurements.

Photometric observations can be used to detect additional transit events, which will either determine the period uniquely, or provide a discrete set of aliases [e.g; Gill et al., 2020]. This is the primary goal of the Next Generation Transit Survey [NGTS; Wheatley et al., 2018] monotransit working group, which uses the 12-telescope NGTS facility in Paranal, Chile to monitor *TESS* monotransit candidates that display transit events with depths 1000 ppm or greater [Bayliss et al., 2020].

This program has already successfully confirmed "monotransits" from *TESS* data [e.g. Gill et al., 2020; Lendl et al., 2020; Ulmer-Moll et al., 2022; Grieves et al., 2022]. The *TESS* single transit Group has also been following up monotransits using a global network of small telescopes [Dragomir et al., 2023].

For shallower *TESS* monotransits (<1000 ppm) usually associated with smaller planets it is extremely difficult to detect additional transits from the ground. In these cases space facilities such as *CHEOPS* [Benz et al., 2021] can be used to detect further transits, e.g. [Tuson et al., 2023; Osborn et al., 2023b; Ulmer-Moll et al., 2023].

Spectroscopic monitoring of monotransits can also determine the true period of a planet candidate and rule out some eclipsing binary stars which display very large RV variations. Examples discoveries using such spectroscopic campaigns include Dragomir et al. [2019]; Ulmer-Moll et al. [2022]; Eberhardt et al. [2022].

Given the large-effort and hundreds of hours of telescope time involved with such follow-up efforts, it is vital to inform these efforts with up-to-date understanding of the sensitivity of *TESS* to monotransit events and the expected yield of monotransits from the mission.

Previous studies of yields from the *TESS* mission have largely focused on multi-event signals. Prior to the launch of *TESS*, yield estimates were predicted in Sullivan et al. [2015]; Bouma et al. [2017] based on the expected performance of the mission given in Ricker et al. [2015].

Around the time that *TESS* was launched there were several studies that estimated the potential yields from the *TESS* mission, including: Muirhead et al. [2018]; Huang et al. [2018a]; Barclay et al. [2018]; Ballard [2019]. These studies were still largely based on the expected performance of the *TESS* mission as the data from the mission was only just becoming available. More recently, Kunimoto et al. [2022] have revised the yield estimates based on the performance of *TESS* in its primary and first extended mission. All of these studies were largely focused on planet discoveries from two or more transits.

The studies of Cooke et al. [2018] and Villanueva et al. [2019] were specifically focused on the expected yield of monotransits from *TESS*. Due to their publication relatively recently after the launch of *TESS* these studies were also still largely based on the expected performance of *TESS* from Ricker et al. [2015]. Cooke et al. [2019] provided an update to the yields from Cooke et al. [2018] using the performance of the *TESS* primary mission and estimating the yield when *TESS* revisited the southern ecliptic in year 3 during its first extended mission.

In this study, we use the custom-made Transit Injection and Recovery Application (TIRARA) pipeline to create sensitivity maps using real *TESS* Science Processing

Operations Centre [SPOC; Stassun et al., 2019] lightcurves from the southern ecliptic hemisphere (years 1 and 3). We combine these with occurrence rates to estimate a yield of planet discoveries.

We present the full details of the **TIaRA** pipeline in Section 2.2 of this paper. In Section 2.3 we describe the application of the **TIaRA** pipeline to the SPOC FFI lightcurves from Year 1 and Year 3 of the *TESS* mission. In Section 2.4 we present sensitivity maps and estimates of exoplanet yields from our simulation. In Section 2.5 we discuss interpretations of our results and some potential caveats and compare them to both actual *TESS* discoveries and other yield predictions. Finally in Section 2.6 we summarise our work and discuss the potential for applying **TIaRA** to additional *TESS* data sets as well as other transit surveys such as *PLATO* [Rauer et al., 2014].

2.2 The **TIaRA** pipeline

In order to estimate the discovery yield of planets from transit surveys such as *TESS*, we need to simulate as many transiting exoplanet signals as possible in a realistic manner. To do this, we base our simulation on the actual stars that are monitored in the survey. We use the timestamps, measured noise properties, and dilution factors that are recorded for each star. We also use all available stellar properties such as radius (R_\star), temperature (T_{eff}), and mass (M_\star) - which are informed by *Gaia* data releases [Gaia Collaboration et al., 2016, 2018, 2023].

In this Section we introduce the Transit Injection and Recovery Application (**TIaRA**) pipeline, which has been developed to calculate the sensitivity of a given transit survey to discovering transiting planets across a range of orbital periods and planetary radii. When combined with occurrence rates, this provides yield statistics for surveys that can be used to understand and assess the completeness of discoveries from a survey and plan future surveys.

A flowchart detailing the operation of the **TIaRA** pipeline on the *TESS* SPOC FFI lightcurves is shown in Figure 2.2

2.2.1 Input of Lightcurves

TIaRA requires a catalogue of stars observed by a survey and their parameters. Using these target lists we retrieve the relevant lightcurves for processing. We use the timestamps in the lightcurve to calculate a window function for each target star and to determine the number of in-transit datapoints when calculating the signal-to-noise (SNR) for transit events. We also use measurements of noise values and

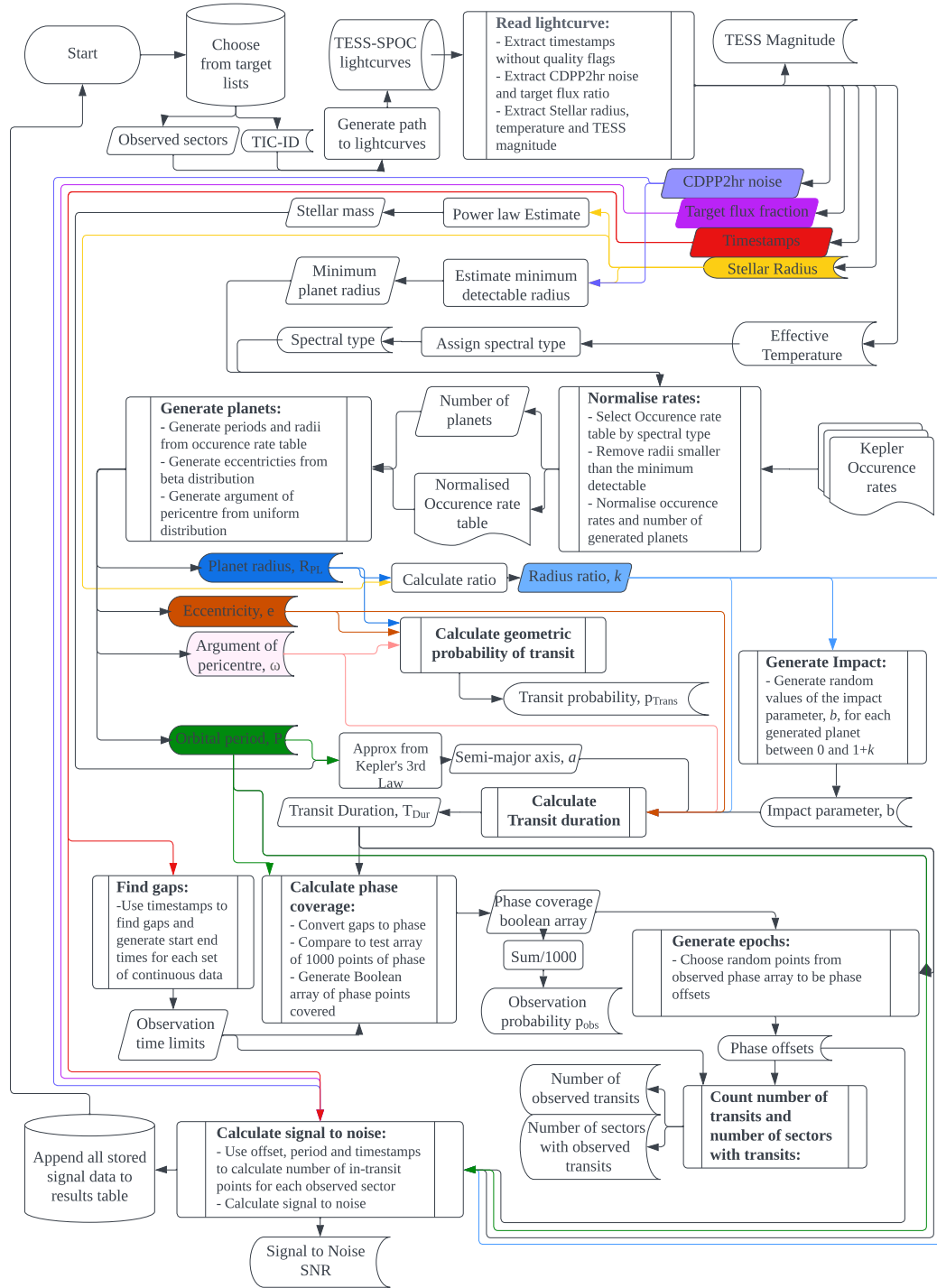


Figure 2.2: Flowchart detailing the operation of the TIARA pipeline on the SPOC FFI lightcurves.

dilution ratios for each lightcurve to calculate SNR for transit events. Using noise values calculated from real lightcurves allows for us to realistically account for a range of astrophysical and instrumental effects in the data. Similarly we use the dilution ratio to account for blending of sources which is a very common problem in wide field photometric transit surveys.

2.2.2 Simulating Transiting Planets

TIARA simulates transiting exoplanets by generating planet parameters and then calculates which timestamps are either occurring in the ingress, egress or fully in-transit portion of the transit event.

Generation of planetary parameters

Thanks largely to the *Kepler* mission [Borucki et al., 2010], we have a good understanding of the occurrence rates of exoplanets, particularly for those with orbital periods less than <100 days [Fressin et al., 2013; Dressing & Charbonneau, 2013, 2015; Hsu et al., 2019; Kunimoto & Matthews, 2020]. For example we know that super-Earth-sized exoplanets are far more common than gas giant planets in short period orbits. We can take advantage of this understanding to optimize TIARA by simulating transiting planets in proportion to the occurrence rate of those planets. The occurrence rates we used are described in Section 2.3.7. **Note that in injecting planets proportionally to occurrence rates is *not* an attempt to simulate the underlying planetary population** but instead is a measure to optimize the simulation. We prioritise injection of more numerous types of planets to avoid wasting simulation time on calculating a precise detection efficiency for rare types of planets for which the yield calculation will almost certainly be zero due to the small numbers in the underlying population. This means that the sensitivity maps we produce are still population agnostic, just with less precise values for rarer types of exoplanets.

We simulate a large number of planets per star (N_{PI}) to obtain a more robust simulation. To choose the orbital period and radius of each of these we first select a period-radius bin using the occurrence rates as a weighted probability for a random draw. The exact period and radius of each planet in the sample was taken from a uniform distribution between the upper and lower limits of the chosen period and radius bins. We use the generated period and the mass of the star to estimate the semi-major axis using Kepler’s third law under the assumption that the mass of the planet is negligible compared to that of the star.

In order to ensure our simulated planets have a realistic eccentricity distribution, we randomly assign each planet an orbital eccentricity from a beta distribution following the prescription set out in Kipping [2013]. We adopt the values of $\alpha = 1.03$ and $\beta = 13.6$ as proposed by Van Eylen & Albrecht [2015].

We randomly assign a periastron angle (ω) in radians, from a uniform distribution over the full π radian range.

For each planet generated, we calculated the geometric probability of transit (p_{tran}) following Winn [2014]:

$$p_{\text{tran}} = \left(\frac{R_{\star} + R_{\text{p}}}{a} \right) \left(\frac{1 + e \sin \omega}{1 - e^2} \right). \quad (2.1)$$

For each simulated transiting planet we randomly generate N_b different impact parameters (b) from a uniform distribution between the values of 0 and $1 + \frac{R_{\text{p}}}{R_{\star}}$.

Simulation of transits

We calculate the total transit duration (T_{14}) including the ingress and egress between the first and fourth points of intersection between the planetary and stellar discs using the following equation from Winn [2014]:

$$T_{14} = \frac{P}{\pi} \arcsin \left[\frac{R_{\star}}{a} \frac{\sqrt{\left(1 + \frac{R_{\text{p}}}{R_{\star}}\right)^2 - b^2}}{\sin i} \right] \frac{\sqrt{1 - e^2}}{1 + e \sin \omega}, \quad (2.2)$$

where i is the inclination of the orbital plane and a is the semi-major axis of the orbit.

In addition, we also calculate the duration of transit between the second and third intersection (T_{23}) using the following equation from Winn [2014]:

$$T_{23} = \frac{P}{\pi} \arcsin \left[\frac{R_{\star}}{a} \frac{\sqrt{\left(1 - \frac{R_{\text{p}}}{R_{\star}}\right)^2 - b^2}}{\sin i} \right] \frac{\sqrt{1 - e^2}}{1 + e \sin \omega}. \quad (2.3)$$

For grazing transits this does not give real solutions, and in such cases we simply set the value of $T_{23} = 0$.

To save computation time, we do not simulate signals with epochs that would result with zero in-transit data points. To accomplish this we convert the timestamps ingested by TIAARA into orbital phase using a chosen reference time (TBJD=0,

BJD=2457000 for *TESS*) and use these phase arrays to determine which portions of the planets orbit are monitored by *TESS*. We then use these observed stretches of phase to generate random epochs in the form of an offset to the chosen reference time, expressed in orbital phase. These observed phase arrays also allow us to calculate the probability that any transit would randomly fall within an observed timespan of *TESS* (p_{obs}). We generate N_{ph} values of this phase offset for each inclination of each planet we simulate resulting in $N_b \times N_{\text{ph}}$ total transit signals per planet.

Using the values of T_{14} and T_{23} calculated from Equations 2.2 & 2.3 and the epoch of each signal, we count the number of points in the timestamps of each lightcurve which are in ingress (N_{ingress}), egress (N_{egress}) or full transit (N_{full}). To obtain a more realistic value of the signal to noise we use a trapezoidal approximation for the shape of transit, and if the signal to noise calculation is likened to the effective area of the transit curve, then the ingress and the egress are triangular while the full transit is rectangular. Thus the effective count of in-transit points for a trapezoidal transit is:

$$N_{\text{trans, eff}} = N_{\text{full}} + 0.5(N_{\text{ingress}} + N_{\text{egress}}). \quad (2.4)$$

2.2.3 Signal-to-Noise Calculation

A full injection and recovery test [e.g; Dressing & Charbonneau, 2015; Hippke & Heller, 2019; Bryant et al., 2023] would require additional computation time to run a detection algorithm [e.g. BLS; Kovács et al., 2002; Collier Cameron et al., 2006] on the data and to initialise a full transit model such as those produced by the **batman** package [Kreidberg, 2015]. We instead calculate detection based purely on the SNR for each signal based on the generated planet properties and lightcurve properties.

The width of the transit is equal to the effective number of in-transit points from Equation 2.4 multiplied by the time cadence of the lightcurve (ΔT) For non-grazing transits where $0 \leq b < 1 - \frac{R_p}{R_\star}$ the depth of transit is simply:

$$\delta = \left(\frac{R_p}{R_\star} \right)^2. \quad (2.5)$$

For grazing transits ($1 - \frac{R_p}{R_\star} \leq b \leq 1 + \frac{R_p}{R_\star}$) we calculate the true anomaly at the time of mid transit in accordance with Maxted [2016]. We then use equation 5.63 from Hilditch [2001] to calculate the corresponding projected orbital separation. We then calculate the depth of transit as the overlap in area between the planetary and stellar disks at this projected separation.

In either case, we then calculate SNR using the equation below:

$$\text{SNR} = \frac{\delta}{1 + C} \frac{\sqrt{N_{\text{trans, eff}} \Delta T}}{\sigma}, \quad (2.6)$$

where the contamination ratio (C) is the proportion of flux from background objects rather than the target itself, ΔT is the time cadence of the lightcurve and σ is the lightcurve noise on the timescale of ΔT .

2.2.4 Detection Probability

To convert from SNR to a recovery rate, we need a function that encapsulates the likelihood that a given signal with a certain SNR will be detected as a transit candidate. Previous studies [Sullivan et al., 2015; Bouma et al., 2017; Huang et al., 2018a; Barclay et al., 2018; Cooke et al., 2018; Villanueva et al., 2019] have used an SNR threshold of $\text{SNR} \geq 7.3$ to determine whether a planet is detectable. This approach is essentially a step function, where the probability of detecting a transit at $\text{SNR} \geq 7.3$ is unity and the probability of detecting a transit at $\text{SNR} < 7.3$ is zero. Kunimoto et al. [2022] used an incomplete gamma function (γ) initially fitted to the *Kepler* pipeline by Christiansen [2017]; Hsu et al. [2019], to characterise the probability of a planet being both detected and passing vetting. The form of this function is:

$$p_{\gamma}(\text{det}) = c_{N_{\text{tr}}} \times \gamma \left(\alpha_{N_{\text{tr}}}, \frac{S/N}{\beta_{N_{\text{tr}}}} \right) \quad (2.7)$$

where $c_{N_{\text{tr}}}$ is the maximum probability of detection a transit signal with N_{tr} observed transits can reach and $\alpha_{N_{\text{tr}}}$, $\beta_{N_{\text{tr}}}$ are coefficients determined from the value of N_{tr} using Table 2.1.

For determining a detection probability, **TIaRA** uses the *Kepler* gamma functions set out in Christiansen [2017] and as adopted by Hsu et al. [2019]. For testing and comparison purposes, **TIaRA** can also used a fixed detection threshold such as $\text{SNR} \geq 7.3$.

In Hsu et al. [2019], there is no detection probability function defined for the case of only one or two transit events in the lightcurve. However calculating the yields for monotransits and duotransits is a key aspect of the **TIaRA** pipeline. Therefore we perform a linear extrapolation of the coefficients fitted by Hsu et al. [2019] to obtain values for $N_{\text{tr}} = 1$ and $N_{\text{tr}} = 2$ resulting in Table 2.1. The incomplete gamma function is represented graphically for each set of coefficients in Figure 2.3.

Table 2.1: Gamma function coefficients.

N_{tr}	$\alpha_{N_{\text{tr}}}$	$\beta_{N_{\text{tr}}}$	$c_{N_{\text{tr}}}$	Source
1	34.3932	0.254262	0.560547	This work
2	33.8908	0.259367	0.629820	This work
3	33.3884	0.264472	0.699093	Hsu et al. [2019]
4	32.8860	0.269577	0.768366	Hsu et al. [2019]
5	31.5196	0.282741	0.833673	Hsu et al. [2019]
6	30.9919	0.286979	0.859865	Hsu et al. [2019]
7-9	30.1906	0.294688	0.875042	Hsu et al. [2019]
10-18	31.6342	0.279425	0.886144	Hsu et al. [2019]
19-36	32.6448	0.268898	0.889724	Hsu et al. [2019]
≥ 37	27.8185	0.32432	0.945075	Hsu et al. [2019]

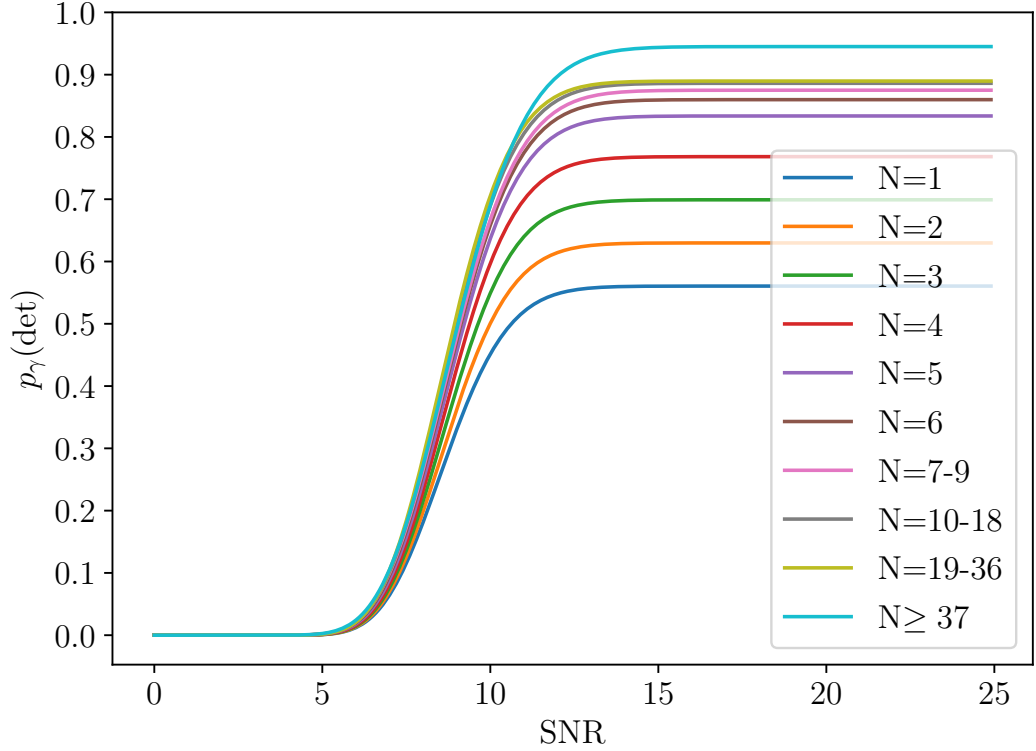


Figure 2.3: The set of incomplete gamma functions used as detection probability functions in the **TTaRA** pipeline. Each function shows the probability a planet will be detected given the signal-to-noise (SNR) of its transit signal in the lightcurve. Each function is for a different number of individual transit events in the lightcurve. The monotransits and duotransits are represented by the blue $N=1$ and orange $N=2$ functions respectively.

2.2.5 Minimum detectable radius cutoff

Since we inject planets proportionally to their real occurrence rates, we will simulate many more smaller radius planets than larger planets due to their relative occurrence rates. However many of the smaller planets would produce transits with extremely low SNR, which may be far below the level of detectability in a given survey. Therefore to conserve computational resources and increase the efficiency of the simulation we implement a radius cutoff to the occurrence rates based on the precision of the given survey. To do this we estimate the minimum detectable radius from a single transit. To calculate the minimum detectable radius we assume a favourable set of transit parameters which consist of $e = 0$, $b = 0$, and T_{dur} set to a "long" transit duration - defined to be the duration of a $P=1000$ days transiting exoplanet of negligible radius around the given host star. Since SNR increases with transit duration, this long duration - beyond what we expect to realistically transit, was chosen so that small-radius planets which could be detected from a long enough transit were not removed from the simulation.

We choose a SNR threshold of 4 to determine the minimum detectable radius as this correlates with a very low probability of detection: $< 10^{-5}$ (see Section 2.2.4). For planets with radii below the cutoff, we simply assign a probability of detection equal to 0.

2.3 *TESS* simulations

2.3.1 *TESS* SPOC FFI lightcurves

In this study we apply *TTaRA* to the Year 1 and Year 3 Full Frame Image [FFI; Ricker et al., 2015] lightcurves from the *TESS* Science Processing Operations Center [SPOC; Jenkins et al., 2016]. The SPOC FFI lightcurve sample is a high quality, homogeneous and readily available dataset representing *TESS* targets which are most amenable to exoplanet detection and thus is appropriate for our purposes [Caldwell et al., 2020]. Additionally the *NGTS* monotransit working group uses the SPOC FFI lightcurves in their search for *TESS* monotransits [e.g; Gill et al., 2020] which allows for easy comparison of our results. We compiled the SPOC FFI target lists per *TESS* sector from MAST available at <https://archive.stsci.edu/hlsp/tess-spoc> into a single list containing the *TESS* Input Catalogue [TICv8; Stassun et al., 2019] numbers of all the SPOC FFI target stars and the *TESS* sectors they were observed in. We also removed all stars with radii $< 0.1R_{\odot}$ and $> 4R_{\odot}$ from the sample. This results in a sample of 1323228 stars across Year 1 and Year 3. For every star in

this list, we obtained the relevant lightcurve FITS files via the MAST portal at <https://archive.stsci.edu/>.

2.3.2 Stellar parameters

We extracted the stellar radius (R_{\star}), *TESS* magnitude (T_{mag}), and effective temperature (T_{eff}) directly from the FITS file headers: These stellar parameters are themselves sourced from the TICv8 [see Stassun et al., 2019].

To calculate a semi-major axis for our injected planets, we require a stellar mass (M_{\star}). Due to the relatively weak dependence of the semi-major axis on stellar mass we assume stellar mass can be estimated using the following power law:

$$M_{\star} = R_{\star}^{1.25}, \quad (2.8)$$

where M_{\star} and R_{\star} are both in solar units. This equation is suitable for the bulk of the main-sequence dwarf stars in the SPOC FFI sample. We assign a spectral type to each star based on T_{eff} using definitions from Pecaut & Mamajek [2013]. Stars with T_{eff} hotter than the maximum cutoff for A type stars (10050 K) were marked as spectral type OB.

2.3.3 Window functions

In order to use the real window function for each star in the SPOC FFI list, we determine blocks of continuous *TESS* observations for each target using the timestamps from the FITS file TIME header for each *TESS* sector. We only consider good quality data where the data quality flag (**QUALITY**) = 0. We use the first and last timestamps of each Sector to define the block of continuous data for each Sector. To identify gaps within Sectors, we search for instances where the difference between two consecutive timestamps is greater than 0.5 days. Most of these gaps are the mid-Sector gaps, which occur during the perigee of the 13.7 day *TESS* orbit when data is downloaded to ground-stations [Ricker et al., 2015]. Other data gaps are caused by technical issues with the specific *TESS* camera, the entire *TESS* spacecraft, or the variety of reasons that give rise to non-zero data quality flags (e.g. stray light, cosmic rays, spacecraft momentum dumps and pointing issues).

To illustrate these data gaps, we plot the lightcurve of a typical SPOC FFI target (TIC-261236954) in Figure 2.4. TIC-261236954 is in the *TESS* CVZ, so can be used to illustrate gaps over the duration of Year 1 of the *TESS* mission. For this star the blocks of continuous photometry account for 79.3% of the total Year 1 duration, while the gaps make up 20.78% of that year.

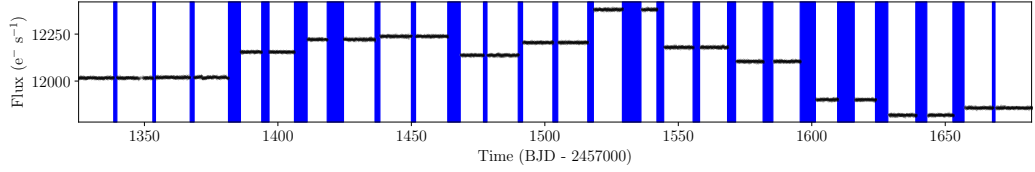


Figure 2.4: An example SPOC FFI lightcurve from a star (TIC-261236954) in the CVZ of *TESS* in Year 1 of the mission, illustrating gaps in the data. The blue shaded regions show data gaps longer than 0.5 days. In this example we find that over the course of one year 79.3% of time is photometrically monitored, while the gaps account for 20.7% of the year.

In order to demonstrate the effect of these gaps in the *TESS* window functions, we calculate the fraction of orbital phase covered by *TESS* observations as a function of the orbital period of a simulated planet for two scenarios: (1) an idealised 27 day window function, and (2) the window function of TIC-261236954 (the lightcurve for which is set out in Fig 2.4). This allows us to compare the effect of gaps for up to 13 consecutive Sectors. The results are set out in Figure 2.5, and show the significant difference between the idealised 27 day Sectors and the real TIC-261236954 lightcurve window function. This highlights the need to account for the gaps in the *TESS* data for each star as we do in the *TIARA* pipeline.

2.3.4 Signal to Noise

To calculate the SNR (Equation 2.6) for each simulated transiting planet, we take the noise of the lightcurve (σ) to be the Combined Differential Photometric Precision [CDPP; Christiansen et al., 2012] 2hr noise as produced by the SPOC FFI pipeline and recorded in the *FITS* headers as `CDPP2_0`. This provides us with a readily available pre-calculated noise metric, which saves computation time. Similarly we take the source-to-background brightness ratio ($C + 1$) from the SPOC FFI pipeline recorded in the *FITS* headers as `CROWDSAP`. The time cadence (ΔT) has changed over the course of the *TESS* mission. For Year 1 the time cadence was 30 mins, while for Year 3 the time cadence was 10 mins.

2.3.5 Probability of detection

We assume that the detection and vetting of transiting exoplanet signals in *TESS* is similar to that of the *Kepler* mission, and we therefore use the modified version of the *Kepler* gamma function (Section 2.2.4) to define our probability of detection for each simulated transiting planet. For comparative purposes, we also record de-

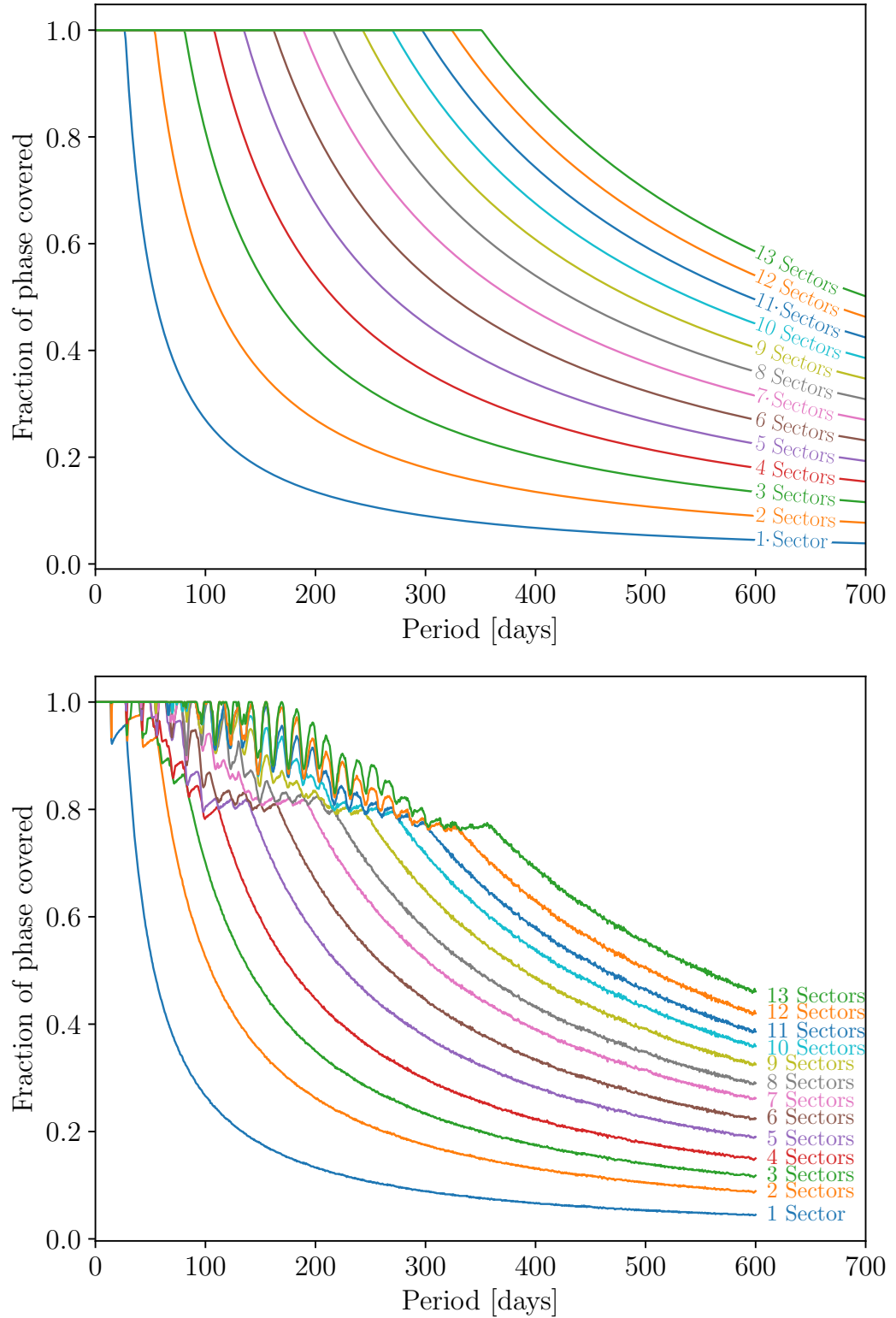


Figure 2.5: Completeness of phase coverage as a function of planetary orbital period. *Top:* Idealised 27 day coverage (no gaps) for durations ranging from 1 to 13 consecutive sectors. *Bottom:* The real phase coverage function for an example SPOC FFI target (TIC-261236954) in the *TESS* CVZ.

tections via two threshold SNR criteria: at $\text{SNR} \geq 7.3$ (to match some previous yield studies) and $\text{SNR} \geq 20$ (to match monotransit searches that typically require such a high SNR for robust detections).

2.3.6 Creating sensitivity maps

For each transit signal that we generate, we convert the SNR into detection probability as described in Section 2.3.5. Each of these probabilities is then multiplied by the probability of observation for each signal calculated from its window function (see Section 2.3.3) to give a probability of observation and detection. These values are again multiplied by the geometric probability of transit for each signal to give a probability of transit, observation and detection by *TESS* for each signal. We take the binned averages for all signals using the same period and radius bins as Kunitomo & Matthews [2020].

We treat each of our detection probabilities as a Poisson statistic such that the error in each is equal to its value divided by the square root of the total count of signals in that bin.

2.3.7 Occurrence Rates

In order to convert our sensitivity maps to yield estimates for the Year 1 and Year 3 *TESS* SPOC FFI sample, we need to know the occurrence rates for the underlying population of planets orbiting each type of star in the sample. For F,G and K dwarf stars we use the occurrence rates calculated in Kunitomo & Matthews [2020]. For A type stars we do not have robust occurrence rates, so we use the same grid as for F type stars.

Kunitomo & Matthews [2020] did not calculate occurrence rates for M dwarfs, so for consistency and ease of comparison between our results we rebin the M dwarf occurrence rate grid from Dressing & Charbonneau [2015] to use the same bins as the grids used in Kunitomo & Matthews [2020]. To do this we use a bivariate spline approximation over a rectangular mesh using the `RectBivariateSpline` interpolator from the `python` module; `scipy.interpolate` [Virtanen et al., 2020]. We take the midpoints of each period and radius bin from the Dressing & Charbonneau [2015] grid and use these for the coordinates of each grid value. We then used the median value, lower bound, and upper bound of each grid cell with these coordinates to create three separate interpolators for each value. We then feed the midpoints of all the Kunitomo & Matthews [2020] bins with $R_p \leq 4R_\oplus$ and an orbital period ≤ 200 days into these to obtain the values for the new grid. For the 200-400 day

period bin we assume the values were identical to the 100-200 day bin. For all bins above $4R_{\oplus}$ we use the values for K dwarf stars but reduced by a factor of 0.5 to account for the generally lower occurrence rates of giant planets around M dwarfs [Sabotta et al., 2021; Bryant et al., 2023].

To account for the fact that some bins in the grid from Dressing & Charbonneau [2015] are unconstrained and contain only an upper bound on the occurrence rate we manually set the equivalent grid cells in our new grid to be unconstrained as well. For all such grid cells, we set the median and lower bound values to zero and the upper bound value to the interpolated median value added to the interpolated upper bound value. We consider the new grid cells between 0.78-1.56 days and $2-4R_{\oplus}$, 6.25-25 days and $1-1.41 R_{\oplus}$, 50-200 days and $0.5-1R_{\oplus}$ and $2.83-4R_{\oplus}$, to be equivalent to the old grid cells between 0.5-1.7 days and $2-4R_{\oplus}$, 5.5-18.2 days and $1.0-1.5 R_{\oplus}$, 60.3-200 days and $0.5-1R_{\oplus}$ and $3.5-4R_{\oplus}$ respectively for the purposes of considering them unconstrained. Furthermore we also consider all the grid cells between 200-400 days and $<4R_{\oplus}$ to be unconstrained as these are extrapolated and not interpolated from the measured *Kepler* rates by Dressing & Charbonneau [2015] and such planets are shown to be very rarely detected by *TESS* if at all [NASA Exoplanet Archive; Akeson et al., 2013].

Our resulting M-dwarf occurrence rate grid is set out in Figure 2.6.

Use as input priority metrics

As set out in Section 2.2.2 we also use occurrence rate grids as a weighted distribution to select periods and radii for planets we inject into the simulation. This requires us to set a median value for unconstrained grid cells that possess only an upper bound. For the A, F, G and K dwarf grids we perform a linear extrapolation of each grid row and column and then take the mean of these as the input grid. For the M dwarf grid we simply take the upper bound of unconstrained grid cells as the median value.

2.3.8 Yield Estimates

To calculate our final yield estimates we multiply the occurrence rates by the detection efficiencies for each spectral type, and then multiply those rates and their uncertainties by the number of each type of star in the Year 1 and Year 3 SPOC FFI sample. This gives us a grid of expected yields for each period-radius bin with uncertainties combined from those of the detection sensitivities and occurrence rates. The error in occurrence rate is considerably larger and so dominated the overall uncertainty in predicted yield.

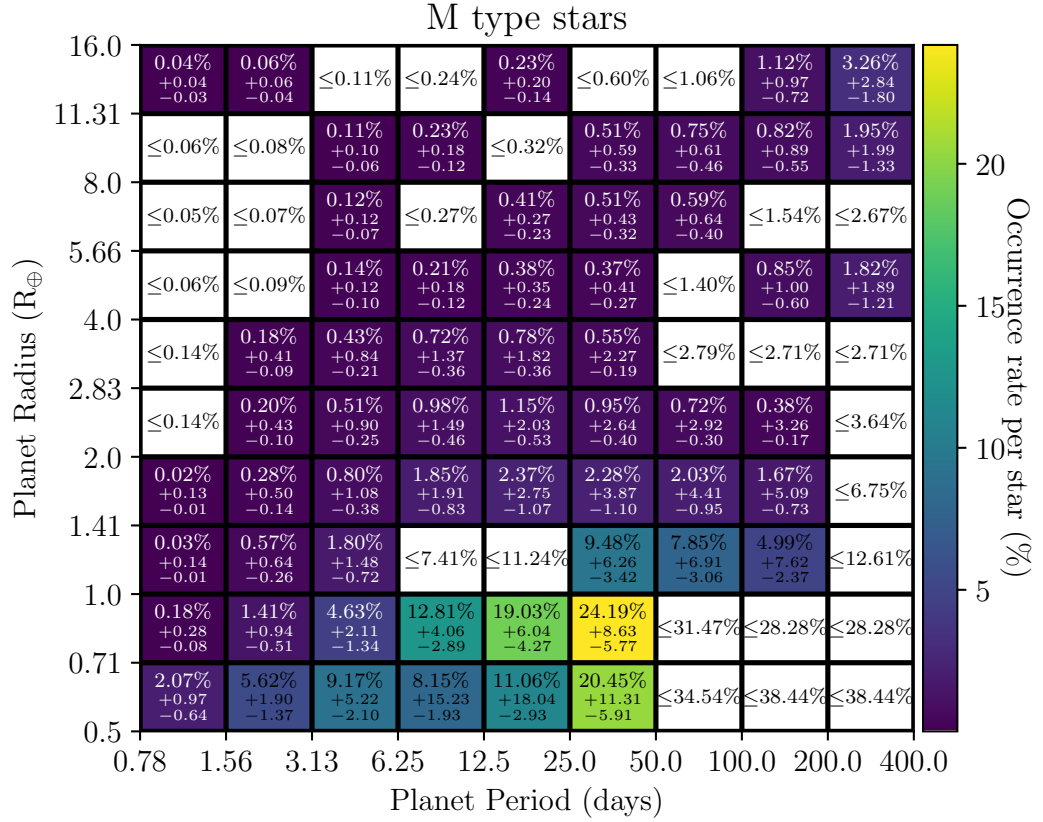


Figure 2.6: Occurrence rates of planets around M dwarfs. Values for $R < 4R_{\oplus}$ taken from Dressing & Charbonneau [2015], rebinned to our standardised grid. Values for $R > 4R_{\oplus}$ from the a scaled K dwarf occurrence rate from Kunimoto & Matthews [2020].

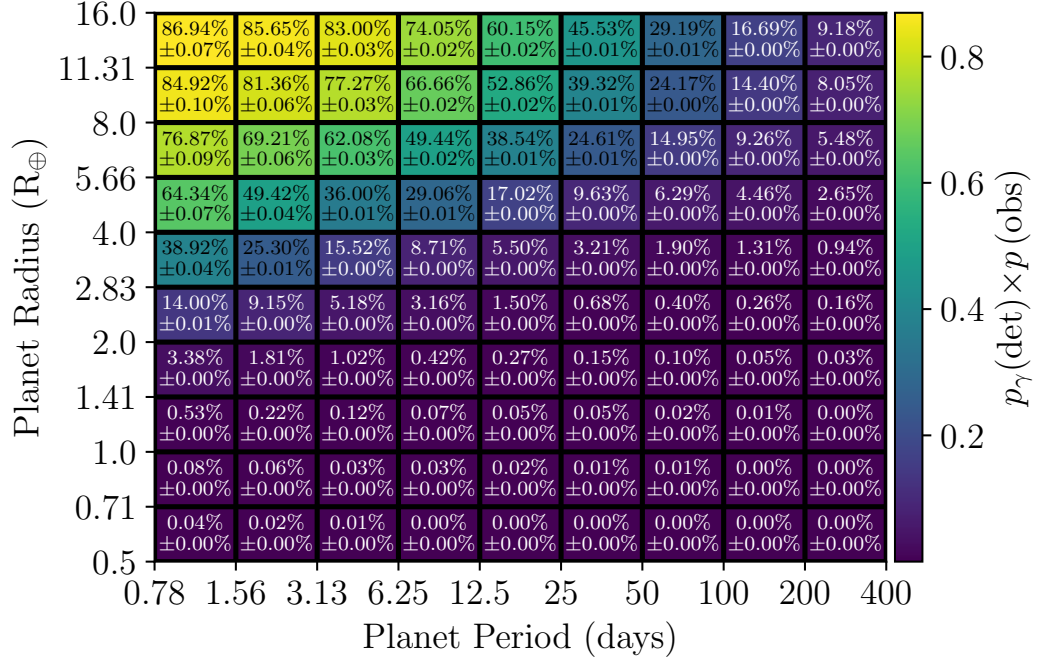


Figure 2.7: Sensitivity map showing the probability of a transiting planet in each period/radius bin being observed and detected around an AFGKM dwarf star in the *TESS* Year 1 and Year 3 SPOC FFI lightcurves.

2.4 Results

2.4.1 *TESS* Sensitivity

The *TTaRA* pipeline creates binned sensitivity maps on the same grid as the occurrence rates from Kunimoto & Matthews [2020]. These show the probability that a transiting exoplanet of a given radius and orbital period is observed and detected by *TESS* in the Year 1 and Year 3 SPOC FFI lightcurves. We compute separate sensitivity maps for each of A,F,G,K, and M dwarfs, and these are set out in Appendix 2.7.1. We also plot the average sensitivity for AFGKM dwarfs in the SPOC FFI sample in Figure 2.7. The uncertainties in sensitivity are very small, this is largely on account of the large numbers of signals we inject in the simulation, which allows for such precise calculation.

Naturally, there is a trend of higher sensitivity towards larger radii planets as these planets produce deeper transits and thus a higher SNR signal. We find that *TESS* should detect over 80% of very short period ($P < 6.25$ day), transiting giant planets ($R > 8R_{\oplus}$). This probability drops below 50% for small transiting planets ($R < 4R_{\oplus}$), and is below 1% for Earth-radii transiting planets.

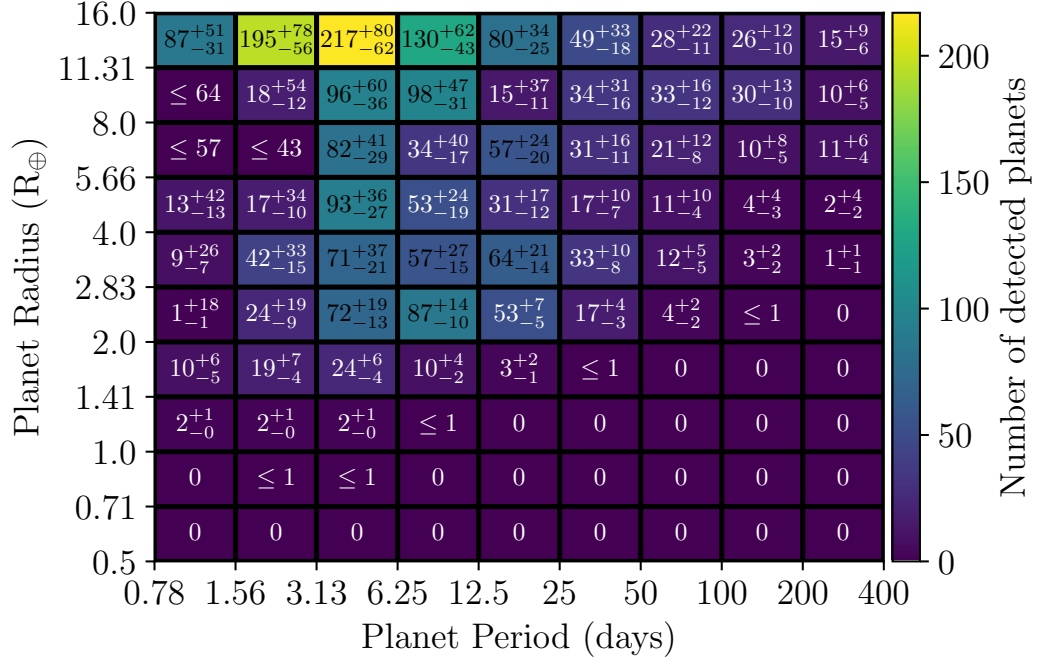


Figure 2.8: Predicted exoplanet yield from Year 1 and 3 SPOC FFI lightcurves of AFGKM type stars. Note that cells where the median value is 1 have been displayed as ≤ 1 to account for the inherent uncertainty in a predicted yield of 1.

Additionally, we are more sensitive to shorter period planets due to the greater number of observed transits in any given monitoring duration. This both produces a higher SNR value when these transits are summed and allows for greater confidence in the detection as accounted for by the gamma function we use to calculate probability of detection (see Section 2.3.5). For giant planets ($R > 8R_{\oplus}$), we move from approximately 80% completeness for short periods ($P < 6.25$ day) down to less than 10% completeness for periods between 200 and 400 days.

As the *TESS* mission continues, these sensitivity maps will evolve as a function of the window function for each star, and the sensitivity will improve over the entire grid. *TTaRA* will be able to re-calculate these sensitivity maps using the timestamps from *TESS* lightcurves as the extended *TESS* mission continues to gather data. For the southern ecliptic hemisphere, this will be the update provided by the Year 5 lightcurves (Sectors 61-69). It is also possible to simulate timestamps for future sectors based on our knowledge of previous sectors with some assumptions needed for distribution of the future data gaps and FFI cadence.

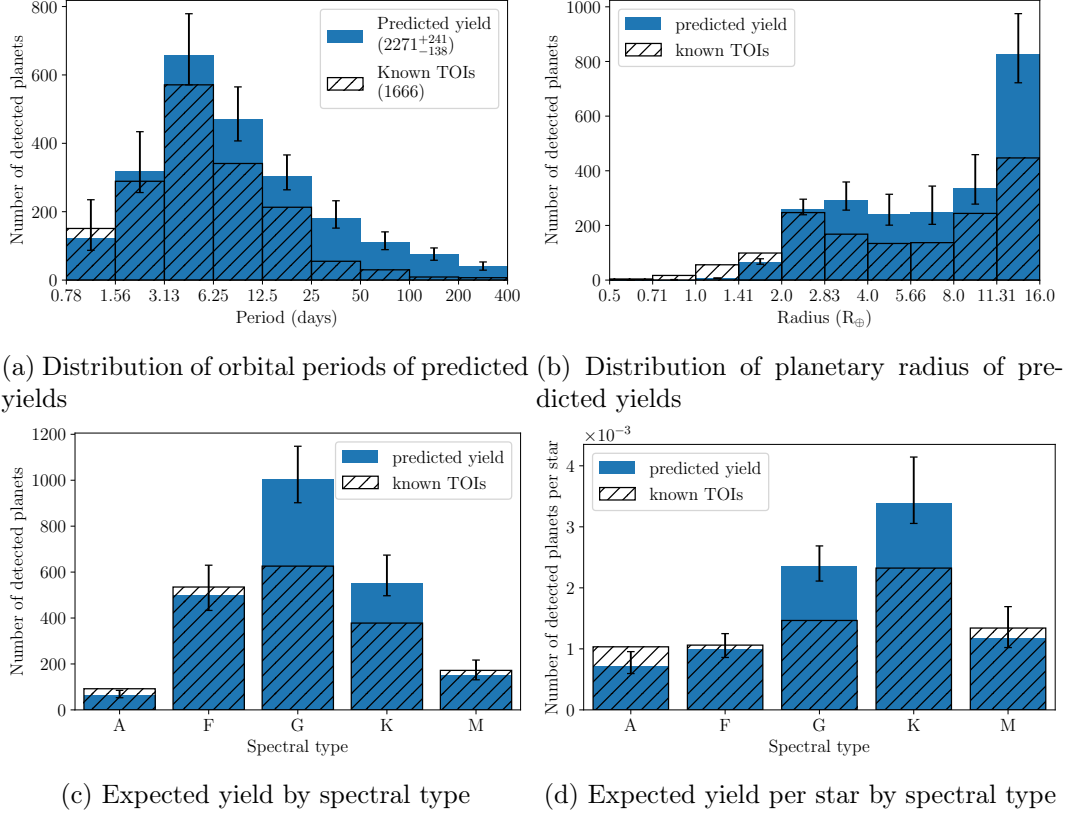


Figure 2.9: Predicted *TtARA* transiting exoplanet yields from the *TESS* Year 1 and Year 3 SPOC FFI lightcurves (solid blue bars). Also displayed are actual *TESS* discoveries (transparent black outlined bars) calculated using TOI catalogue downloaded from the NASA exoplanet archive [Akeson et al., 2013] on 2023-06-15 (excluding flagged false positives) and matched to TIC IDs of southern ecliptic SPOC FFI sample.

2.4.2 Predicted Yield

We present the TIAra predicted yield of transiting exoplanet discoveries from *TESS* Year 1 and Year 3 SPOC FFI lightcurves in Figure 2.8. This grid is the summation of all spectral types, however we also present the yields broken down by spectral type in Appendix 2.7.2.

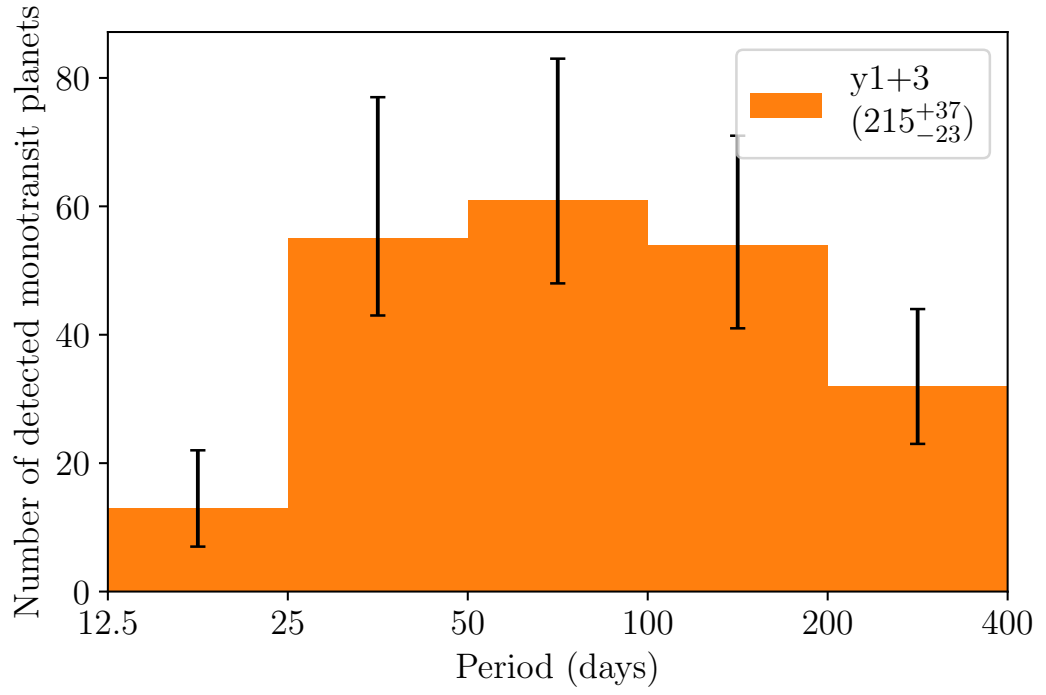
Overall we predict a yield of 2271^{+241}_{-138} exoplanets detected around AFGKM dwarf host stars. We set out the yield distributions of orbital period, planet radius, and host spectral type in Figure 2.9. We find the discoveries should peak at orbital periods between 3.13 and 6.25 days. However there are a significant number of longer period planets in our predicted yield, with 403^{+64}_{-38} planets with orbital periods greater than 25 days and 113^{+23}_{-17} will have orbital periods greater than 100 days. Interestingly the distribution of planet radii is quite flat, with the exception of giant planets ($R > 11.31R_{\oplus}$), which are twice as numerous as other radius bins. Most discoveries are predicted to be around G dwarf stars, although K dwarfs provide the most number of discoveries per star monitored.

To compare our predicted yield to the actual discoveries to date, we cross-match the TOI catalogue with the SPOC FFI target lists for Year 1 and 3 to find transiting exoplanet discoveries from our sample. The distributions of these TOIs and our predicted yields are shown in Figure 2.9.

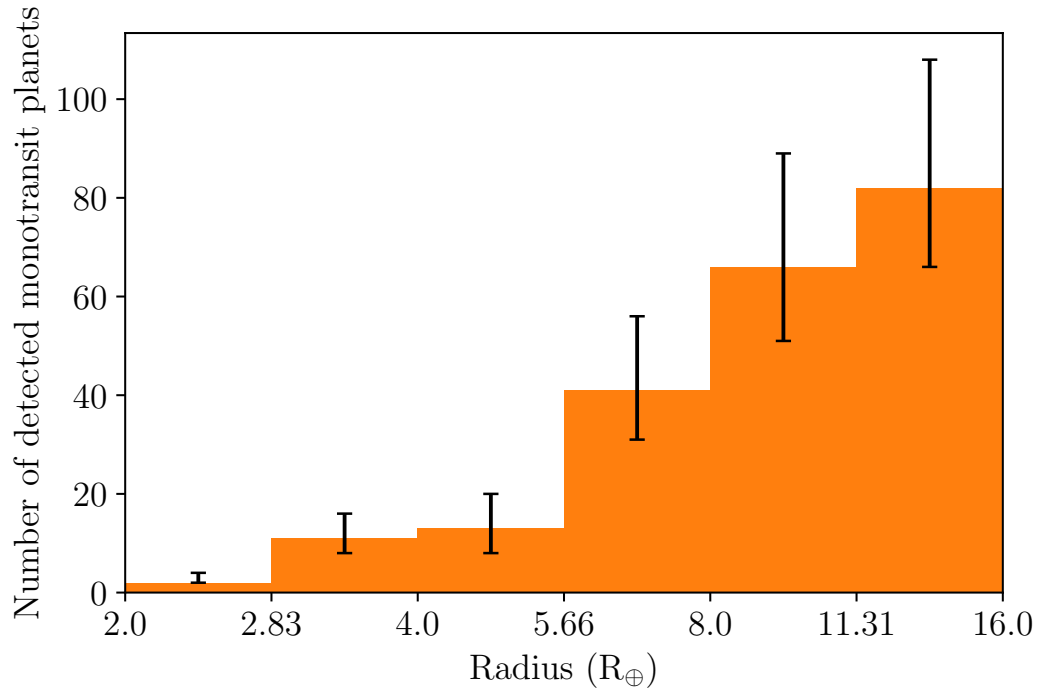
2.4.3 Monotransits

We predict that 215^{+37}_{-23} of the transiting planet discoveries will only have one transit event in the *TESS* Year 1 or Year 3 data - i.e. are "monotransits". This makes up a relatively small fraction (9%) of the total predicted yield, but is a significant fraction of the long-period detections. 202^{+36}_{-22} (50%) of the planets with $P > 25$ days are monotransits, while 86^{+20}_{-14} (76%) of the planets with $P > 100$ days are monotransits. Figure 2.10 shows the the distributions of orbital period and planetary radius for the predicted monotransit yield. As expected there are very few monotransits with orbital periods less than the sector length of *TESS* (27 days). However beyond that the distribution of orbital period is remarkably flat out to our final bin of 400 days. The distribution of planetary radii for the monotransits are much more heavily skewed towards larger radii planets than typical multi-transit detections. 73% of all detections are for planets with $R_p > 4R_{\oplus}$, while this fraction is 94% of just the monotransit detections.

In addition to the monotransit yield for Years 1 and 3 together, we also estimated the yield for Year 1 alone in order to investigate the effect of reobserving



(a) Period distribution of predicted montransit detections



(b) Radius distribution of predicted montransit detections

Figure 2.10: Predicted yields of montransits, shown as binned distributions in orbital period (a) and radius (b).

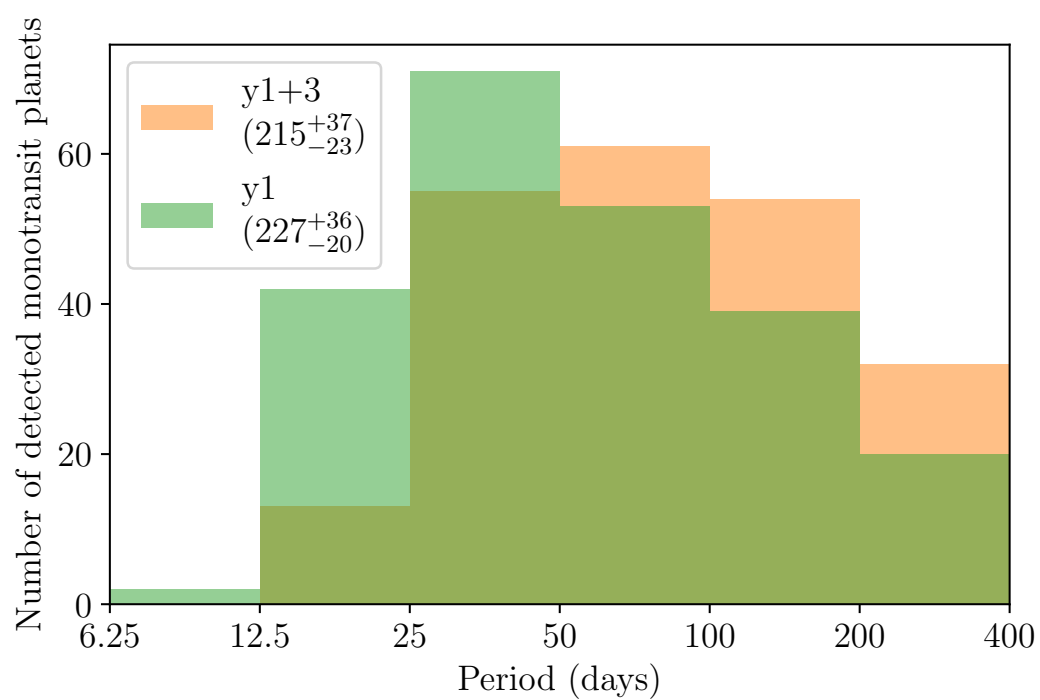


Figure 2.11: Comparison of the distribution in period of the yields of monoplanets from Year 1 alone (green) compared to Year 1 and Year 3 combined (orange).

the field on the monotransit yield. The results are shown in Figure 2.11. We find that the number of monotransits in Year 1 alone is 227^{+36}_{-20} , compared to the Year 1 and 3 combined yield of 215^{+37}_{-23} . Assuming that all of the Year 1 monotransits that have an additional Year 3 transit observed become duotransits (see Section 2.4.4), then this leaves 114^{+42}_{-24} detected monotransits observed in Year 1 and not Year 3 and 101^{+55}_{-33} observed in Year 3 and not Year 1. The distribution of orbital periods changes to favour longer periods with 40% of Year 1 and Year 3 monotransits having $P > 100$ days compared to 26% of Year 1 only monotransits. The distribution of monotransit detections in period also becomes significantly flatter at longer-periods when Year 3 is added to Year 1.

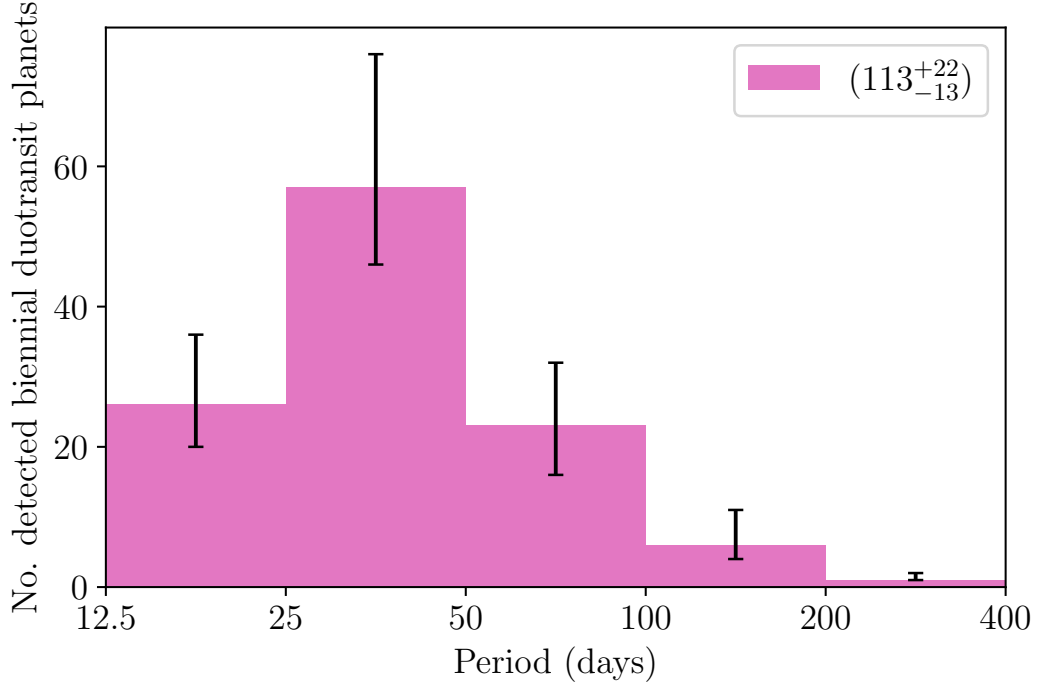
2.4.4 Duotransits

As *TESS* reobserved the southern ecliptic hemisphere in Year 3 of the mission, many Year 1 monotransit signals will have an additional transit observed in Year 3, and become "biennial duotransits". We define these duotransits as "biennial" to distinguish them from other duotransits in which the two transit events happen in the same year of *TESS* data. In Year 1, duotransit signals are caused mostly by planets in a narrow period range such that they transit twice within a single *TESS* sector. With Year 3 added most duotransits are instead caused by longer-period systems with two observed transits separated by a year or more (one in the primary mission and one in the first extended mission). We predict a total of 170^{+29}_{-18} duotransits in total with 113^{+22}_{-13} of these being biennial duotransits where both transit events are observed more than a year apart.

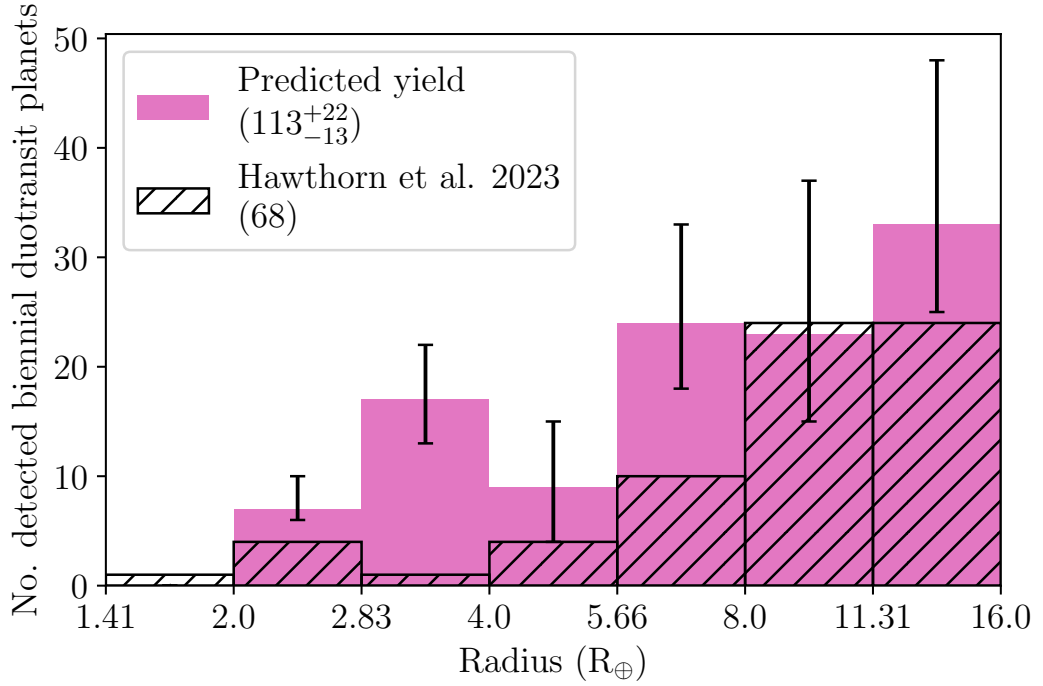
The distribution of biennial duotransits is shown in Figure 2.12. Compared to monotransit detections (see Section 2.4.3) we find that the sample of planets detected from biennial duotransits show a flatter distribution in radius, with 21% of biennial duotransit detections coming from planets below $4R_{\oplus}$ compared to 6% of monotransits, although radii $> 11.31R_{\oplus}$ are still the largest bin of detections. We find the period of expected biennial duotransits peaks between 25 and 50 days and falls off more rapidly than monotransits for longer-periods with 6% of biennial duotransits coming from periods > 100 days compared to 40% of monotransits.

2.4.5 Breakdown by Spectral Type

As shown in Figure 2.9c, we find G dwarfs should be host to the most detections (1005^{+143}_{-103}), followed by K (551^{+123}_{-54}) and F (500^{+130}_{-67}) dwarfs in quick succession with a reasonable number from M dwarfs (151^{+66}_{-20}) and a very small number from



(a) Period distribution of predicted biennial duotransit yield



(b) Radius distribution of predicted biennial duotransit yield

Figure 2.12: Predicted yields of biennial duotransit planets detected from one transit in Year 1 and another in Year 3. Shown in distributions of period (a) and radius (b). Plot (b) also shows a comparison with the radii of biennial duotransits from Hawthorn et al. [2023a] excluding candidates over $16R_{\oplus}$ which we do not simulate.

A dwarfs (64^{+21}_{-11}). This distribution is largely due to the numbers of each spectral type represented in the SPOC FFI sample with G types being the most numerous and thus host to the most detected planets.

Figure 2.9d shows the yield from each spectral type divided by the number of stars of that spectral type in the SPOC sample. From this it becomes apparent that K dwarfs are the most numerous hosts of detections per star with a rate of $(3.4^{+0.8}_{-0.3}) \times 10^{-3}$ transiting planets per star observed. G dwarfs are the next most efficient sources of detections with $(2.4^{+0.3}_{-0.2}) \times 10^{-3}$ predicted per star, followed by M with $(1.2^{+0.5}_{-0.2}) \times 10^{-3}$, F with $(0.99^{+0.26}_{-0.13}) \times 10^{-3}$ and A with $(0.72^{+0.24}_{-0.12}) \times 10^{-3}$.

K dwarfs sit at the best crossover between occurrence rates and *TESS*’ detection efficiency, and thus have the highest rate of detections per star. Despite M dwarfs having higher planetary occurrence rates than AFGK stars [Dressing & Charbonneau, 2015] and their small size causing deeper transits due to a higher planet-star radius-ratio, they display a relatively low rate of detections per star. M dwarfs host many small radius planets compared with AFGK dwarfs, but fewer giant planets. These small planets produce low SNR signals that result in low detection probabilities for M dwarf host stars. This results in fewer detections per star for M dwarfs.

Figure 2.13 shows the proportion of different period ranges in the predicted yield by spectral type. We find a reasonably flat trend in the distribution of long-period discoveries for each spectral type with a possible minor trend towards shorter-period discoveries being favoured at later spectral types, although increasingly small numbers create uncertainty in such a trend.

2.4.6 Comparison of Detection Probability Functions

As well as the gamma function described in Section 2.2.4 we also calculate yields using simple signal to noise thresholds of 7.3 and 20. Figure 2.14 shows a comparison of the results from these three approaches.

The predicted total yield using a $\text{SNR} \geq 20$ threshold of 1555^{+216}_{-126} shows a strong agreement with the total number of TOIs from the Year 1 and 3 SPOC FFI discoveries (1666). However Figure 2.14 demonstrates that the predicted distribution in periods and radii from this criterion does not match the proportions of the TOI sample as well as other methods. We see a significant under-prediction of planet yields for radii below $5.66R_{\oplus}$ which increases in disagreement for decreasing radii from this method as shown in Figure 2.14b. We also find that the yields for short period planets ($P < 25$ days) are under-predicted by this method, with the largest deficit being between 3.13 and 6.25 days

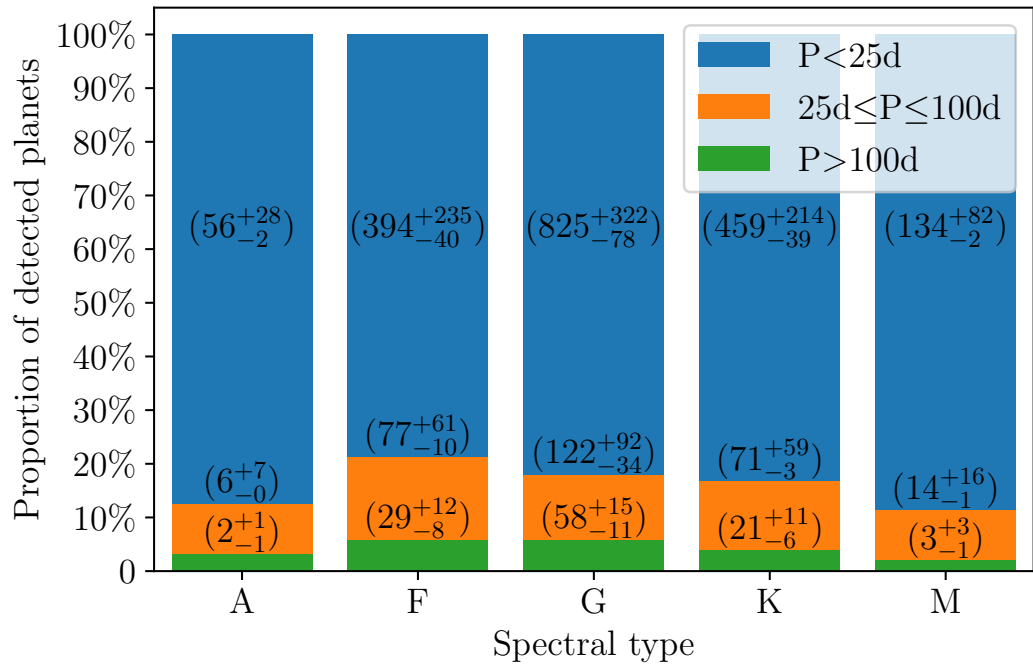
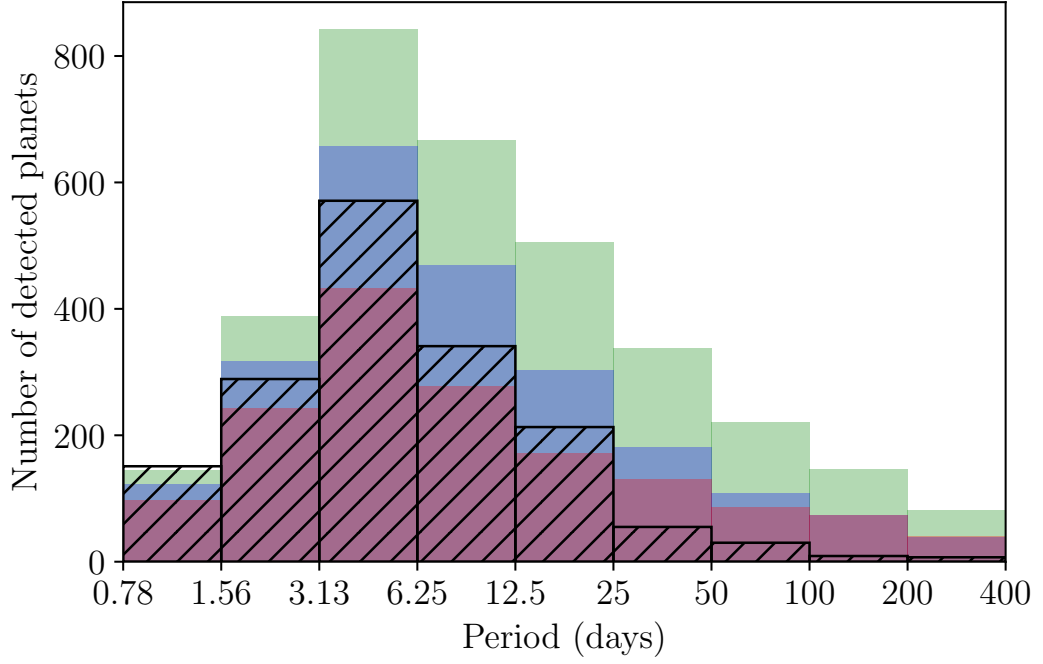
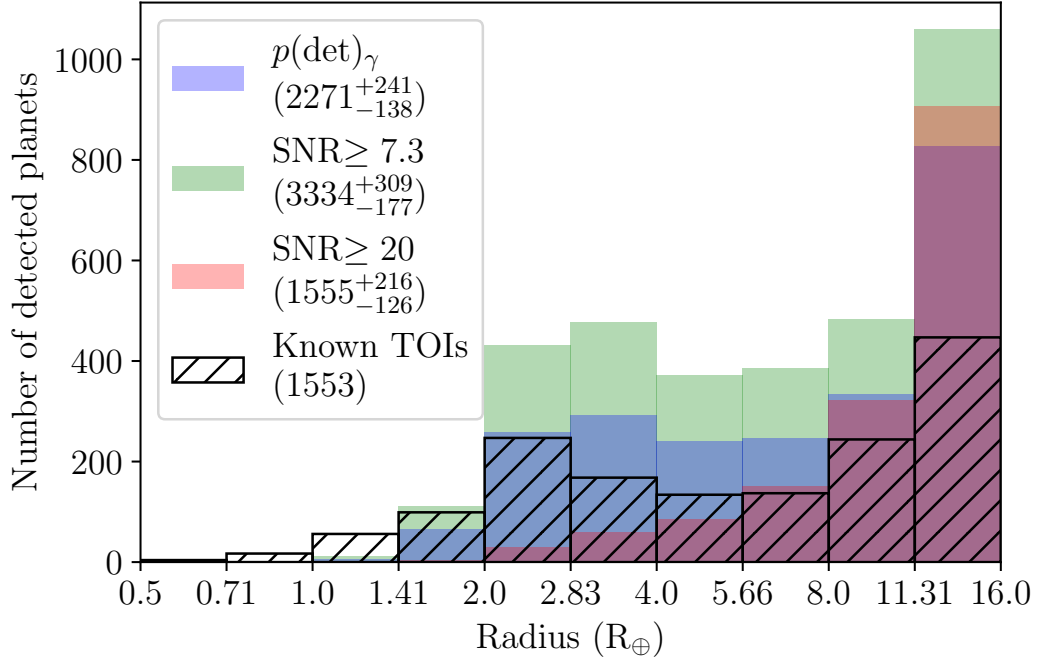


Figure 2.13: Comparison of the proportions of predicted long-period planet yield by spectral type. Planets with periods less than 25 days are shown in blue, periods between 25 and 100 days are shown in orange and periods longer than 100 days are shown in green. The predicted yield numbers for each spectral type and period range are printed on the plot, along with the associated uncertainties.



(a) Period distribution of predicted yields for three detection criteria



(b) Radius distribution of predicted yields for three detection criteria

Figure 2.14: Comparison of the yields predicted using three different detection criteria, a gamma cumulative distribution (blue), and signal to noise thresholds of 7.3 (green) and 20 (red). Distributions are shown in period (a) and radius (b).

Using a smaller SNR threshold of 7.3 as many yield studies have done previously [e.g; Sullivan et al., 2015; Bouma et al., 2017; Barclay et al., 2018; Cooke et al., 2018, 2019; Villanueva et al., 2019], we find a significantly greater yield prediction than either the threshold of $\text{SNR} \geq 20$ or the gamma function. The predicted yield of planets with $\text{SNR} \geq 7.3$ (3334^{+309}_{-177}) is more than double the size of the TOI discoveries and the yield predicted by $\text{SNR} \geq 20$ and around 1.5 times greater than that predicted by the gamma function. A large fraction of this additional predicted yield comes from small planets and longer period planets as shown in Figure 2.14.

2.5 Discussion

2.5.1 Comparison to actual *TESS* detections

Comparison to the population of *TESS* transiting planet discoveries via the TOI catalogue is a relatively straightforward and robust check for the **TIaRA** yield results. We cross-match the TIC IDs of the TOI catalogue with stars we simulated from the SPOC FFI sample to compare against our predicted yields as shown in Figure 2.9.

Our total predicted yield of 2271^{+241}_{-138} is $\sim 4.4\sigma$ greater than the total number of TOIs (1666) as of 2023-06-15. However, for orbital periods less than 6.25 days the **TIaRA** predictions agree with the discoveries to within uncertainties. For periods between 6.25 and 25 days the **TIaRA** predictions are not more than 2σ above the discoveries. However for planets with periods greater than 25 days the deficit between **TIaRA** predictions and TOI discoveries becomes increasingly significant as shown in Figure 2.15.

The SPOC Transiting Planet Search [TPS; Jenkins et al., 2016; Guerrero et al., 2021] relies on phase folding data to search for periodic signals [Guerrero et al., 2021]. This becomes increasingly difficult for longer-periods as such planets may have transits in different *TESS* sectors or only one transit which is impossible to phase fold. This suggests that the difference between our predicted yield and the TOI sample may be due to *TESS* discoveries being currently incomplete for longer-period planets. Since the majority of candidates are given TOI status by the TPS [Guerrero et al., 2021], many monotransit and biennial duotransit events in the SPOC FFI lightcurves may have yet to be detected.

We can gain an indication of this by comparing our predicted yield with and without monotransits to the TOI sample. When we remove monotransits from our predicted yield we find 2056^{+245}_{-140} detected exoplanets and excluding biennial duotransits we further reduce this to 1943^{+246}_{-141} . This brings our yield into closer alignment with the TOI detections [Taken from NASA exoplanet archive; Akeson

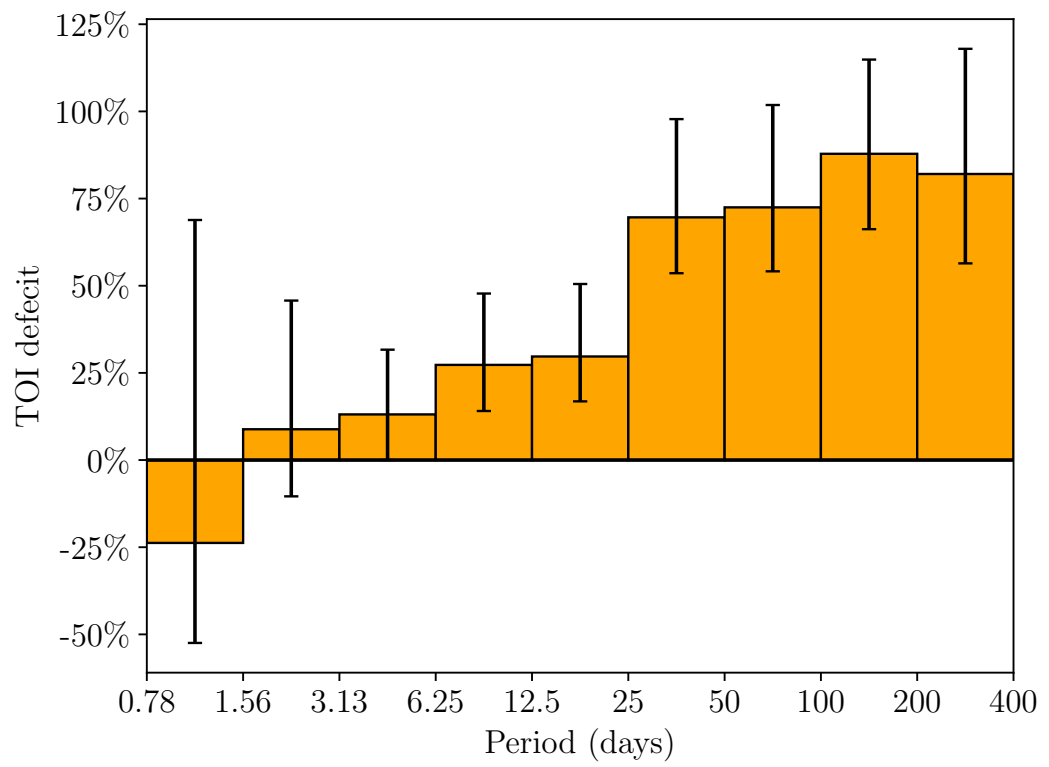


Figure 2.15: Percentage deficit between the discovered TOIs and our predicted yield for the *TESS* SPOC FFI lightcurves from Year 1 and Year 3.

et al., 2013] from 4.4σ to 2.8σ and 2.0σ respectively.

This could also explain the seeming overabundance of giant planets as seen in Figure 2.9b as long-period monotransit and duotransit detections are particularly biased towards larger radii (see Figures 2.10b and 2.12b), and hence the undiscovered long-period planets make up the majority of the undiscovered giant planets as well. Additionally it could explain the overestimation of planets detected around G and K dwarfs shown in Figures 2.9c and 2.9d. As these stars make up the largest numbers of stars in the SPOC FFI sample and have the highest detection rate per star, it is likely that most of the long-period and other planets not yet found would be around these.

2.5.2 Comparison to Biennial Duotransit search

We are able to compare our predicted yield of biennial duotransit detections with a real search of the Year 1 and Year 3 SPOC FFI lightcurves for biennial duotransits set out in Hawthorn et al. [2023a]. Figure 2.12b shows the distribution of the **TIaRA** predicted yields and the sample from Hawthorn et al. [2023a] in radius. The periods of the majority of candidates in Hawthorn et al. [2023a] are currently unknown and so cannot be compared directly to our prediction. Our predicted yield of biennial duotransits is 113^{+22}_{-13} , which is 3.5σ greater than the 68 candidates in the real sample. The numbers are in close agreement for radii between 8.0 and $11.31 R_{\oplus}$ and near agreement for 11.31 to $16 R_{\oplus}$. However for smaller radii planets ($R < 4R_{\oplus}$), **TIaRA** predicts many more biennial duotransits than are detected in Hawthorn et al. [2023a], especially between 2.83 and $4 R_{\oplus}$. This is to be expected as Hawthorn et al. [2023a] only consider high SNR biennial duotransits, which will be produced by larger planets. We note that Hawthorn et al. [2023a] also have a significant number of candidates with radii larger than $16R_{\oplus}$, however we do not consider such large radius objects in our **TIaRA** simulation.

We also note the strong agreement between the predicted number of biennial duotransits with $\text{SNR} \geq 20$ of 86^{+25}_{-13} and the discovery of 68 biennial duotransits from Hawthorn et al. [2023a]. The effect of using different probability of detection functions is discussed further in Section 2.5.5.

2.5.3 Comparison to previously predicted yield

In addition to comparing our results to the TOI catalogue (see Section 2.5.1) we can also check the validity of our results by comparing them to previous attempts at predicting yield. This is especially useful as our methods include monotransits,

which are not included in studies such as Kunimoto et al. [2022].

Kunimoto et al. [2022] use a considerably larger population of stars. We have simulated the yield from the ~ 1.3 million stars in the Year 1 and Year 3 SPOC FFI sample. Kunimoto et al. [2022] use 4 million stars from the *TESS* Candidate Target List [CTL; Stassun et al., 2019]. Therefore we normalise each set of results by the number of stars in each sample and compare in terms of number of planets predicted per star (similarly to in Figure 2.9d) for ease of comparison. However, it should be noted that the selection criteria for each stellar sample, especially for SPOC stars [Caldwell et al., 2020], introduces biases in the average detectability for each stars, so this is somewhat of a crude comparison.

Kunimoto et al. [2022] predict a total of 2532 ± 189 exoplanets found around 4066063 stars in Year 1 and 1748 ± 103 around 4021948 stars in Year 3. This gives a total of $(1.06 \pm 0.05) \times 10^{-3}$ detections per star. This is 6.5σ below our estimate of $(1.55^{+0.18}_{-0.11}) \times 10^{-3}$ per star excluding monotransits. It is to be expected that our yield prediction will be greater than Kunimoto et al. [2022] since we use the SPOC FFI sample, which has been explicitly created to target stars that are most likely to have detectable transits with *TESS* [Caldwell et al., 2020].

2.5.4 Occurrence Rates

The *TTaRA* yield predictions rely on the occurrence rates from Kunimoto & Matthews [2020] for AFGK stars and a modified occurrence rate from Dressing & Charbonneau [2015] for M dwarfs.

The occurrence rates we use from Kunimoto & Matthews [2020] do not include any planets larger than $16R_{\oplus}$ although larger planets are known to exist and are likely to be detectable by *TESS* even if the occurrence rates from *Kepler* are known to be low [Fressin et al., 2013; Hsu et al., 2019; Kunimoto & Matthews, 2020]. Future yield estimate studies could benefit from studies into the occurrence rate of planets larger than $16R_{\oplus}$ which could be carried out on samples of planets from *TESS*.

Due to the lack of occurrence rate studies on A and earlier spectral-type stars, we assume the occurrence rates of planets around A and earlier type stars are equal to that of F type stars (see Section 2.3.7). In reality these may be different as the higher mass and temperature of A type stars are expected to have significant effects on planet formation and thus the occurrence rate [Johnson et al., 2010]. Future studies could benefit from *TESS* derived occurrence rates of A type stars [e.g; Zhou et al., 2019; Johnson, 2023].

For M dwarfs we rebin the values found by Dressing & Charbonneau [2015] onto the same grid used by Kunimoto & Matthews [2020]. While this does, of course,

change the exact values for M dwarf occurrence rates, due to the large errors on the values from Dressing & Charbonneau [2015] we believe our values for occurrence rates within the original bounds of this grid ($0.5R_{\oplus} \leq R_p \leq 4R_{\oplus}$, $0.5 \text{ days} \leq P \leq 200 \text{ days}$) are robust. As discussed in Section 2.3.7 we expect the yields of planets with periods between 200-400 days from *TESS* to be low and thus treat these bins as unconstrained with only an upper bound value. Furthermore we estimate values for planets between 4 and $16 R_{\oplus}$ around M-dwarfs using the values found for K dwarf stars by Kunimoto & Matthews [2020] but reduced by a factor of one half to account for the expected lower occurrence rate of giant planets around M dwarfs [Sabotta et al., 2021; Bryant et al., 2023]. To improve the accuracy of future yield estimations, it would be useful to constrain giant planet occurrence rates around M dwarfs as discussed in Bryant et al. [2023] and Sabotta et al. [2021]. It is also worth noting that by rebinning the rates for M dwarfs we increase the shortest possible period of planet we simulate from 0.5 days to 0.78 days, this means we are likely to underestimate yields in this region of period-space as *TESS* has already found candidates [NASA Exoplanet Archive; Akeson et al., 2013] and 9 confirmed planets [Vanderspek et al., 2019; Giacalone et al., 2022; Luque & Pallé, 2022; Essack et al., 2023; Goffo et al., 2023] in this region.

2.5.5 Probability of detection

As set out in Section 2.2.4, we use an incomplete gamma function to estimate the probability of detection in the *TIaRA* simulation following Christiansen [2017]; Hsu et al. [2019] and Kunimoto et al. [2022]. As discussed in Kunimoto et al. [2022], there are some caveats associated with the use of this probability of detection function:

1. *Kepler* monitored a different population of stars and had different light curve properties to *TESS*. While our use of real *TESS* lightcurves allows us to account for many of the unique properties of *TESS* data we still are applying a probability of detection function developed for *Kepler* to a very different mission. It would be useful for work similar to that of Christiansen [2017] and Hsu et al. [2019] on *Kepler* DR25 to be performed on *TESS* to gain a more accurate understanding of the false positive rate and detection efficiency of *TESS*.
2. We perform a linear extrapolation for the detection efficiency of duotransit and monotransit events in *TESS*. While we believe the result to be reasonable as it produces the lower detection efficiency we expect for such events it is not based on the same rigorous testing done by Christiansen [2017] and Hsu et al. [2019] for 3 transit and greater events. Furthermore monotransits are often not

found by the same algorithms that search for multitransit events and thus the probability of detection may not scale down linearly with number of transits down to the level of a monotransit. For this reason it is also worth considering a simple $\text{SNR} \geq 20$ threshold for monotransits as discussed in Section 2.4.6.

Additionally, as shown in Section 2.4.6 the use of a gamma function, and SNR thresholds of 7.3 and 20 all recover a deficit in the number of long-period planets compared with the sample of TOI discoveries. This provides additional evidence for the potential of undiscovered long-period planets in *TESS* data.

2.5.6 Use of Year 1 and Year 3 SPOC FFI Lightcurves

In our simulation we use Year 1 and Year 3 SPOC FFI lightcurves which gives us a stellar population of ~ 1.3 million stars in the southern ecliptic hemisphere. This sample is selected in part due to computational limits of SPOC [Caldwell et al., 2020], and *TESS* observes many more stars at sufficient precision to detect transiting exoplanets. Thus the total planetary yield from the *TESS* mission will be higher than those from just the SPOC FFI targets as we simulate here. However, the SPOC FFI sample prioritises bright, main sequence targets with low levels of dilution from other sources to fill the maximum of 160000 targets per sector [Caldwell et al., 2020]. The Candidate Target List [CTL; Stassun et al., 2019], as used by Kunimoto et al. [2022], uses a similar prioritisation metric but with a higher number of selected targets. This difference results in a smaller sample for SPOC, but with a greater proportion of targets most amenable to small planet detection. In future, it would be interesting to run **TIaRA** on a larger sample of lightcurves, such as those generated by the Quick Look Pipeline [QLP; Huang et al., 2020].

2.6 Summary and Conclusion

We develop the **TIaRA** pipeline to simulate the sensitivity of transit surveys to detecting transiting exoplanets. We focus in this paper on the Year 1 and Year 3 SPOC FFI sample from the *TESS* mission. In particular we are interested in the sensitivity and yield for longer-period planets that present as monotransits or biennial duotransits in the data. Our simulations is based on the actual stars monitored by *TESS* and the real *TESS* window functions (accounting for discontinuities in observations). We also use the actual noise properties of the lightcurves for each star.

We find a total of 2271^{+241}_{-138} exoplanets should be detected around AFGKM dwarf host stars in the Year 1 and Year 3 SPOC FFI lightcurves. Of these 403^{+64}_{-38}

will have orbital periods greater than 25 days and 113^{+23}_{-17} will have orbital periods greater than 100 days. We find 4.4σ more predicted detections than the current TOI sample size of 1666. We find an increasing disparity between our predictions and actual *TESS* discoveries from the TOI catalogue at longer-periods, suggesting that the *TESS* discovery sample is incomplete at longer-periods and more long-period planets remain to be discovered in *TESS* data.

These additional planets will require concentrated follow-up efforts to confirm as the majority of them will be initially detected as some of the 215^{+37}_{-23} predicted *TESS* monotransits. 50% of planet detections with periods above 25 days and 76% of planet detections above 100 days will be monotransits. Aside from monotransits, a large portion of the remaining long-period planets will be found as biennial duotransit events with one transit in Year 1 and an additional in Year 3, with 113^{+22}_{-13} of these discoveries detected.

The **TIaRA** pipeline developed for this project can be applied to additional *TESS* data sets such as the northern ecliptic hemisphere SPOC FFI lightcurves from Years 2 and 4 and the upcoming release of the remaining Year 5 SPOC FFI lightcurves. The QLP lightcurves [Huang et al., 2020] could also be analysed using **TIaRA**. Reasonable assumptions of the observing strategy and current performance of *TESS* could also be used to create simulated lightcurves and make predictions of future *TESS* extended missions. With simulated data, **TIaRA** can easily be used to predict the yields from future missions, in particular the upcoming PLANetary Transits and Oscillations of stars [*PLATO*; Rauer et al., 2014] mission.

2.7 Appendix

2.7.1 Sensitivity by spectral types

2.7.2 Yield by spectral type

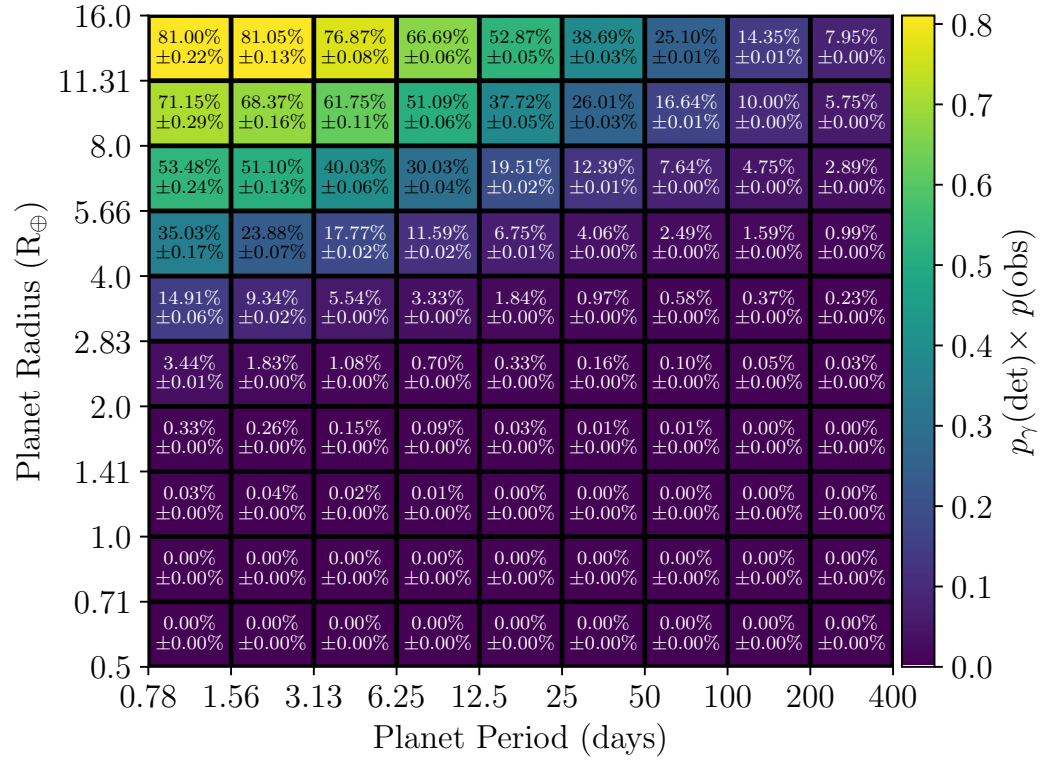


Figure 2.16: Sensitivity map showing the probability of a transiting exoplanet being observed and detected around an A dwarf in the Year 1 and Year 3 *TESS* SPOC FFI lightcurves.

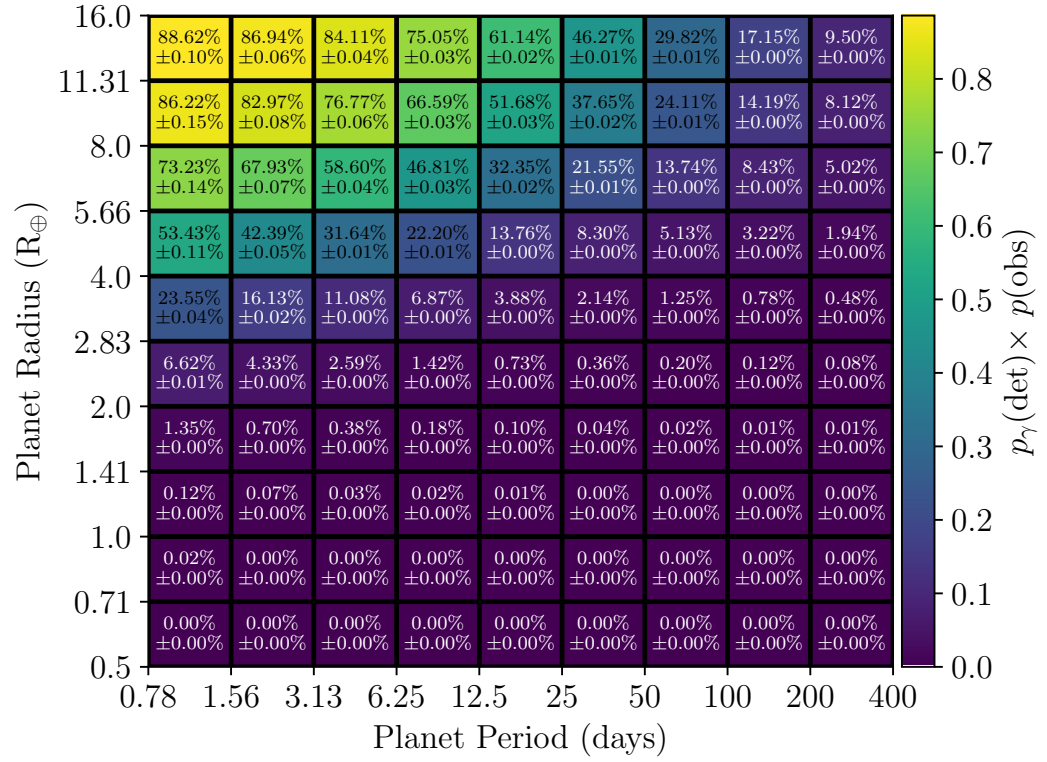


Figure 2.17: Sensitivity map showing the probability of a transiting exoplanet being observed and detected around an F dwarf in the Year 1 and Year 3 *TESS* SPOC FFI lightcurves.

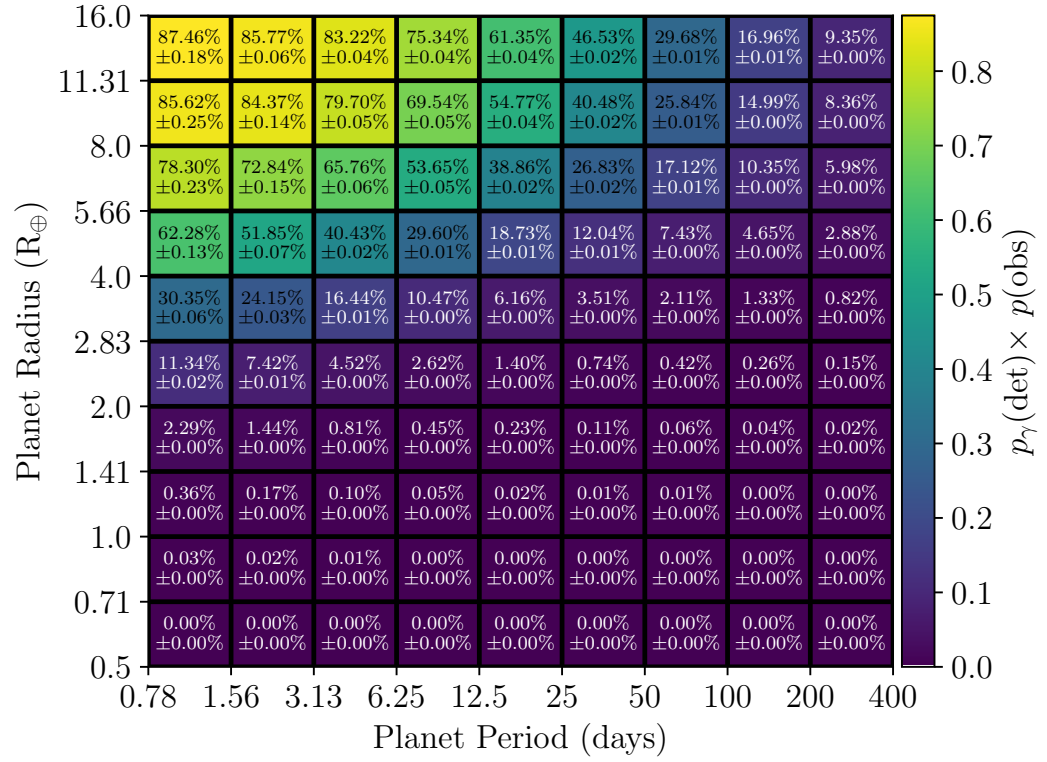


Figure 2.18: Sensitivity map showing the probability of a transiting exoplanet being observed and detected around a G dwarf in the Year 1 and Year 3 *TESS* SPOC FFI lightcurves.

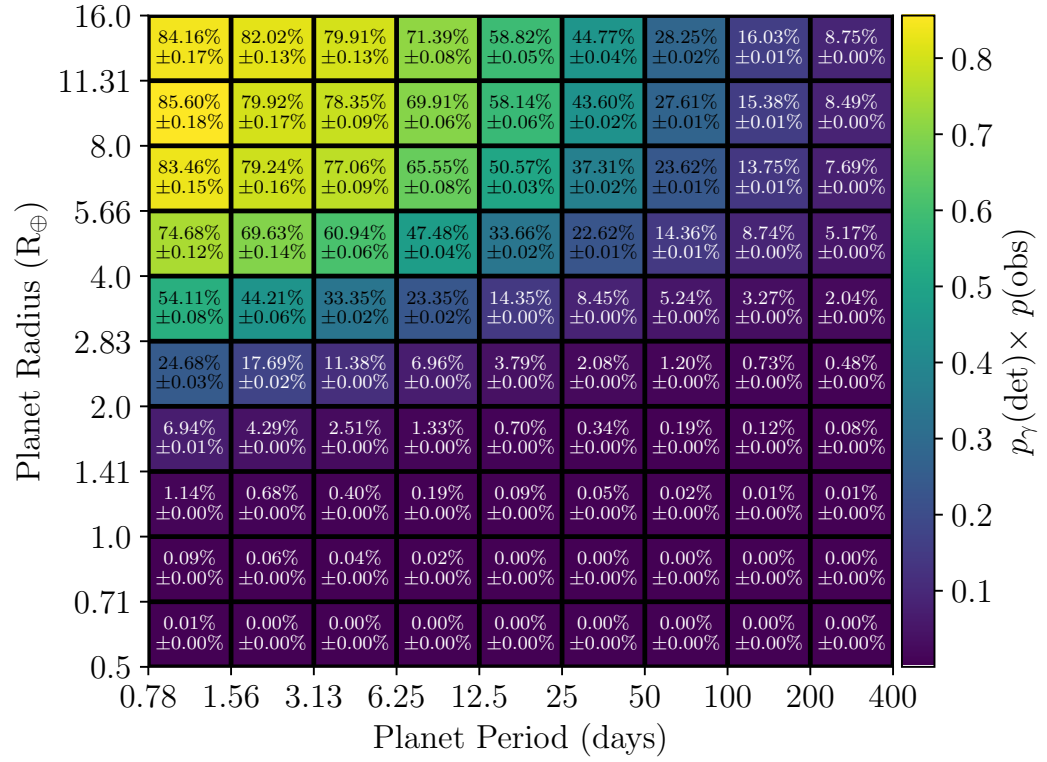


Figure 2.19: Sensitivity map showing the probability of a transiting exoplanet being observed and detected around a K dwarf in the Year 1 and Year 3 *TESS* SPOC FFI lightcurves.

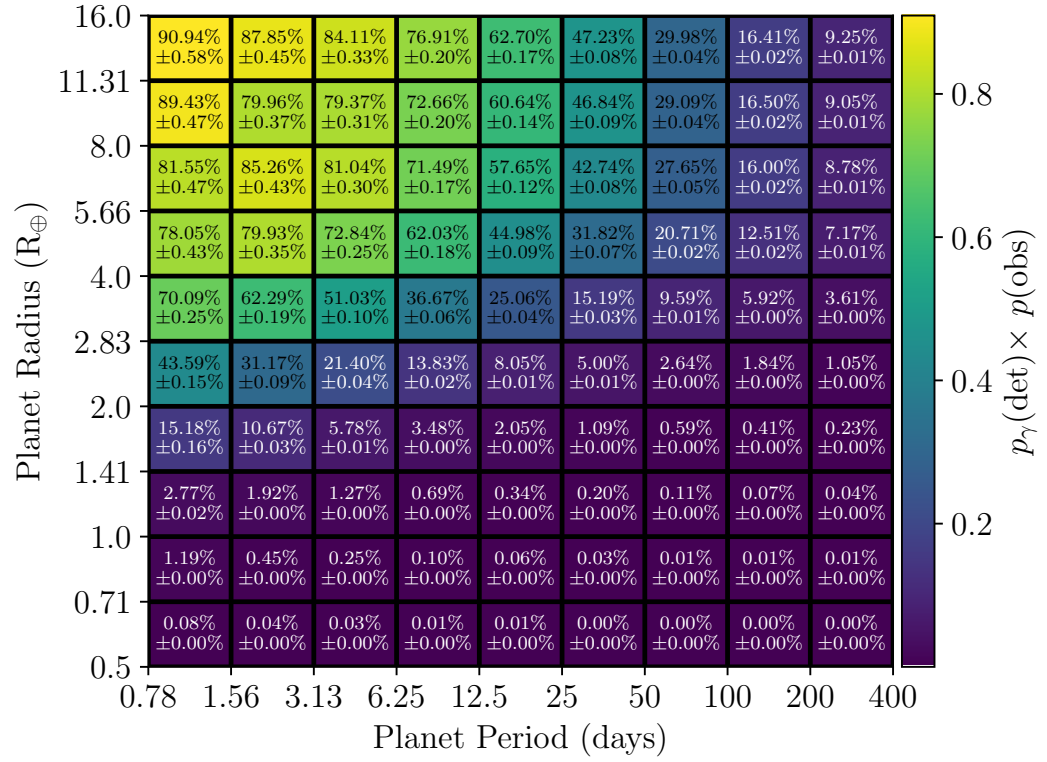


Figure 2.20: Sensitivity map showing the probability of a transiting exoplanet being observed and detected around an M dwarf in the Year 1 and Year 3 *TESS* SPOC FFI lightcurves.

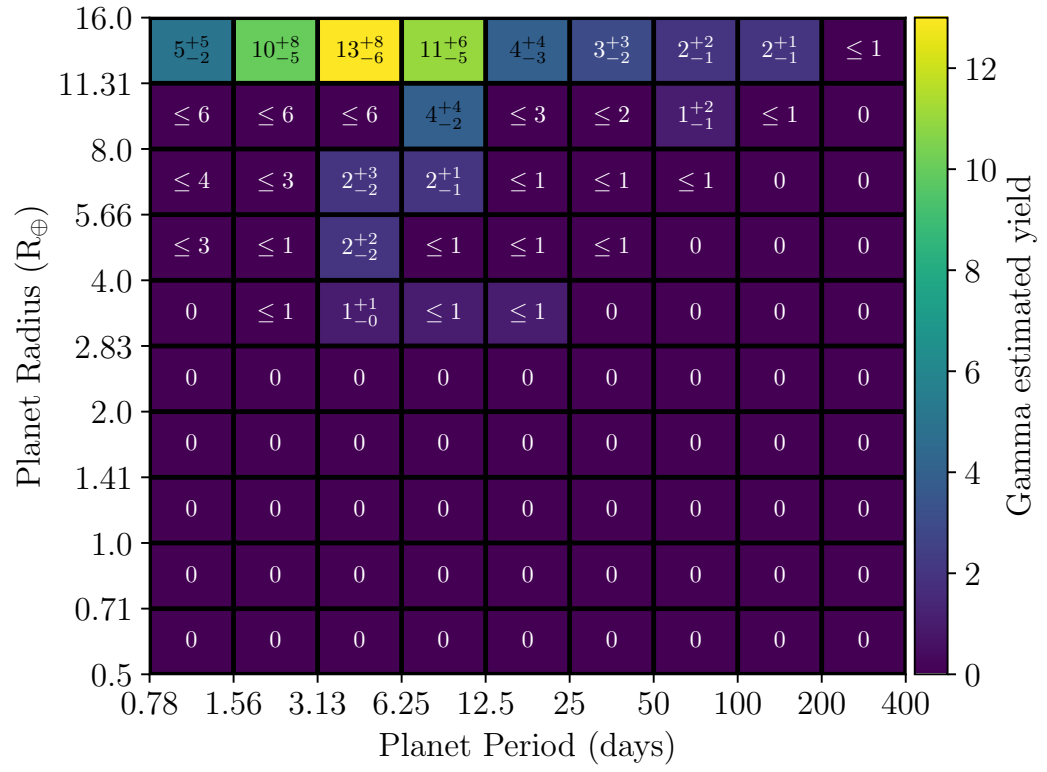


Figure 2.21: Predicted yields of transiting exoplanets around A dwarf stars from the Year 1 and Year 3 *TESS* SPOC FFI lightcurves.

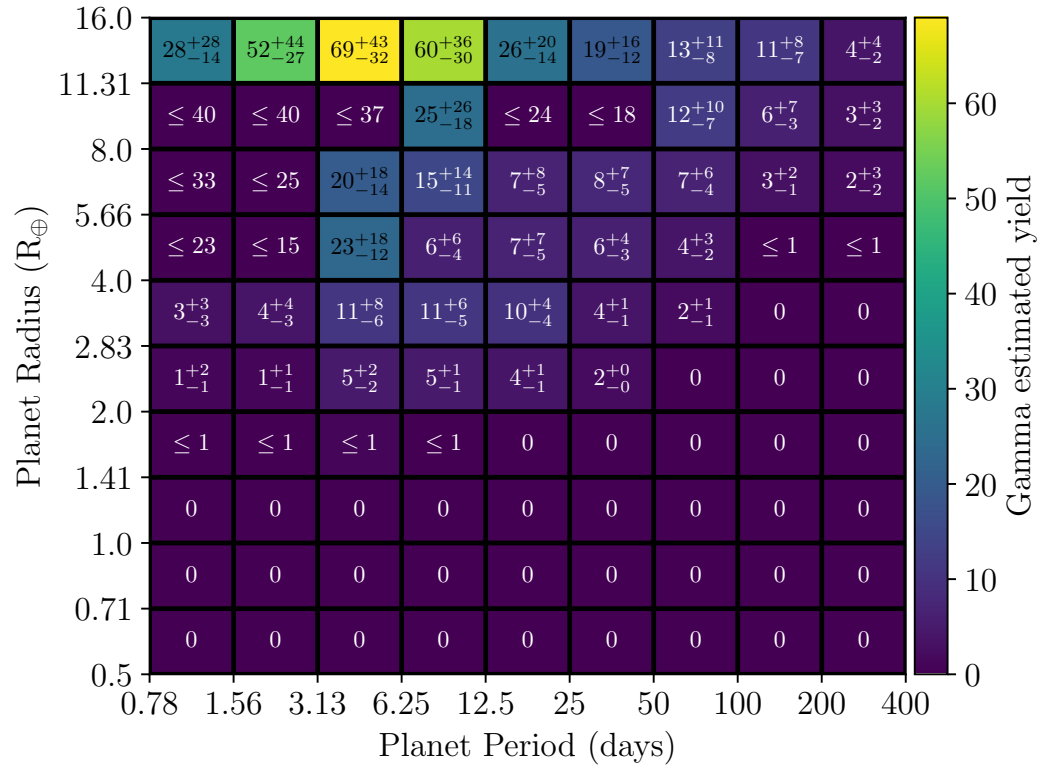


Figure 2.22: Predicted yields of transiting exoplanets around F dwarf stars from the Year 1 and Year 3 *TESS* SPOC FFI lightcurves.

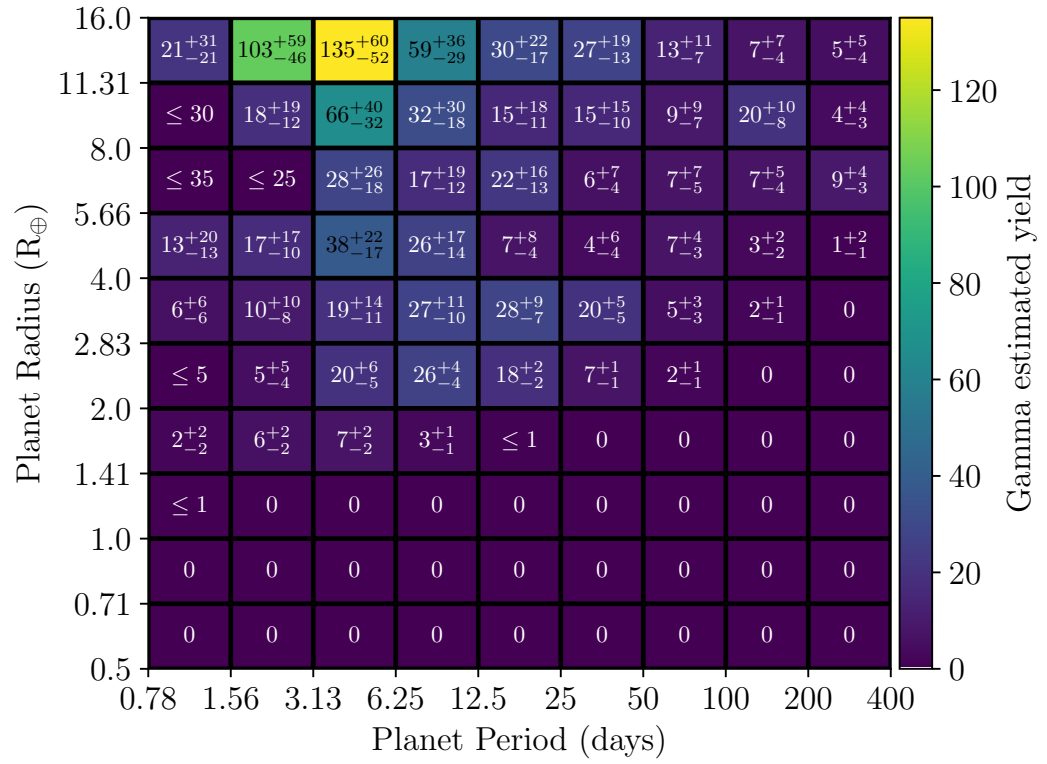


Figure 2.23: Predicted yields of transiting exoplanets around G dwarf stars from the Year 1 and Year 3 *TESS* SPOC FFI lightcurves.

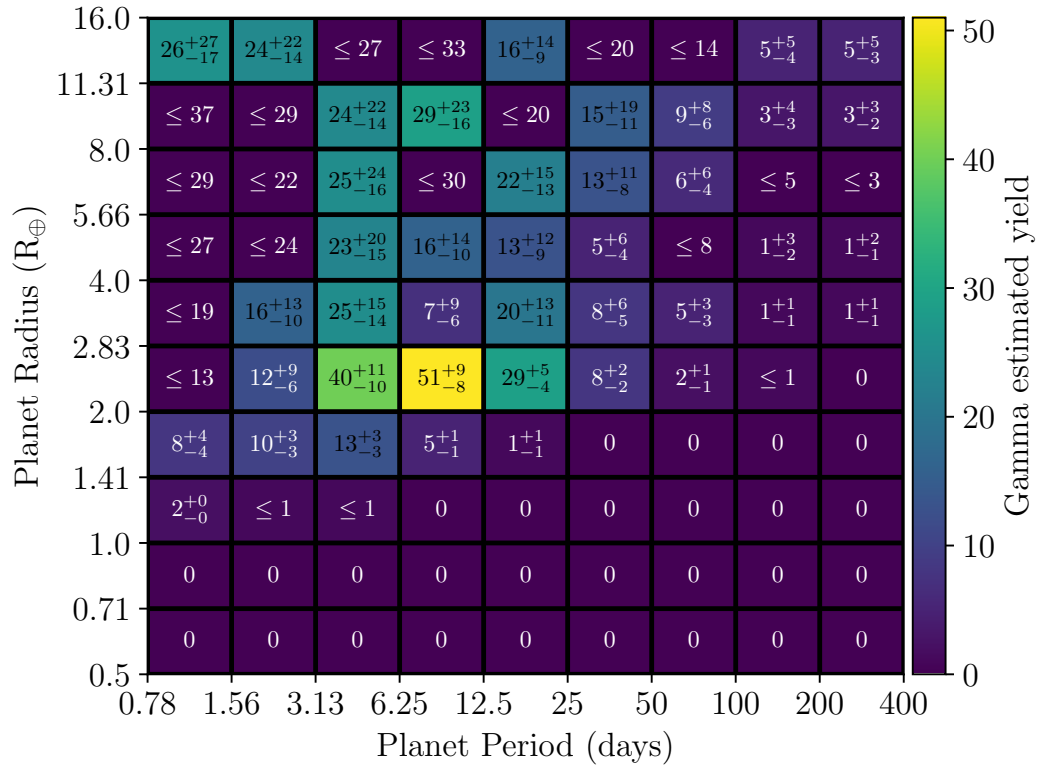


Figure 2.24: Predicted yields of transiting exoplanets around K dwarf stars from the Year 1 and Year 3 *TESS* SPOC FFI lightcurves.

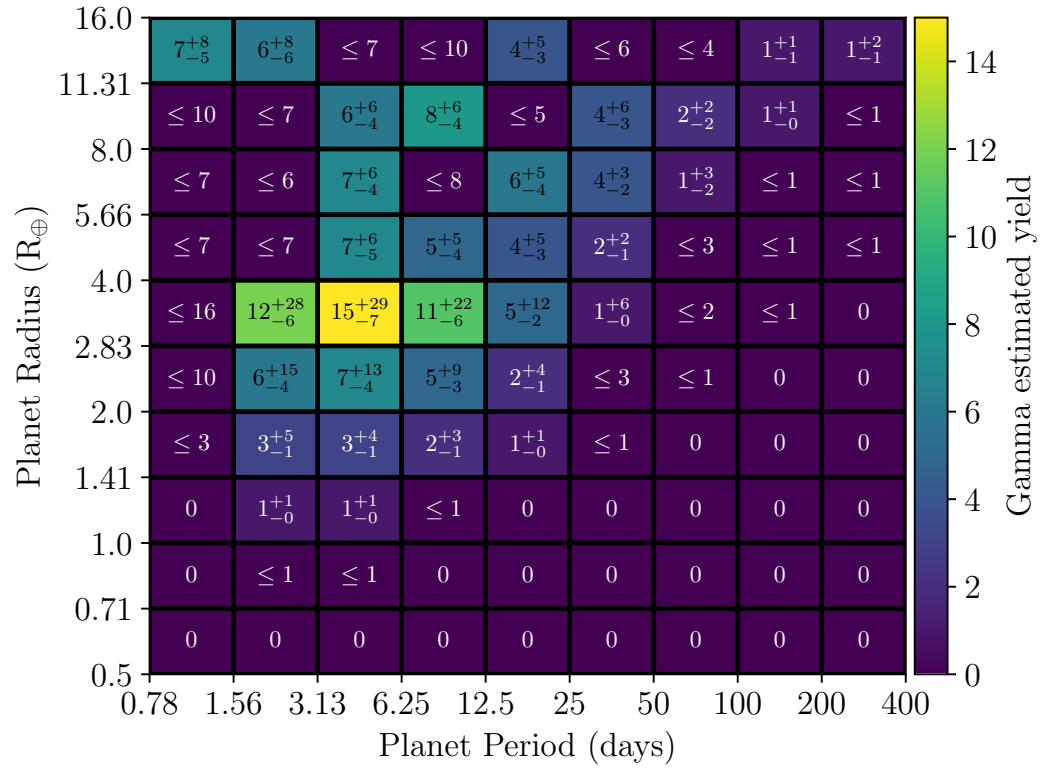


Figure 2.25: Predicted yields of transiting exoplanets around M dwarf stars from the Year 1 and Year 3 *TESS* SPOC FFI lightcurves.

Chapter 3

Future work and Conclusion

"Upgrades people! Upgrades!"

Phineas T. Ratchet

Robots (2005)

3.1 Summary of Key Results

From the simulation presented in Chapter 2, we predict a total yield of 2271^{+241}_{-138} exoplanets detected around AFGKM dwarf stars from the *TESS* Year 1 and Year 3 SPOC FFI lightcurves. Of these 403^{+64}_{-38} will have orbital periods greater than 25 days and 113^{+23}_{-17} will have orbital periods greater than 100 days.

We find our results are in agreement with the actual *TESS* TOI discoveries for short periods but over-estimate the TOI discoveries to date for systems with periods beyond 6.25 days. This suggests that the TOI sample is incomplete at longer periods and more long-period planets remain to be found in the SPOC FFI data. We also find our results match proportionally with the predictions of Kunimoto et al. [2022] for shorter periods, but we predict a greater proportion of longer-period giant planets due to our inclusion monotransit discoveries.

We predict 215^{+37}_{-23} monotransit detections, the vast majority of which will be from giant planets with periods of 25 days or greater. We find that the re-observation of Year 1 fields in Year 3 pushes the distribution of these monotransits out to longer periods and we expect Year 5 observations to compound this effect. We also find that the addition of Year 3 to Year 1 data will cause more longer-period planets to have two transits detected, we predict that 113^{+22}_{-13} year 1 monotransits will be detected with an additional transit in year 3. While these "biennial duotransits" do

not allow for as many detections as monotransits out to periods of 100 days or more, they provide a population of planets with periods of 25 days or greater which are easier to follow up due to easier estimation of period aliases.

Surprisingly, we find that K dwarfs appear to be the most efficient host stars for planet detection by *TESS*. K dwarfs have the best intersection of occurrence rates of planets and *TESS* sensitivities to maximise detections per star observed. This may have implications for target selection in future *TESS* missions or other transit surveys such as *PLATO*.

In our work we adopt a gamma function as a detection metric [as in; Christiansen, 2017; Hsu et al., 2019; Kunimoto et al., 2022] instead of a traditional signal to noise cutoff as previous studies have done. We find this to be a more robust detection metric as it is less arbitrary than a signal to noise cut and produces a more realistic distribution of detections. Interestingly, we find that our gamma function and signal to noise thresholds of 7.3 and 20 all predict more long-period planets than the current TOI sample.

3.2 Future Work on *TESS*

In Chapter 2 we presented a study using **TIaRA** to process the SPOC lightcurves from year 1 and year 3 observations of the current ecliptic hemisphere. *TESS* data already exists from sources beyond those in that set, and future observations will supply even more. It seems natural that **TIaRA** should be used on these additional current and future *TESS* data sets. In the remainder of this section we discuss other sets of *TESS* lightcurves which would benefit from analysis and the potential application of **TIaRA** to estimating occurrence rates.

3.2.1 Northern ecliptic Hemisphere: Year 2 and Year 4

We prioritized the southern ecliptic hemisphere SPOC FFI data. This has strong synergies with the monotransit follow-up work of *NGTS* (see Section 1.5.1) and other facilities which are located in the southern hemisphere. As such the paper we present in Chapter 2 contains the Year 1 and Year 3 SPOC FFI data. However, a **TIaRA** run has already been completed on the Year 2 and Year 4 SPOC lightcurves. The simulation output now requires additional processing and writing to present in a scientific paper. The northern ecliptic hemisphere has less coverage by *TESS* than the south (see Figure 1.18) and Year 4 also contains coverage of the ecliptic plane (see Section 1.6.2 itself which was not observed previously. These effects will certainly

influence the yield of monotransits and duotransits which we will be able to quantify when the simulation output is analysed.

3.2.2 Update to southern ecliptic with Year 5

At the time of writing, *TESS* is undergoing its second extended mission and 5th year of observations. Year 5 of *TESS* covers both the northern and southern ecliptic including some, but not all regions previously observed in Years 1 and 3 (see Section 1.6.2). Year 5 observations are not yet fully processed by the SPOC FFI pipeline. Once the Year 5 SPOC FFI lightcurves for the southern ecliptic hemisphere are available they can be processed by **TIaRA** to provide an update to the yield of long-period planets from another year of *TESS* observations. It will be important to determine how many previously unsolved periods Year 5 data will solve and how the numbers of monotransits and duotransits will evolve. Year 5 will also result in systems with three transits but unsolved periods as a transit occurs once in each year of *TESS* data.

3.2.3 Quick Look Pipeline (QLP) lightcurves

We elected to use SPOC FFI lightcurves because they give us a readily available, high quality homogeneous data set. Furthermore the *NGTS* monotransit working group uses the SPOC lightcurve in its search for *TESS* monotransits so this provided an easy point of comparison. However SPOC produces FFI lightcurves for ~ 160000 stars per *TESS* sector which is only a relatively small fraction of the stars actually observed by *TESS* [Caldwell et al., 2020]. A larger set of lightcurves can be found from the Quick Look Pipeline [QLP; Huang et al., 2020], which produced ~ 14.8 million lightcurves for year 1, compared to ~ 2 million SPOC lightcurves. A larger number of targets, such as in the QLP sample, will give us a more representative sample of stars and therefore more precise detection sensitivities.

Computational runtime will increase for applying **TIaRA** on a larger dataset such as the QLP lightcurves. The QLP sample is approximately seven times larger than the SPOC FFI sample, so we would expect **TIaRA** to take seven times longer to run a similar yield analysis. For the Year 1 and Year 3 SPOC FFI sample, **TIaRA** ran for approximately one week using four cores of a standard desktop PC. We would therefore expect we could run **TIaRA** on the QLP sample in approximately two months with the same computing configuration. However with more computational resources (such as a computer cluster or supercomputer) this could easily be reduced to a more manageable time-frame. There are also additional gain in performance

that can be achieved by upgrades to the speed of the **TIaRA** pipeline (see Section 3.4).

3.2.4 Future *TESS* sectors

TESS is still in its second extended mission at the time of writing. Year 6 of *TESS* has begun and will provide an additional data set which can be processed by **TIaRA** in the relatively near future.

A third extended mission and maybe even a fourth and fifth seem likely as *TESS* shows no major signs of degradation and has sufficient fuel resources onboard the spacecraft to continue [Ricker et al., 2015]. As more data sets become available, **TIaRA** can be used to make sensitivity maps and estimate yields to assess the completeness of discoveries. Additionally, reasonable assumptions about the performance and strategy of *TESS* so far could be used to simulate lightcurves for future observations and estimate yields ahead of time. This could provide a way of determining the value of future *TESS* extended missions before they are approved. It also allows for the planning of follow-up observations such as the *NGTS* monotransit program [Gill et al., 2020] and spectroscopic monitoring campaigns aimed at confirming longer period transiting exoplanets [e.g. *HARPS* programs including; Ulmer-Moll et al., 2023].

3.2.5 Occurrence rates

It is also possible to work backwards and use **TIaRA** produced sensitivity maps to compare to *TESS* or other transit survey discoveries to estimate the underlying occurrence rate of planets. However this would not be without its caveats. *TESS* is ongoing and discoveries are still in progress, hence assessing the completeness of the sample of discoveries for calculating occurrence rates is difficult. Additionally, the sensitivity maps presented in Section 2.7.1 are derived from the SPOC FFI sample and so are biased by the SPOC selection criteria for stars more likely to host detectable planets [Caldwell et al., 2020].

3.3 Applications to other Transit Surveys

The **TIaRA** pipeline is applicable to any transit survey so long as the lightcurve timestamps and noise characteristics are available to be processed. Minor modification will be required to change the functions to accept the new format instead of *TESS* lightcurves. If a noise metric (e.g. the *TESS* CDPP) is not available for the lightcurve it will have to be computed from the flux values. Additionally, the pipeline will need

stellar parameters for the survey targets from a catalogue or similar database.

TIaRA can be applied to previous surveys such as *WASP* [Pollacco et al., 2006], *KELT* [Pepper et al., 2007], *Kepler* [Borucki et al., 2010] and *K2* [Howell et al., 2014] (see Section 1.5), as well as current surveys such as *NGTS* [Wheatley et al., 2018], *ASTEP* [Crouzet et al., 2010], or *SPECULOOS* [Sebastian et al., 2021]. This would allow an assessment of the completeness of these survey as well as an understanding of their biases and the populations of detectable planets.

Future transit surveys could also be assessed using **TIaRA** either waiting until launch to use real data or by simulating lightcurves. This could be performed to predict transit yields from observations made by the Nancy Grace Roman Space Telescope, [previously WIFIRST; Akeson et al., 2019] similar to the estimates produced by Wilson et al. [2023].

With major modifications to the architecture of the pipeline, **TIaRA** could be applied to programs aimed at photometrically following up *TESS* long period transiting planets, such as *NGTS* [Wheatley et al., 2018], *ASTEP* [Crouzet et al., 2010] or *CHEOPS* [Benz et al., 2021]. We could produce sensitivity maps of these follow-up efforts and test different follow-up strategies to determine which is most efficient.

3.3.1 *PLATO*

In December 2026 the European space agency (ESA) is scheduled to launch the PLANetary Transits and Oscillations of Stars [*PLATO*; Rauer et al., 2014] mission with the primary goal of searching for transits of Earth-sized exoplanets around solar-like F, G and K type stars. *PLATO* is expected to have precision approaching that of *Kepler* but with a significantly wider field of view and targeting much brighter stars.

Yield estimates have already been produced for *PLATO* [e.g; Heller et al., 2022; Matuszewski et al., 2023], but use of the **TIaRA** pipeline may provide a useful alternate prediction to these studies. **TIaRA** could be used with simulated lightcurves pre-launch and/or on the real lightcurves post launch. The high cadence of *PLATO* and the duration of monitoring will increase the file size of lightcurve data significantly compared to the *TESS* data. Upgrades to the speed of **TIaRA** (see Section 3.4) or additional computational resources would mitigate these issues. It would also be possible to bin high cadence timestamps with little effect on the yield predictions. However, *PLATO* will monitor significantly fewer stars than the *TESS* SPOC FFI dataset, so these measures may not be critical.

3.4 TIaRA Upgrades

The TIaRA pipeline has proven fast and effective. Upgrades to its speed and efficiency will ease the ability for TIaRA to be ported to other datasets in the future. Optimisation of the pipeline can be achieved through several methods. Many of the functions which currently use ordinary `Python` loops could be vectorised into faster array operations using the `numpy` package [Harris et al., 2020]. Additionally the `numba` package [Lam et al., 2015] could be implemented to speed up compatible functions. Rewriting some functions in a faster programming language than `Python` (e.g. `C`) can also improve the speed of the pipeline.

Another potential change is to the method for inputting planetary radii and periods. While currently we used a binned grid to inject proportionally to occurrence rates, using a uniform distribution would simplify binning the results to different grids (especially if the radius cutoff was also removed). This would also allow us to more easily compare the differences in yield predictions from different occurrence rates as in Matuszewski et al. [2023]. However, we would lose the ability to prioritise ranges of periods and radii for which we desire more robust statistics.

TIaRA could also be upgraded with additional functionality to obtain additional information on the datasets it processes. By generating masses for our injected planets from reasonable mass-radius distributions we could estimate the RV semi-amplitude (see Section 1.2.4) of planets injected into the simulation. This would allow us to estimate yields of planets from *TESS* and other surveys which are amenable to RV followup and mass measurement, which is useful for designing spectroscopic followup programs. Similarly, we could calculate the Transmission Spectroscopy or Emission Spectroscopy metrics [TSM and ESM respectively; Kempton et al., 2018] and estimate the size of exoplanet yields which are amenable to atmospheric characterisation. By tagging individual planets in the simulation as having their periods solved or unsolved by *TESS*, we could estimate the proportion of *TESS* detections that will require follow-up observations to confirm their periods. However, the uncertainties in these predictions would be large in areas of parameter space with few detections expected. To do this we would have to identify signals with no significant gaps in phase between observed transits and tag them as solved in the simulation.

Additionally we could calculate the insolation flux and/or equilibrium temperature of injected planets and present yields in terms of these values as well as period and radius as in Dressing & Charbonneau [2013, 2015]. This would be useful for predicting how many targets atmospheric surveys may have at different temperature ranges. We could also use this feature to estimate the yields of planets in the

habitable zone [Kasting et al., 1993; Kopparapu et al., 2013, 2014] which *TESS* will become more sensitive to as further extended missions find more long-period planets. Although, most of these will be giant planets and therefore not habitable unless they possess rocky moons [Kaltenegger, 2010; Heller, 2012; Heller & Barnes, 2013; Hinkel & Kane, 2013].

3.5 Conclusions

Overall the **TIaRA** pipeline has proved a valuable tool in assessing the *TESS* Year 1 and Year 3 data, and provides interesting insights into the ability of *TESS* to detect long-period and other types of exoplanets. We have found that more long-period transiting exoplanets remain to be found in *TESS* data and this result will prove useful in motivating and planning follow-up programs of long-period *TESS* exoplanets.

Now initial development of **TIaRA** is complete, it will be able to be easily applied to other *TESS* data sets and other transit surveys including *PLATO*. The methods we have developed for this thesis may become a standard way of assessing the completeness and biases of future transit surveys for years to come.

Bibliography

- ALMA Partnership et al., 2015, *ApJ*, 808, L3
- Abe F., et al., 1997, in Ferlet R., Maillard J.-P., Raban B., eds, *Variables Stars and the Astrophysical Returns of the Microlensing Surveys*. p. 75
- Aerts C., 2021, *Reviews of Modern Physics*, 93, 015001
- Aerts C., et al., 2019, *A&A*, 624, A75
- Aizawa M., Uehara S., Masuda K., Kawahara H., Suto Y., 2017, *AJ*, 153, 193
- Akeson R. L., et al., 2013, *PASP*, 125, 989
- Akeson R., et al., 2019, arXiv e-prints, p. arXiv:1902.05569
- Albrecht S., et al., 2012, *ApJ*, 757, 18
- Anglada-Escudé G., et al., 2016, *Nature*, 536, 437
- Armeni A., et al., 2023, arXiv e-prints, p. arXiv:2309.10591
- Bachelet E., Penny M., 2019, *ApJ*, 880, L32
- Bakos G., Noyes R. W., Kovács G., Stanek K. Z., Sasselov D. D., Domsa I., 2004, *PASP*, 116, 266
- Ballard S., 2019, *AJ*, 157, 113
- Baranne A., et al., 1996, *A&AS*, 119, 373
- Barclay T., Quintana E. V., Raymond S. N., Penny M. T., 2017, *ApJ*, 841, 86
- Barclay T., Pepper J., Quintana E. V., 2018, *ApJS*, 239, 2
- Barnes J. W., Fortney J. J., 2004, *ApJ*, 616, 1193
- Barnes J. W., O'Brien D. P., 2002, *ApJ*, 575, 1087

Barros S. C. C., et al., 2023, *A&A*, 673, A4

Batygin K., Stevenson D. J., 2010, *ApJ*, 714, L238

Bayliss D., et al., 2018, *MNRAS*, 475, 4467

Bayliss D., et al., 2020, *The Messenger*, 181, 28

Bean J. L., McArthur B. E., Benedict G. F., Harrison T. E., Bizyaev D., Nelan E., Smith V. V., 2007, *AJ*, 134, 749

Bedell M., et al., 2015, *A&A*, 581, A34

Benedict G. F., et al., 2002, *ApJ*, 581, L115

Benedict G. F., et al., 2006, *AJ*, 132, 2206

Benedict G. F., McArthur B. E., Nelan E. P., Harrison T. E., 2017, *PASP*, 129, 012001

Benedict G. F., McArthur B. E., Nelan E. P., Bean J. L., 2023, *AJ*, 166, 27

Benz W., et al., 2021, *Experimental Astronomy*, 51, 109

Bessel F. W., 1844, *MNRAS*, 6, 136

Beuzit J. L., et al., 2019, *A&A*, 631, A155

Bitsch B., Crida A., Libert A. S., Lega E., 2013, *A&A*, 555, A124

Black D. C., Suffolk G. C. J., 1973, *Icarus*, 19, 353

Bond I. A., 2012, *New A Rev.*, 56, 25

Bond I. A., et al., 2004, *ApJ*, 606, L155

Borucki W. J., et al., 2010, *Science*, 327, 977

Bouma L. G., Winn J. N., Kosiarek J., McCullough P. R., 2017, arXiv e-prints, p. arXiv:1705.08891

Bouma L. G., Jayaraman R., Rappaport S., Rebull L. M., Hillenbrand L. A., Winn J. N., David-Uraz A., Bakos G. Á., 2023, arXiv e-prints, p. arXiv:2309.06471

Bowler B. P., 2016, *PASP*, 128, 102001

Bowman D. M., 2020, *Frontiers in Astronomy and Space Sciences*, 7, 70

- Bowman D. M., et al., 2019, *Nature Astronomy*, 3, 760
- Brahm R., et al., 2023, *AJ*, 165, 227
- Brandt T. D., 2021, *ApJS*, 254, 42
- Brandt G. M., Brandt T. D., Dupuy T. J., Michalik D., Marleau G.-D., 2021, *ApJ*, 915, L16
- Bruno G., 1584b, *De l’infinito universo et mundi*
- Bruno G., 1584a, *La Cena de le Ceneri*
- Bryant E. M., Bayliss D., Van Eylen V., 2023, *MNRAS*, 521, 3663
- Buchhave L. A., et al., 2010, *ApJ*, 720, 1118
- Bursens S., et al., 2020, *A&A*, 639, A81
- Caldwell D. A., et al., 2020, *Research Notes of the American Astronomical Society*, 4, 201
- Campbell B., Walker G. A. H., Yang S., 1988, *ApJ*, 331, 902
- Carter A. L., et al., 2023, *ApJ*, 951, L20
- Cassan A., et al., 2012, *Nature*, 481, 167
- Cassidy T. A., Mendez R., Arras P., Johnson R. E., Skrutskie M. F., 2009, *ApJ*, 704, 1341
- Charbonneau D., Brown T. M., Latham D. W., Mayor M., 2000, *ApJ*, 529, L45
- Charbonneau D., Brown T. M., Noyes R. W., Gilliland R. L., 2002, *ApJ*, 568, 377
- Chauvin G., Lagrange A. M., Dumas C., Zuckerman B., Mouillet D., Song I., Beuzit J. L., Lowrance P., 2004, *A&A*, 425, L29
- Chen J., Kipping D., 2017, *ApJ*, 834, 17
- Choi J., McCarthy C., Marcy G. W., Howard A. W., Fischer D. A., Johnson J. A., Isaacson H., Wright J. T., 2013, *ApJ*, 764, 131
- Christiansen J. L., 2017, *Planet Detection Metrics: Pixel-Level Transit Injection Tests of Pipeline Detection Efficiency for Data Release 25*, Kepler Science Document KSCI-19110-001, id. 18. Edited by Michael R. Haas and Natalie M. Batalha

- Christiansen J. L., et al., 2012, *PASP*, 124, 1279
- Cloutier R., et al., 2017, *A&A*, 608, A35
- Collier Cameron A., et al., 2006, *MNRAS*, 373, 799
- Collier Cameron A., et al., 2007, *MNRAS*, 375, 951
- Cooke B. F., Pollacco D., West R., McCormac J., Wheatley P. J., 2018, *A&A*, 619, A175
- Cooke B. F., Pollacco D., Bayliss D., 2019, *A&A*, 631, A83
- Copernicus N., 1543, *De revolutionibus orbium coelestium*
- Crouzet N., et al., 2010, *A&A*, 511, A36
- Currie T., et al., 2023a, *Science*, 380, 198
- Currie T., Biller B., Lagrange A., Marois C., Guyon O., Nielsen E. L., Bonnefoy M., De Rosa R. J., 2023b, in Inutsuka S., Aikawa Y., Muto T., Tomida K., Tamura M., eds, *Astronomical Society of the Pacific Conference Series Vol. 534, Protostars and Planets VII*. p. 799 ([arXiv:2205.05696](https://arxiv.org/abs/2205.05696)), doi:10.48550/arXiv.2205.05696
- Daszyńska-Daszkiewicz J., Walczak P., Szewczuk W., Niewiadomski W., 2023, *MNRAS*,
- Dawson R. I., Johnson J. A., 2018, *ARA&A*, 56, 175
- Demory B.-O., Seager S., 2011, *ApJS*, 197, 12
- Dobos V., Charnoz S., Pál A., Roque-Bernard A., Szabó G. M., 2021, *PASP*, 133, 094401
- Dong J., et al., 2021, *ApJS*, 255, 6
- Dong J., et al., 2023, *ApJ*, 951, L29
- Doppler C., Studnica F. J., 1842, *Ueber das farbige licht der doppelsterne und einiger anderer gestirne des himmels*.
- Dragomir D., Huang C. X., Kane S., Dalba P. A., Günther M. N., 2019, in *AAS/Division for Extreme Solar Systems Abstracts*. p. 103.04
- Dragomir D., et al., 2023, in *American Astronomical Society Meeting Abstracts*. p. 318.03

Dressing C. D., Charbonneau D., 2013, *ApJ*, 767, 95

Dressing C. D., Charbonneau D., 2015, *ApJ*, 807, 45

Duffell P. C., Haiman Z., MacFadyen A. I., D’Orazio D. J., Farris B. D., 2014, *ApJ*, 792, L10

Dürmann C., Kley W., 2015, *A&A*, 574, A52

Eberhardt J., et al., 2022, in *Bulletin of the American Astronomical Society*. p. 102.385

Einstein A., 1936, *Science*, 84, 506

Espinoza-Retamal J. I., Zhu W., Petrovich C., 2023, *arXiv e-prints*, p. arXiv:2309.08665

Essack Z., et al., 2023, *AJ*, 165, 47

Fabrycky D., Tremaine S., 2007, *ApJ*, 669, 1298

Faedi F., et al., 2011, *A&A*, 531, A40

Fausnaugh M. M., et al., 2021, *ApJ*, 908, 51

Feng F., Butler R. P., Vogt S. S., Holden B., Rui Y., 2023, *MNRAS*, 525, 607

Fischer D. A., et al., 2008, *ApJ*, 675, 790

Fontenelle B. L. B., 1686, *Entretiens sur la pluralite des mondes*.

Ford E. B., Rasio F. A., 2006, *ApJ*, 638, L45

Foreman-Mackey D., Montet B. T., Hogg D. W., Morton T. D., Wang D., Schölkopf B., 2015, *ApJ*, 806, 215

Fortney J. J., Visscher C., Marley M. S., Hood C. E., Line M. R., Thorngren D. P., Freedman R. S., Lupu R., 2020, *AJ*, 160, 288

Frame G., et al., 2023, *MNRAS*, 523, 1163

Fressin F., et al., 2013, *ApJ*, 766, 81

Gaia Collaboration et al., 2016, *A&A*, 595, A1

Gaia Collaboration et al., 2018, *A&A*, 616, A1

Gaia Collaboration et al., 2023, A&A, 674, A1

Gandolfi D., et al., 2018, A&A, 619, L10

Gao P., Marley M. S., Zahnle K., Robinson T. D., Lewis N. K., 2017, AJ, 153, 139

Gardner J. P., et al., 2006, Space Sci. Rev., 123, 485

Gatewood G. D., 1995, Ap&SS, 223, 91

Gaudi B. S., et al., 2017, Nature, 546, 514

Gaudi B. S., et al., 2020, arXiv e-prints, p. arXiv:2001.06683

Giacalone S., et al., 2022, AJ, 163, 99

Giles H. A. C., et al., 2018, A&A, 615, L13

Gill S., et al., 2020, ApJ, 898, L11

Gillon M., et al., 2017, Nature, 542, 456

Goffo E., et al., 2023, ApJ, 955, L3

Gould A., 2000, ApJ, 542, 785

Gould A., Loeb A., 1992, ApJ, 396, 104

Grieves N., et al., 2022, A&A, 668, A29

Guerrero N. M., et al., 2021, ApJS, 254, 39

Günther M. N., et al., 2018, MNRAS, 478, 4720

Gupta A. F., et al., 2023, AJ, 165, 234

Handler G., et al., 2019, ApJ, 873, L4

Harris C. R., et al., 2020, Nature, 585, 357

Hatzes A. P., Cochran W. D., Endl M., McArthur B., Paulson D. B., Walker G. A. H., Campbell B., Yang S., 2003, ApJ, 599, 1383

Hawthorn F., et al., 2023a, TESS Duotransit Candidates from the Southern Ecliptic Hemisphere (arXiv:2310.17268)

Hawthorn F., et al., 2023b, MNRAS, 520, 3649

Hawthorn F., et al., 2023c, MNRAS, 524, 3877

Hebb L., et al., 2009, ApJ, 693, 1920

Hebb L., et al., 2010, ApJ, 708, 224

Heintz W. D., 1988, JRASC, 82, 140

Heller R., 2012, A&A, 545, L8

Heller R., Barnes R., 2013, Astrobiology, 13, 18

Heller R., Harre J.-V., Samadi R., 2022, A&A, 665, A11

Hellier C., et al., 2009, Nature, 460, 1098

Hellier C., et al., 2011, A&A, 535, L7

Hellier C., et al., 2014, MNRAS, 440, 1982

Hilditch R. W., 2001, An Introduction to Close Binary Stars. Cambridge University Press, doi:10.1017/CBO9781139163576

Hinkel N. R., Kane S. R., 2013, ApJ, 774, 27

Hipke M., Heller R., 2019, A&A, 623, A39

Holl B., et al., 2023, A&A, 674, A10

Holoien T. W. S., et al., 2019, ApJ, 883, 111

Howell S. B., et al., 2014, PASP, 126, 398

Hsu D. C., Ford E. B., Ragozzine D., Ashby K., 2019, AJ, 158, 109

Hu R., 2021, ApJ, 921, 27

Huang C., Wu Y., Triaud A. H. M. J., 2016, ApJ, 825, 98

Huang C. X., et al., 2018a, arXiv e-prints, p. arXiv:1807.11129

Huang C. X., et al., 2018b, ApJ, 868, L39

Huang C. X., et al., 2020, Research Notes of the American Astronomical Society, 4, 204

Huygens C., 1698, The celestial worlds discover'd:

- Itoh Y., et al., 2005, ApJ, 620, 984
- JWST Transiting Exoplanet Community Early Release Science Team et al., 2023, Nature, 614, 649
- Jacob W. S., 1855, MNRAS, 15, 228
- Jehin E., et al., 2011, The Messenger, 145, 2
- Jenkins J. M., et al., 2016, in Chiozzi G., Guzman J. C., eds, Society of Photo-Optical Instrumentation Engineers (SPIE) Conference Series Vol. 9913, Software and Cyberinfrastructure for Astronomy IV. p. 99133E, doi:10.1117/12.2233418
- Johnson M., 2023, in American Astronomical Society Meeting Abstracts. p. 401.02
- Johnson J. A., Aller K. M., Howard A. W., Crepp J. R., 2010, PASP, 122, 905
- Johnson S. A., Penny M., Gaudi B. S., Kerins E., Rattenbury N. J., Robin A. C., Calchi Novati S., Henderson C. B., 2020, AJ, 160, 123
- Jones H. R. A., Paul Butler R., Tinney C. G., Marcy G. W., Penny A. J., McCarthy C., Carter B. D., Pourbaix D., 2002, MNRAS, 333, 871
- Kalas P., Liu M. C., Matthews B. C., 2004, Science, 303, 1990
- Kaltenegger L., 2010, ApJ, 712, L125
- Kasting J. F., Whitmire D. P., Reynolds R. T., 1993, Icarus, 101, 108
- Kaufer A., Stahl O., Tubbesing S., Nørregaard P., Avila G., Francois P., Pasquini L., Pizzella A., 1999, The Messenger, 95, 8
- Kempton E. M. R., et al., 2018, PASP, 130, 114401
- Kepler J., 1609, Astronomia nova ..., seu physica coelestis, tradita commentariis de motibus stellae martis, doi:10.3931/e-rara-558
- Keppler M., et al., 2019, A&A, 625, A118
- Kiefer F., Hébrard G., Lecavelier des Etangs A., Martioli E., Dalal S., Vidal-Madjar A., 2021, A&A, 645, A7
- Kim S.-L., et al., 2016, Journal of Korean Astronomical Society, 49, 37
- Kipping D. M., 2013, MNRAS, 434, L51

- Kipping D. M., Fossey S. J., Campanella G., 2009, MNRAS, 400, 398
- Kiss C., Farkas-Takács A., Szakáts R., Müller T., Pál A., 2021, in European Planetary Science Congress. pp EPSC2021–123, doi:10.5194/epsc2021-123
- Konacki M., Torres G., Jha S., Sasselov D. D., 2003, Nature, 421, 507
- Konopacky Q. M., Barman T. S., Macintosh B. A., Marois C., 2013, Science, 339, 1398
- Kopparapu R. K., et al., 2013, ApJ, 765, 131
- Kopparapu R. K., Ramirez R. M., SchottelKotte J., Kasting J. F., Domagal-Goldman S., Eymet V., 2014, ApJ, 787, L29
- Kovács G., Zucker S., Mazeh T., 2002, A&A, 391, 369
- Kreidberg L., 2015, PASP, 127, 1161
- Kreidberg L., 2018, in Deeg H. J., Belmonte J. A., eds, , Handbook of Exoplanets. Springer International Publishing, Cham, pp 2083–2105, doi:10.1007/978-3-319-55333-7_100, https://doi.org/10.1007/978-3-319-55333-7_100
- Kunimoto M., Matthews J. M., 2020, AJ, 159, 248
- Kunimoto M., Winn J., Ricker G. R., Vanderspek R. K., 2022, AJ, 163, 290
- Lagrange A. M., et al., 2010, Science, 329, 57
- Lam S. K., Pitrou A., Seibert S., 2015, in Proceedings of the Second Workshop on the LLVM Compiler Infrastructure in HPC. pp 1–6
- Laureijs R., et al., 2011, arXiv e-prints, p. arXiv:1110.3193
- Lendl M., et al., 2020, MNRAS, 492, 1761
- Lopez E. D., Fortney J. J., 2014, ApJ, 792, 1
- Lovis C., Fischer D., 2010, in Seager S., ed., , Exoplanets. University of Arizona Press, pp 27–53
- Lubin J., et al., 2021, AJ, 162, 61
- Luque R., Pallé E., 2022, Science, 377, 1211
- Maciejewski G., Golonka J., Łoboda W., Ohlert J., Fernández M., Aceituno F., 2023, MNRAS, 525, L43

- Macintosh B., et al., 2014, *Proceedings of the National Academy of Science*, 111, 12661
- Madhusudhan N., 2019, *ARA&A*, 57, 617
- Madhusudhan N., Knutson H., Fortney J. J., Barman T., 2014a, in Beuther H., Klessen R. S., Dullemond C. P., Henning T., eds, *Protostars and Planets VI*. pp 739–762 ([arXiv:1402.1169](#)), doi:10.2458/azu_uapress_9780816531240-ch032
- Madhusudhan N., Amin M. A., Kennedy G. M., 2014b, *ApJ*, 794, L12
- Makarov V. V., Efroimsky M., 2023, *A&A*, 672, A78
- Mann C., et al., 2023, *AJ*, 165, 217
- Mardling R. A., 2007, *MNRAS*, 382, 1768
- Marois C., Macintosh B., Barman T., Zuckerman B., Song I., Patience J., Lafrenière D., Doyon R., 2008, *Science*, 322, 1348
- Matuszewski F., Nettelmann N., Cabrera J., Börner A., Rauer H., 2023, *arXiv e-prints*, p. [arXiv:2307.12163](#)
- Maxted P. F. L., 2016, *A&A*, 591, A111
- Maxted P. F. L., et al., 2011, *PASP*, 123, 547
- Mayor M., Queloz D., 1995, *Nature*, 378, 355
- Mayor M., et al., 2003, *The Messenger*, 114, 20
- Mazeh T., Holczer T., Faigler S., 2016, *A&A*, 589, A75
- McArthur B. E., et al., 2004, *ApJ*, 614, L81
- McArthur B. E., Benedict G. F., Barnes R., Martioli E., Korzennik S., Nelan E., Butler R. P., 2010, *ApJ*, 715, 1203
- McArthur B. E., Benedict G. F., Henry G. W., Hatzes A., Cochran W. D., Harrison T. E., Johns-Krull C., Nelan E., 2014, *ApJ*, 795, 41
- McLaughlin D., 1924, *ApJ*, 60
- Mikal-Evans T., et al., 2023, *AJ*, 165, 84
- Mróz P., et al., 2017, *Nature*, 548, 183

- Muirhead P. S., Dressing C. D., Mann A. W., Rojas-Ayala B., Lépine S., Paegert M., De Lee N., Oelkers R., 2018, *AJ*, 155, 180
- Mustill A. J., Davies M. B., Johansen A., 2017a, *MNRAS*, 468, 3000
- Mustill A. J., Davies M. B., Johansen A., 2017b, *MNRAS*, 468, 3000
- Naef D., et al., 2001, *A&A*, 375, L27
- Nielsen E. L., et al., 2019, *AJ*, 158, 13
- O’Brien S. M., et al., 2022, *MNRAS*, 509, 6111
- Öberg K. I., Murray-Clay R., Bergin E. A., 2011, *ApJ*, 743, L16
- Oberg K. I., Fayolle E., Linnartz H., van Dishoeck E., Fillion J., Bertin M., 2013, in *American Astronomical Society Meeting Abstracts*. p. 202.02
- Öberg K. I., Facchini S., Anderson D. E., 2023, *ARA&A*, 61, 287
- Ohno K., Fortney J. J., 2023, *ApJ*, 946, 18
- Osborn H., 2017, PhD thesis, University of Warwick, UK
- Osborn A., et al., 2023a, *MNRAS*,
- Osborn H. P., et al., 2023b, *MNRAS*, 523, 3069
- Owen J. E., Wu Y., 2017, *ApJ*, 847, 29
- Paczynski B., 1986, *ApJ*, 304, 1
- Pecaut M. J., Mamajek E. E., 2013, *ApJS*, 208, 9
- Pepe F. A., et al., 2010, in McLean I. S., Ramsay S. K., Takami H., eds, *Society of Photo-Optical Instrumentation Engineers (SPIE) Conference Series Vol. 7735, Ground-based and Airborne Instrumentation for Astronomy III*. p. 77350F, doi:10.1117/12.857122
- Pepper J., et al., 2007, *PASP*, 119, 923
- Perna R., Heng K., Pont F., 2012, *ApJ*, 751, 59
- Perryman M., Hartman J., Bakos G. Á., Lindegren L., 2014, *ApJ*, 797, 14
- Petrovich C., 2014, in *AAS/Division for Planetary Sciences Meeting Abstracts #46*. p. 301.03

- Petrovich C., 2015, *ApJ*, 805, 75
- Plavchan P., et al., 2020, *Nature*, 582, 497
- Pollacco D. L., et al., 2006, *PASP*, 118, 1407
- Pollacco D., et al., 2008, *MNRAS*, 385, 1576
- Rauer H., et al., 2014, *Experimental Astronomy*, 38, 249
- Raynard L., et al., 2018, *MNRAS*, 481, 4960
- Rice M., Laughlin G., 2020, in *European Planetary Science Congress*. pp EPSC2020–420, doi:10.5194/epsc2020-420
- Rice M., et al., 2022, *AJ*, 164, 104
- Ricker G. R., et al., 2015, *Journal of Astronomical Telescopes, Instruments, and Systems*, 1, 014003
- Rogers L. A., 2015, *ApJ*, 801, 41
- Rossiter R., 1924, *ApJ*, 60
- Sabotta S., et al., 2021, *A&A*, 653, A114
- Sebastian D., et al., 2021, *A&A*, 645, A100
- Shporer A., et al., 2019, *AJ*, 157, 178
- Simon A. E., Szabó G. M., Kiss L. L., Szatmáry K., 2012, *MNRAS*, 419, 164
- Southworth J., Bowman D. M., Tkachenko A., Pavlovski K., 2020, *MNRAS*, 497, L19
- Stassun K. G., et al., 2019, *AJ*, 158, 138
- Sullivan P. W., et al., 2015, *ApJ*, 809, 77
- Szakáts R., et al., 2023, *A&A*, 669, L3
- Tan X., Showman A. P., 2021, *MNRAS*, 502, 678
- Triaud A. H. M. J., 2018, in Deeg H. J., Belmonte J. A., eds, , *Handbook of Exoplanets*. Springer International Publishing, Cham, pp 1375–1401, doi:10.1007/978-3-319-55333-7_2, https://doi.org/10.1007/978-3-319-55333-7_2

Tuson A., et al., 2023, MNRAS, 523, 3090

Udalski A., Szymański M. K., Szymański G., 2015, Acta Astron., 65, 1

Ulmer-Moll S., et al., 2022, A&A, 666, A46

Ulmer-Moll S., et al., 2023, A&A, 674, A43

Vallely P. J., et al., 2019, MNRAS, 487, 2372

Valsecchi F., Rappaport S., Rasio F. A., Marchant P., Rogers L. A., 2015, ApJ, 813, 101

Van Eylen V., Albrecht S., 2015, ApJ, 808, 126

Vanderburg A., et al., 2015, ApJ, 800, 59

Vanderspek R., et al., 2019, ApJ, 871, L24

Venner A., Vanderburg A., Pearce L. A., 2021, AJ, 162, 12

Vigan A., et al., 2021, A&A, 651, A72

Villanueva Steven J., Dragomir D., Gaudi B. S., 2019, AJ, 157, 84

Vines J. I., et al., 2019, MNRAS, 489, 4125

Virtanen P., et al., 2020, Nature Methods, 17, 261

Vogt S. S., et al., 1994, in Crawford D. L., Craine E. R., eds, Society of Photo-Optical Instrumentation Engineers (SPIE) Conference Series Vol. 2198, Instrumentation in Astronomy VIII. p. 362, doi:10.1117/12.176725

Walker G. A. H., Bohlender D. A., Walker A. R., Irwin A. W., Yang S. L. S., Larson A., 1992, ApJ, 396, L91

West R. G., et al., 2019, MNRAS, 486, 5094

Wheatley P. J., et al., 2018, MNRAS, 475, 4476

Wilson R. F., et al., 2023, arXiv e-prints, p. arXiv:2305.16204

Winn J. N., 2014, arXiv e-prints, p. arXiv:1001.2010v5

Winn J. N., Fabrycky D. C., 2015, ARA&A, 53, 409

Wolszczan A., Frail D. A., 1992, Nature, 355, 145

- Wright J. T., Gaudi B. S., 2013, in Oswalt T. D., French L. M., Kalas P., eds, , Planets, Stars and Stellar Systems: Volume 3: Solar and Stellar Planetary Systems. Springer Netherlands, Dordrecht, pp 489–540, doi:10.1007/978-94-007-5606-9_10, https://doi.org/10.1007/978-94-007-5606-9_10
- Wu Y., Lithwick Y., 2011, ApJ, 735, 109
- Xiang-Gruess M., 2016, MNRAS, 455, 3086
- Yao X., et al., 2019, AJ, 157, 37
- Yee S. W., et al., 2023, VizieR Online Data Catalog, p. J/ApJS/265/1
- Zhou Y., Herczeg G. J., Kraus A. L., Metchev S., Cruz K. L., 2014, ApJ, 783, L17
- Zhou G., et al., 2019, AJ, 158, 141
- de Beurs Z. L., de Wit J., Venner A., Berardo D., Bryan J., Winn J. N., Fulton B. J., Howard A. W., 2023, AJ, 166, 136
- van de Kamp P., 1963, AJ, 68, 515
- van de Kamp P., 1969, AJ, 74, 757
- van de Kamp P., 1982, Vistas in Astronomy, 26, 141